COULOMB EXCITATION OF NEUTRON-RICH SULFUR ISOTOPES

By

Brenden Robert Longfellow

A DISSERTATION

Submitted to
Michigan State University
in partial fulfillment of the requirements
for the degree of

Physics — Doctor of Philosophy

2020

ABSTRACT

COULOMB EXCITATION OF NEUTRON-RICH SULFUR ISOTOPES

By

Brenden Robert Longfellow

Understanding how the structure of nuclei is modified far from stability has become one of the major goals in nuclear science. While the nuclear shell model was successful in explaining the magic numbers observed for the stable and near-stable nuclei available for study at the time, subsequent research on nuclei with extreme proton-to-neutron ratios has revealed surprising changes in nuclear structure. For example, the conventional magic number of neutrons $N = 28$ has been shown to break down in the region of neutron-rich nuclei centered around ^{42}Si and ^{44}S known as the $N = 28$ island of inversion. In this work, predictions made by the shell-model effective interaction SDPF-MU, which has been successful in describing the evolution of collectivity for nuclei in this region, were put to the test using the selectivity of intermediate-energy Coulomb excitation in an experiment utilizing the scintillator array CAESAR and the S800 magnetic spectrograph at the National Superconducting Cyclotron Laboratory at Michigan State University. In the even-even neutron-rich sulfur isotopes ^{38,40,42,44}S, $B(E2)$ strengths from the ground states to multiple 2^+ states were measured allowing a detailed comparison to theoretical predictions by the SDPF-MU Hamiltonian. For ^{43}S, excited states built on top of both the ground state and the isomeric state at 320 keV were excited, allowing the collective nature of these shape-coexisting structures to be characterized.

ACKNOWLEDGMENTS

I am deeply grateful for the support I have received over the course of my graduate career from friends, colleagues, and mentors. The following list of acknowledgments is certainly not exhaustive. First and foremost, I would like to thank my advisor, Alexandra Gade, for her tireless guidance and enthusiasm. Thank you for everything you have taught me about physics and for encouraging me to pursue opportunities ranging from travel to collaborate on measurements in Japan to writing proposals for experiments. Your mentorship and advice have helped me grow tremendously as a scientist. I would also like to thank Dirk Weisshaar for sharing his knowledge of γ-ray detectors, electronics, and the liquid nitrogen fill system, answering questions about data analysis, and helping me develop as an experimentalist.

Next, I would like to thank the members of my guidance committee for their support and encouragement. Thank you to Daniel Bazin for tuning the S800 spectrograph during the sulfur Coulomb excitation experiment that this dissertation results from and for providing expertise during gamma group meetings. Thank you to Alex Brown, who I was lucky to be able to work with on a project exploring Thomas-Ehrman shifts in *sd*-shell nuclei. Thank you to Wade Fisher for providing the outside perspective of a high-energy experimentalist to my committee. Finally, I thank Sean Liddick for his work with the Nuclear Science and Security Consortium (NSSC), which I am grateful to for funding, and for giving me the opportunity to expand my knowledge by collaborating on a few β-decay experiments. I would also like to thank the NSSC giving me the chance to work with Aaron Gallant and Nick Scielzo at Lawrence Livermore National Laboratory on a summer project.

During my time as a graduate student, I was lucky to have the chance to learn from postdoctoral researchers including Peter Bender, Joe Belarge, Mark Spieker, Jing Li, and

Sayani Biswas. You have had an indelible impact on my scientific career. I would also like to thank the graduate students in the gamma group who I had the privilege to work alongside: Eric Lunderberg, (upstairs) Brandon Elman, Daniel Rhodes, Matt Hill, and Peter Farris. These graduate students and the graduate students in the lifetime group have my appreciation for sharing the burden of the filling system pager.

I would also like to thank the staff at the National Superconducting Cyclotron Laboratory (NSCL). Without them it would not have been possible to run the sulfur Coulomb excitation experiment. I have enjoyed my time at the NSCL and am looking forward to the science results that will come from the Facility for Rare Isotope Beams. I am thankful for the friendships I have made at Michigan State University and for the friendship of Jason Surbrook, who followed me to the NSCL from the University of North Carolina at Chapel Hill. I was glad to be able to play soccer with the foot-pounds, go to trivia nights, and attend MSU sporting events. Finally, I would like to thank my parents, Russell and Cathie, and my brothers, Jerrod, Darec, and Rion, for their unwavering support.

TABLE OF CONTENTS

LIST OF TABLES . . . . . **vii**

LIST OF FIGURES . . . . . **viii**

Chapter 1 Introduction **1**
1.1 Atomic Nuclei 1
1.2 Nuclear Shell Model 6
1.3 Collective Models 10
1.4 Electromagnetic Transitions 12
1.5 Configuration Interaction Method 16
1.6 Breakdown of the N=28 Magic Number 17
1.7 Motivation for Studying the Neutron-Rich Sulfur Isotopes 22

Chapter 2 Intermediate-Energy Coulomb Excitation **28**
2.1 Alder-Winther Formalism 30
2.2 Experimental Considerations 36
2.3 Reduced Transition Probabilities and Lifetimes 38

Chapter 3 Experimental Method **39**
3.1 Beam Production and Purification 39
3.2 S800 Magnetic Spectrograph 43
3.2.1 Particle Identification and Trajectory Reconstruction 45
3.2.2 Isomer Tagging 49
3.3 In-Beam γ-Ray Spectroscopy with CAESAR 51
3.3.1 Interaction of γ Rays with Matter 51
3.3.2 Doppler Reconstruction 56
3.3.3 Nearest-Neighbor Addback 57
3.3.4 CAESAR Calibrations 58

Chapter 4 Data Analysis and Results **64**
4.1 General Method 64
4.2 Results for Even-Even Neutron-Rich Sulfur Isotopes 69
4.2.1 Intermediate-Energy Coulomb Excitation of ^{38}S 69
4.2.2 Intermediate-Energy Coulomb Excitation of ^{40}S 77
4.2.3 Intermediate-Energy Coulomb Excitation of ^{42}S 82
4.2.4 Intermediate-Energy Coulomb Excitation of ^{44}S 89
4.3 Results for ^{43}S 94
4.3.1 ^{43}S Incoming Beam Isomeric Content 94
4.3.2 Intermediate-Energy Coulomb Excitation of ^{43}S 96

Chapter 5 Discussion **106**

Chapter 6 Summary and Outlook 113

BIBLIOGRAPHY 115

LIST OF TABLES

Table 3.1: Production target, momentum acceptance dp/p, and energy as inferred from the magnetic rigidity setting of the segment of the analysis line just before the 492 mg/cm^2 ^{209}Bi reaction target in front of the S800 spectrograph for each secondary beam setting. 43

Table 3.2: Energy resolution parameters for each of the 10 rings of CAESAR for energies in keV. 63

Table 4.1: Corrected number of sulfur isotopes N_{beam} and average livetimes for particle triggers in the S800 LT_{S800} and S800-CAESAR coincidences LT_{coinc} for each of the settings. 67

Table 5.1: $B(E2)$ strengths for the neutron-rich sulfur isotopes studied in this work compared to the results of previous intermediate-energy Coulomb excitation experiments and theoretical calculations using the SDPF-MU Hamiltonian with effective proton and neutron charges of 1.35 and 0.35, respectively. 108

LIST OF FIGURES

Figure 1.1: Central projection of the nucleon-nucleon interaction. Outside the repulsive core, the potential is attractive with rapidly diminishing strength. Over longer ranges, the central nuclear force can be modeled through exchange of massive particles called mesons. Figure modified from [1]. . . 2

Figure 1.2: The chart of the nuclides with neutron number on the x axis and proton number on the y axis. Terra Incognita refers to the region of the chart with experimentally unobserved nuclei that are predicted to exist. The dotted lines indicate the traditional magic numbers of neutrons and protons discussed in the text. Figure adapted from [2]. 3

Figure 1.3: Differences between experimental binding energies and binding energies calculated using the liquid drop model for nuclei with $Z \geq 8$ as a function of neutron number. The peaks at $N = 28$, 50, 82, and 126 indicate that nuclei have internal structure. Figure taken from [3] with data from [4]. . 5

Figure 1.4: Energies of neutron single-particle orbitals calculated for ^{208}Pb using different mean field potentials: three-dimensional harmonic oscillator, Woods-Saxon, and Woods-Saxon plus spin-orbit. The number in brackets is the maximum number of neutrons allowed in the orbital by the Pauli principle and the number outside the brackets is the sum of total allowed nucleons through this orbital. Orbitals are labeled by their quantum numbers. Figure is adapted from [5]. 9

Figure 1.5: Energies of the first 2^+ excited state and ratios $R_{4/2}$ of energies for the first 2^+ and 4^+ states in even-even nuclei across the chart of nuclides. The neutron and proton magic numbers are denoted by dashed lines. Figure taken from [6]. 12

Figure 1.6: Experimental energies of the first 2^+ states [7] (top) and $B(E2; 0_1^+ \rightarrow 2_1^+)$ strengths [8] (bottom) for Si, S, Ar, and Ca isotopes showing the evolution of collectivity around the conventional neutron magic numbers $N = 20$ and $N = 28$. 19

Figure 1.7: Schematic illustration of the tensor force. The repulsive interaction between the neutron $0f_{7/2}(j_>)$ orbital and proton $0d_{5/2}(j_>)$ and the attractive interaction between the neutron $0f_{7/2}(j_>)$ orbital and proton $0d_{3/2}(j_<)$ orbital reduce the $Z = 14$ sub-shell gap. Figure modified from [9]. 21

Figure 1.8: SDPF-MU neutron $1p_{3/2}$ occupancies for 0^+ (red) and 2^+ states (blue) below 4.5 MeV in ^{38,40,42,44}S. The increase in occupancy for the second 2^+ state in ^{42}S relative to ^{38}S explains the observed change in γ-decay pattern. Figure modified from [10]. 26

Figure 1.9: SDPF-MU predictions for $B(E2; 0_1^+ \rightarrow 2^+)$ strengths in e^2fm^4 for levels in ^{38,40,42,44}S. Arrow widths are proportional to transition strength. 2^+ states above 4 MeV with $B(E2)$ values less than 10 e^2fm^4 are omitted in this figure. Effective proton and neutron charges of 1.35 and 0.35, respectively, were used in the SDPF-MU calculations. 27

Figure 2.1: Schematic of intermediate-energy Coulomb excitation. The projectile (target) nucleus is inelastically excited in the Coulomb field of the target (projectile) nucleus. In analysis, a maximum center-of-mass scattering angle θ (minimum impact parameter b) is considered to ensure no nuclear contribution to the cross section. Figure adapted from [11]. 29

Figure 3.1: Layout of the Coupled Cyclotron Facility at the National Superconducting Cyclotron Laboratory showing the ion sources, K500 and K1200 cyclotrons, and A1900 fragment separator [12]. Figure adapted from [13]. . 40

Figure 3.2: Illustration of the S800 magnetic spectrograph including the analysis line. The target position was surrounded by the CsI(Na) array CAESAR. Figure taken from [11]. 44

Figure 3.3: S800 focal plane diagram showing the cathode readout drift chambers (CRDCs), ionization chamber, and E1 plastic scintillator. Figure modified from [13]. 45

Figure 3.4: Typical calibrated mask run for CRDC1 (upstream) taken from the ^{38}S setting. 48

Figure 3.5: Particle identification plot utilizing energy loss and time of flight for the ^{44}S setting. The energy loss is measured in the S800 ionization chamber and is proportional to Z^2 and the time of flight is measured between the OBJ and E1 plastic scintillators and is proportional to A/Z. 50

Figure 3.6: Illustration of the arrangement of CAESAR into 10 rings of detectors. Left: cross-sectional view of rings F and J perpendicular to the beam axis. Right: the $3 \times 3 \times 3$ inch detectors occupy the two most upstream (A,B) and two most downstream (I,J) rings while the $2 \times 2 \times 4$ inch detectors occupy the six middle rings (C-H). The target position is shown in red. Figure taken from [14]. 52

Figure 3.7: Photograph of the 192 CsI(Na) detectors composing CAESAR in front of the S800 spectrograph. 53

Figure 3.8: Illustration of the response of a γ-ray detector to many monoenergetic γ rays showing characteristic features including the full-energy peak, Compton edge, Compton continuum, and single and double-escape peaks. Figure taken from [11]. 54

Figure 3.9: Energies after calibration for the 192 CAESAR detectors for the ^{88}Y source. The 898-keV and 1836-keV transitions are aligned for all detectors. The 2614-keV transition from room background is also visible. 59

Figure 3.10: Alignment of the corrected CAESAR timings for all 192 detectors after calibration gated on γ-ray energies above 500 keV in the laboratory frame for one of the ^{38}S runs. 60

Figure 3.11: Full-energy peak efficiency of CAESAR as a function of energy as determined from direct measurement of a low-activity ^{207}Bi source and from coincidence measurements with a $LaBr_3$(Ce) detector for ^{60}Co, ^{88}Y, and ^{207}Bi sources compared to predictions from GEANT4 simulations. The efficiency curves here were produced treating the 192 detectors of CAESAR independently (no addback applied). 62

Figure 4.1: Doppler-corrected energy versus corrected CAESAR timing gated on ^{40}S. As seen from the 904-keV peak, the prompt time-energy cut (red) removes random background counts without affecting the prompt γ decays that occur after Coulomb excitation. 68

Figure 4.2: Top: Doppler-corrected energy spectrum for ^{38}S gated on scattering angles smaller than 40 mrad in the laboratory frame. The blue curves are the individual components of the fit function derived from GEANT4 simulations along with a double exponential background. The red curve is the total fit function. Bottom: Low-energy portion of the Doppler-corrected energy spectrum for ^{38}S. The large background at low energies is due to bremsstrahlung and other beam-correlated background. 71

Figure 4.3: Doppler-corrected coincidence matrix for ^{38}S events with exactly two γ rays detected in CAESAR. Both the x and y axes have 16-keV wide bins. The matrix is filled symmetrically. The 1292-keV and 1513-keV transitions are in coincidence and the 1292-keV and 2508-keV transitions are in coincidence. 72

Figure 4.4: Background-subtracted, Doppler-corrected γ-ray spectrum for ^{38}S counts in coincidence with the 1292-keV transition. The 1513-keV and 2508-keV peaks are visible. 73

Figure 4.5: Counts in the 1292-keV peak as a function of scattering angle in the laboratory frame. Using the nominal safe scattering angle of 55 mrad would lead to an underestimation of the angle-integrated cross section. A maximum safe scattering angle of 40 mrad was considered in the analysis. 74

Figure 4.6: Top: feeding-subtracted angle-integrated cross section as a function of choice of scattering angle cut derived from the experimental data for the 2_1^+ state in ^{38}S (black). The red curve is the expected cross section assuming a $B(E2; 0_1^+ \rightarrow 2_1^+)$ strength of 229 e^{2}fm^4. Bottom: $B(E2; 0_1^+ \rightarrow 2_1^+)$ strength calculated using Alder-Winther theory for different choices of maximum scattering angle. 76

Figure 4.7: Doppler-corrected energy spectrum for ^{40}S gated on scattering angles smaller than 40 mrad in the laboratory frame. The blue curves are the individual components of the fit function derived from GEANT4 simulations along with a double exponential background. The red curve is the total fit function. 78

Figure 4.8: Doppler-corrected coincidence matrix for ^{40}S events with exactly two γ rays detected in CAESAR. Both the x and y axes have 16-keV wide bins. The matrix is filled symmetrically. The 904-keV and 2452-keV transitions are in coincidence. 79

Figure 4.9: Background-subtracted, Doppler-corrected γ-ray spectrum for ^{40}S counts in coincidence with the 904-keV transition. A peak at 2452 keV is visible. 80

Figure 4.10: Top: feeding-subtracted angle-integrated cross section as a function of choice of scattering angle cut derived from the experimental data for the 2_1^+ state in ^{40}S (black). The red curve is the expected cross section assuming a $B(E2; 0_1^+ \rightarrow 2_1^+)$ strength of 284 e^{2}fm^4. Bottom: $B(E2; 0_1^+ \rightarrow 2_1^+)$ strength calculated using Alder-Winther theory for different choices of maximum scattering angle. 81

Figure 4.11: Doppler-corrected energy spectrum for ^{42}S gated on scattering angles smaller than 40 mrad in the laboratory frame. The blue curves are the individual components of the fit function derived from GEANT4 simulations along with a double exponential background. The red curve is the total fit function. 82

Figure 4.12: Doppler-corrected energy spectrum for ^{42}S for events where only one γ ray was detected by CAESAR. Nearest-neighbor addback was utilized. The 3000-keV transition from the 2_2^+ state to the ground state is visible. . . . 83

Figure 4.13: Doppler-corrected coincidence matrix for ^{42}S events with exactly two γ rays detected in CAESAR. Both the x and y axes have 16-keV wide bins. The matrix is filled symmetrically. The 903-keV transition is in coincidence with peaks at 2100 keV (more clearly observed in the projection of Figure 4.14) and 4150 keV. 84

Figure 4.14: Background-subtracted, Doppler-corrected γ-ray spectrum for ^{42}S counts in coincidence with the 903-keV transition. 85

Figure 4.15: Top: feeding-subtracted angle-integrated cross section as a function of choice of scattering angle cut derived from the experimental data for the 2_1^+ state in ^{42}S (black). The red curve is the expected cross section assuming a $B(E2; 0_1^+ \rightarrow 2_1^+)$ strength of 326 e^{2}fm^4. The blue data points are the experimental data with the correction for scattering angle explained in the text. Bottom: $B(E2; 0_1^+ \rightarrow 2_1^+)$ strength calculated using Alder-Winther theory for different choices of maximum scattering angle. 87

Figure 4.16: Doppler-corrected energy spectrum for ^{44}S gated on scattering angles smaller than 40 mrad in the laboratory frame. The blue curves are the individual components of the fit function derived from GEANT4 simulations along with a double exponential background. The red curve is the total fit function. 90

Figure 4.17: Doppler-corrected coincidence matrix for ^{44}S events with exactly two γ rays detected in CAESAR. Both the x and y axes have 16-keV wide bins. The matrix is filled symmetrically. The 1329-keV transition is in coincidence with the 949-keV transition. 91

Figure 4.18: Background-subtracted, Doppler-corrected γ-ray spectrum for ^{44}S counts in coincidence with the 1329-keV transition. 92

Figure 4.19: Top: feeding-subtracted angle-integrated cross section as a function of choice of scattering angle cut derived from the experimental data for the 2_1^+ state in ^{44}S (black). The red curve is the expected cross section assuming a $B(E2; 0_1^+ \rightarrow 2_1^+)$ strength of 221 e^{2}fm^4. Bottom: $B(E2; 0_1^+ \rightarrow 2_1^+)$ strength calculated using Alder-Winther theory for different choices of maximum scattering angle. 93

Figure 4.20: Top: Doppler-corrected energy spectrum for ^{43}S gated on scattering angles smaller than 40 mrad in the laboratory frame. The blue curves are the individual components of the fit function derived from GEANT4 simulations along with a double exponential background. The red curve is the total fit function. Bottom: Low-energy portion of the Doppler-corrected energy spectrum for ^{43}S. The wide feature present in the ^{43}S data that is not present for ^{38}S is due to the continuous decay of the 320-keV isomer at different points along the beam line. The large background at low energies is due to bremsstrahlung and other beam-correlated background. 98

Figure 4.21: Doppler-corrected energy spectrum for ^{43}S produced from one-neutron removal for addback events with exactly one or two detected γ rays. The labeled peaks were also observed in the high-resolution ^{9}Be(^{44}S,^{43}S)X data presented in [15]. 99

Figure 4.22: Background-subtracted, Doppler-corrected energy spectrum for ^{43}S measured with CAESAR in coincidence with 320-keV γ rays detected on the hodoscope at the S800 focal plane from the decay of the isomer. The CAESAR spectrum is for addback multiplicity one. 100

Figure 4.23: Top: feeding-subtracted angle-integrated cross section as a function of choice of scattering angle cut derived from the experimental data for the 977-keV state in ^{43}S (black). The red curve is the expected cross section assuming a $B(E2)$ strength of 91 e^{2}fm^4 from the ground state to the 977-keV level. Bottom: $B(E2)$ strength calculated using Alder-Winther theory for different choices of maximum scattering angle. 101

Figure 4.24: SDPF-MU predictions for $B(E2)$ strengths in e^{2}fm^4 for low-lying levels in ^{43}S compared with experimental results. Arrow widths are proportional to transition strength. 102

Figure 4.25: Doppler-corrected energy spectrum for ^{45}Cl gated on scattering angles smaller than 40 mrad in the laboratory frame. The blue curves are the individual components of the fit function derived from GEANT4 simulations along with a double exponential background. The red curve is the total fit function. 105

Figure 5.1: $B(E2; 0^+_1 \rightarrow 2^+)$ strengths in the even-even sulfur isotopes for the 2^+ states measured in this work compared to predictions from the SDPF-MU Hamiltonian for the first five 2^+ states. 107

Chapter 1

Introduction

1.1 Atomic Nuclei

The atomic nucleus is a quantum many-body system made up of neutrons and protons. Collectively, the electrically-neutral neutrons and positively-charged protons are known as nucleons. The nucleus consisting of N neutrons and Z protons, with a total of $A = N + Z$ nucleons, is commonly referred to using the notation ${}^{A}X(Z)$ where $X(Z)$ is the chemical symbol for the element with Z protons. Since protons carry a positive charge, they repel each other via the Coulomb interaction, which is proportional to $1/r^2$ where r is radial separation. Despite this repulsion, the nucleons in a nucleus are bound together due to the strong nuclear force.

Nucleons are composed of three valence quarks: two down quarks and one up quark (neutrons) or two up quarks and one down quark (protons). The strong interaction described by quantum chromodynamics confines the quarks that constitute the nucleons and is mediated by the exchange of gluons. At a distance of 1 fm = 10^{-15} m, which is on the order of the nucleon size, the strong force is roughly 100 times stronger than the Coulomb repulsion. While quarks and gluons carry color charge, nucleons are color neutral. The strong nuclear force that binds nucleons together within the nucleus is a residual of the fundamental strong interaction, analogous to the van der Waals force in chemistry between neutral atoms or

molecules which is a residual of the fundamental Coulomb interaction [16].

Figure 1.1 shows the central part of the nucleon-nucleon interaction. The strong nuclear force has a repulsive core at short distances but outside of the core is strongly attractive over a short range. At longer distances, the nucleon-nucleon potential can be modeled as the exchange of light mesons (systems composed of one quark and one antiquark) [17]. In addition to the scalar central part, the nucleon-nucleon interaction has a complex dependence on spin that can be decomposed into vector (spin-orbit) and tensor components. Nucleon-nucleon scattering experiments indicate that the strong nuclear force is approximately charge independent [18].

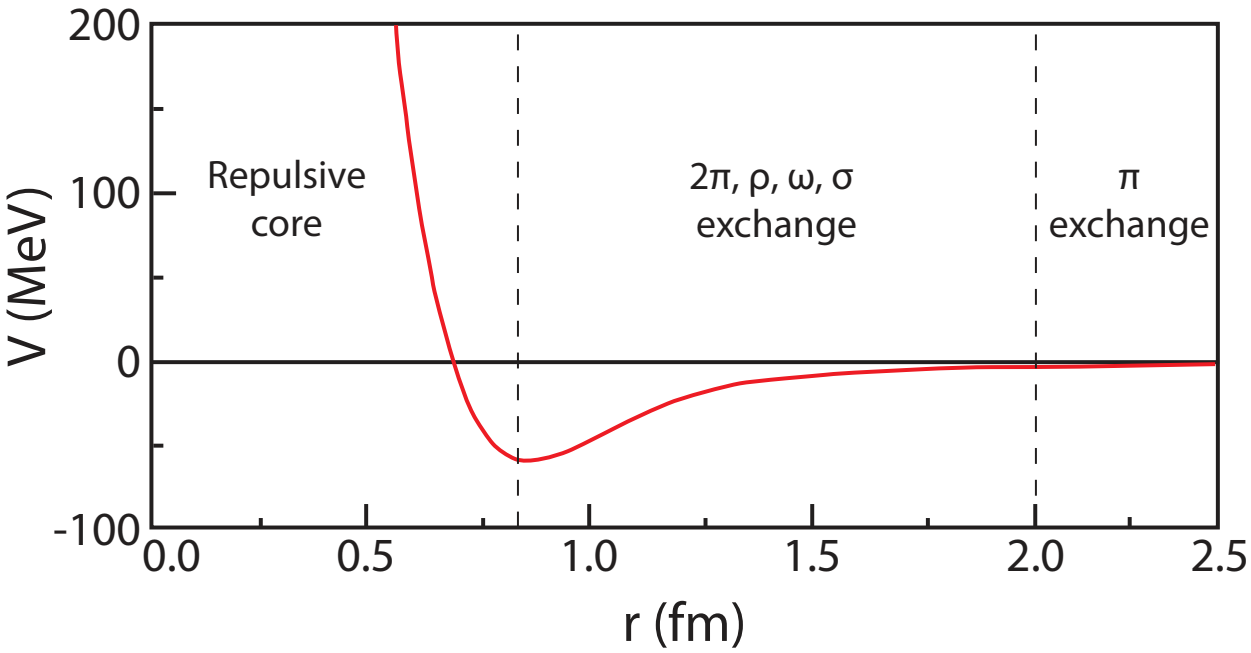

Figure 1.1: Central projection of the nucleon-nucleon interaction. Outside the repulsive core, the potential is attractive with rapidly diminishing strength. Over longer ranges, the central nuclear force can be modeled through exchange of massive particles called mesons. Figure modified from [1].

The interplay between the strong nuclear force and the Coulomb repulsion is apparent in the chart of the nuclides shown in Figure 1.2. The chart of the nuclides displays neutron

number on the x axis and proton number on the y axis with each square representing a different nucleus. Nuclei with the same Z, N, and A are referred to as isotopes, isotones, and isobars, respectively. Of the approximately 7000 nuclei predicted to exist [19], around 3000 have been observed experimentally. The stable nuclei (black squares) are situated in the region of the chart known as the valley of stability. As the proton number increases, the valley of stability bends away from the $N = Z$ line, where neutron-proton pairing dominates, toward the neutron-rich side as a result of the repulsive Coulomb force between protons.

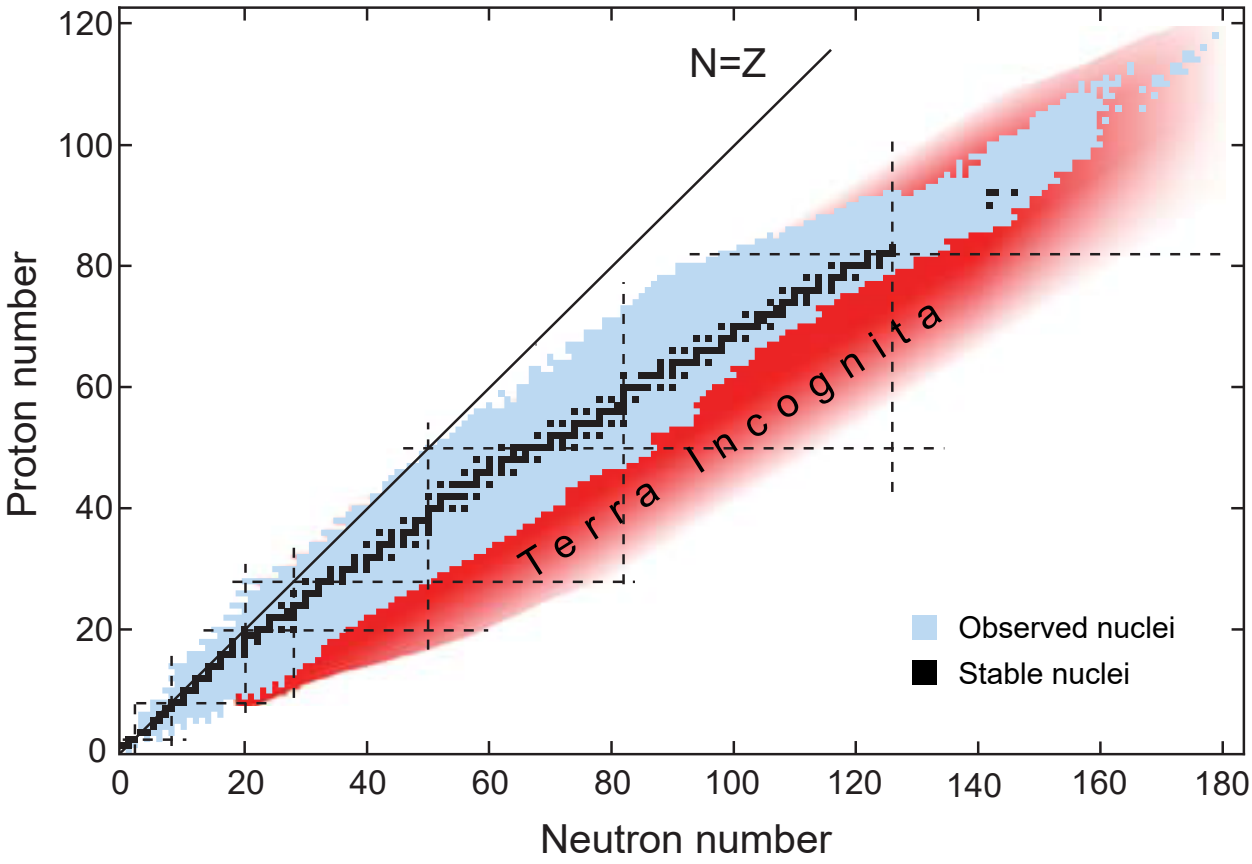

Figure 1.2: The chart of the nuclides with neutron number on the x axis and proton number on the y axis. Terra Incognita refers to the region of the chart with experimentally unobserved nuclei that are predicted to exist. The dotted lines indicate the traditional magic numbers of neutrons and protons discussed in the text. Figure adapted from [2].

One early framework for describing the nucleus is the liquid drop model. By approxi-

mating the nucleus as an incompressible fluid of nucleons, the nuclear binding energy can be calculated [20]. Due to the attractive and short-range nature of the nucleon-nucleon interaction, the interior matter density for nuclei is approximately constant (saturation). Therefore, the droplet energy, which increases linearly with volume, is proportional to the number of nucleons A. The nucleons at the surface, however, have fewer neighbors to interact with, so a correction term proportional to the surface area, which goes as $A^{2/3}$, must be added. The Coulomb energy is approximately proportional to $Z^2/A^{1/3}$. Since both neutrons and protons are fermions with intrinsic spin $s = 1/2$, they each obey the Pauli exclusion principle. Consequently, there is a term that penalizes neutron-proton asymmetry. Finally, the observed systematic odd-even staggering in binding energy is accounted for using a pairing term. Altogether, the semi-empirical mass formula for binding energy BE is:

$$BE = a_V A - a_S A^{2/3} - a_C \frac{Z^2}{A^{1/3}} - a_A \frac{(N-Z)^2}{A} + \delta(N,Z), \tag{1.1}$$

where

$$\delta(N,Z) = \begin{cases} a_P A^{-1/2} & N \text{ and } Z \text{ even} \\ 0 & A \text{ odd} \\ -a_P A^{-1/2} & N \text{ and } Z \text{ odd.} \end{cases} \tag{1.2}$$

The values of the coefficients for the volume term a_V, the surface term a_S, the Coulomb term a_C, the asymmetry term a_A, and the pairing term a_P are determined from fits to experimental mass data and the signs are chosen here to yield positive coefficients. The liquid drop model successfully reproduces the observed bend in the valley of stability shown in Figure 1.2 and is accurate to within 10 MeV for most nuclei while the average binding energy is about 8 MeV per nucleon.

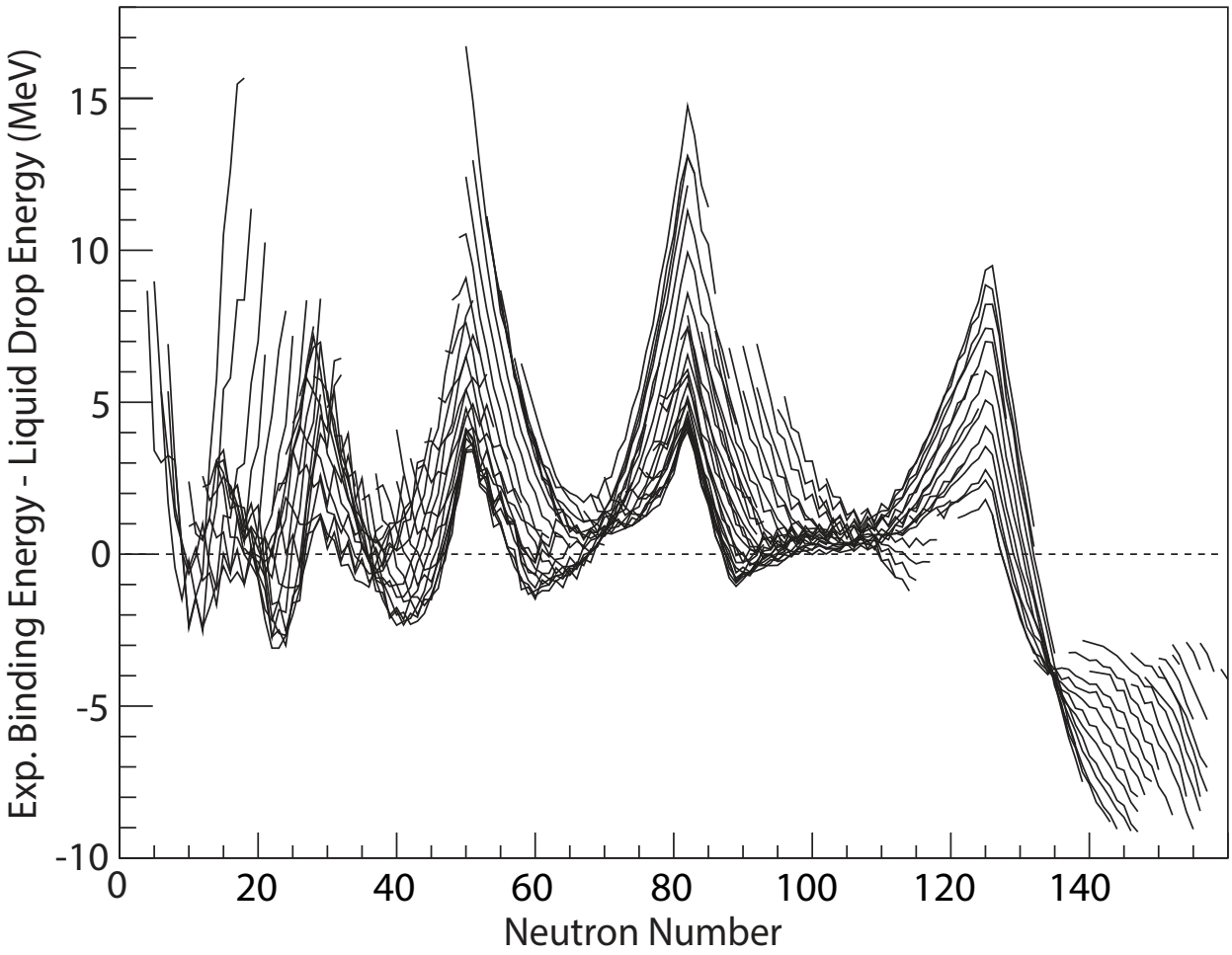

Figure 1.3: Differences between experimental binding energies and binding energies calculated using the liquid drop model for nuclei with $Z \geq 8$ as a function of neutron number. The peaks at $N = 28$, 50, 82, and 126 indicate that nuclei have internal structure. Figure taken from [3] with data from [4].

However, systematic deviations between the experimental and liquid-drop binding energies as a function of neutron number can be seen in Figure 1.3, suggesting that nuclei have internal structure that is not accounted for in this simple picture. The experimental nuclear binding energy is larger than predicted by this model for nuclei with neutron numbers 28, 50, 82, and 126. These neutron numbers, along with 2, 8, and 20, which are less clearly visible in Figure 1.3, are known as magic numbers. The same phenomenon can be observed for nuclei with magic numbers of protons. Nuclei with either a magic number of neutrons or

protons are referred to as singly-magic while nuclei with a magic number of both neutrons and protons are called doubly-magic.

1.2 Nuclear Shell Model

Efforts to explain the existence of the neutron and proton magic numbers lead to the development of the nuclear shell model [21, 22]. The shell model considers the motion of a single nucleon in a mean field generated by all the other nucleons in the nucleus. By solving the Schrödinger equation using this mean potential, the available single-particle orbitals and their corresponding quantized energy levels are obtained. These orbitals are filled according to the Pauli exclusion principle and the magic numbers correspond to large energy gaps between successive groups of close-lying orbitals called shells.

Neglecting the Coulomb interaction, the Hamiltonian for a nucleus with A nucleons can be written as:

$$H = \sum_{i=1}^{A} \frac{\mathbf{p}_i^2}{2m_i} + \sum_{i>k=1}^{A} V_{ik}(\mathbf{r}_i - \mathbf{r}_k), \tag{1.3}$$

assuming only two-body interactions between nucleons. Here $\mathbf{p}_i$ and m_i are the momentum and mass of each nucleon and V_{ik} is the two-body interaction between two nucleons. In the mean-field approximation of the shell model, the A nucleons do not interact with each other strongly and the system can be treated as A non-interacting nucleons in an external single-particle potential:

$$H = \left[\sum_{i=1}^{A}\left(\frac{\mathbf{p}_i^2}{2m_i} + U_i(\mathbf{r})\right)\right] + \left[\sum_{i>k=1}^{A} V_{ik}(\mathbf{r}_i - \mathbf{r}_k) - \sum_{i=1}^{A} U_i(\mathbf{r})\right] = H_0 + V_{res}. \tag{1.4}$$

The first term H_0 describes the motion in the mean field while the second term V_{res} is known

as the residual interaction.

A convenient starting guess for the mean-field potential, the form of which is not known exactly, is the three-dimensional harmonic oscillator:

$$U(r) = \frac{1}{2}\mu\omega^2 r^2, \tag{1.5}$$

where μ is the reduced mass of the system and ω is the oscillator frequency. The energy levels for H_0 in this case depend only on the radial quantum number n, the orbital angular momentum quantum number l, and the choice of ω:

$$E_{nl} = \left(2n + l + \frac{3}{2}\right)\hbar\omega = \left(N + \frac{3}{2}\right)\hbar\omega. \tag{1.6}$$

Here, $\hbar$ is the reduced Planck constant. The three-dimensional harmonic oscillator successfully reproduces the first few magic numbers (2, 8, and 20) but fails to reproduce the other magic numbers, as shown Figure 1.4 for the neutron single-particle energy levels of ^{208}Pb.

Unlike the short-range nucleon-nucleon interaction, the harmonic oscillator potential goes to infinity as the radial distance increases. A more realistic form for the mean-field generated by all the nucleons is the Woods-Saxon potential:

$$U(r) = \frac{-U_0}{1 + e^{(r-R)/a}}, \tag{1.7}$$

where U_0 is the potential depth, the nuclear radius is $R = r_0 A^{1/3}$, and a is the diffuseness. Although the Woods-Saxon potential breaks the degeneracy of orbitals with the same principle harmonic oscillator quantum number $N = 2n + l$, Figure 1.4 shows that this potential also fails to reproduce the experimentally-observed magic numbers larger than 20.

Adding a strongly attractive spin-orbit coupling term [21, 22],

$$U_{so}(r, \vec{l}, \vec{s}) = -U_{so}(r)(\vec{l} \cdot \vec{s}), \tag{1.8}$$

to the Woods-Saxon potential lifts the degeneracy for states with the same orbital angular momentum quantum number l and the gaps in energy between shells formed by the close-lying orbitals shown in Figure 1.4 successfully explain the experimentally-observed magic numbers. Similar results are obtained for the proton single-particle orbitals.

The single-particle orbitals are labeled by their quantum numbers n, l, and j using the notation nl_j. The radial quantum number $n = 0, 1, 2, \ldots$ counts the number of radial nodes in the wavefunction. The orbital angular momentum quantum number l is often referred to using spectroscopic notation where the labels $l = s, p, d, f, g, h, \ldots$ represent $l = 0, 1, 2, 3, 4, 5, \ldots$, respectively. The maximum value of l is the principle quantum number N. The nucleon spin $\vec{s}$ couples with the orbital angular momentum $\vec{l}$ to the total angular momentum $\vec{j} = \vec{l} + \vec{s}$, giving the total angular momentum quantum number $j = l \pm 1/2$. Each orbital has $2j+1$ magnetic substates, running over $m_j = -j, \ldots, j$ in integer steps, and accordingly can hold a maximum of $2j + 1$ neutrons or protons due to the Pauli exclusion principle. Note that neutrons and protons are distinguishable and can share the same set of quantum numbers.

The states of the nucleus itself are characterized by their spin-parities J^π. The parity π of a single-particle state indicates whether the wavefunction changes sign under inversion of all the spatial coordinates and is given by $(-1)^l$. For the nucleus itself, the total parity is the product of the parities of the occupied single-particle levels. Similarly, the total angular momentum J of the nucleus is found by coupling the spins $\vec{j}$ of all the occupied single-

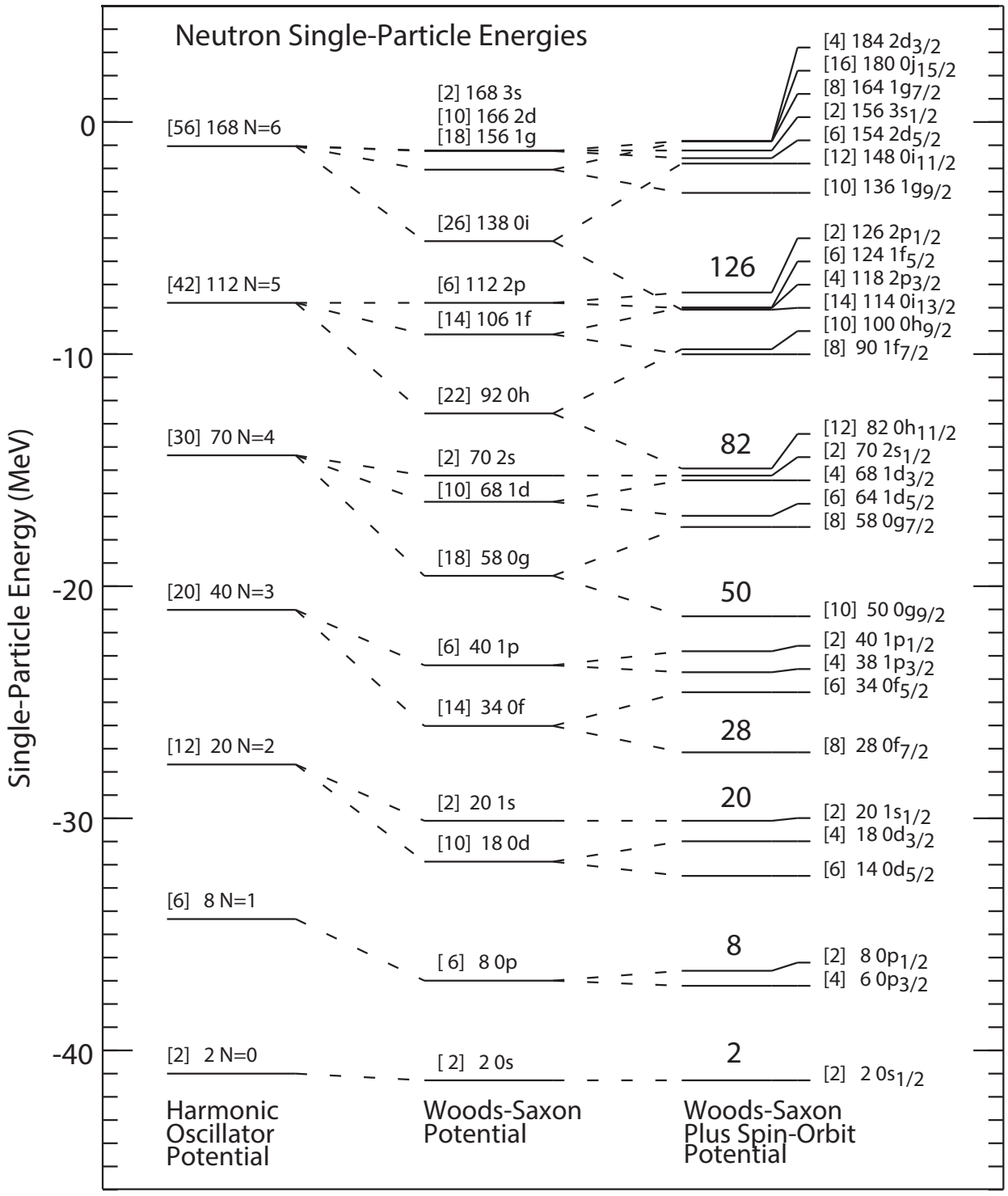

Figure 1.4: Energies of neutron single-particle orbitals calculated for ^{208}Pb using different mean field potentials: three-dimensional harmonic oscillator, Woods-Saxon, and Woods-Saxon plus spin-orbit. The number in brackets is the maximum number of neutrons allowed in the orbital by the Pauli principle and the number outside the brackets is the sum of total allowed nucleons through this orbital. Orbitals are labeled by their quantum numbers. Figure is adapted from [5].

particle states. For a completely filled orbital, the nucleons couple to spin-parity 0^+. If all of the orbitals in a shell are full, then the shell is called closed and the J^π of the nucleus is determined by the remaining valence nucleons above the closed shell. For example, ^{17}O has one valence neutron in the $0d_{5/2}$ orbital with respect to doubly-magic ^{16}O and the spin-parity of its ground state is $5/2^+$. Furthermore, energy is typically minimized when nucleons in the same orbital form pairs that couple to 0^+. In fact, the spin-parity of the ground state for all nuclei with even numbers of both neutrons and protons (even-even nuclei) is 0^+ [23]. Typically, within this scheme, only nucleons outside of a so-called core are allowed to contribute to nuclear excitations. Due to the properties of closed shells described above and the large energy gaps at magic numbers, it is common to choose a core that corresponds to a doubly-magic nucleus.

The nuclear shell model describes the properties of nuclei in the single-particle picture and is therefore most successful near shell closures where the structure is dominated by only a few nucleons outside a closed core. In this framework, nuclear excited states are formed by rearranging one or a few nucleons in their orbitals. For example, in this simple picture, the $1/2^+$ first excited state of ^{17}O arises from the promotion of the valence neutron in the $0d_{5/2}$ orbital to the $1s_{1/2}$ orbital. However, away from closed shells nuclei exhibit collective behavior where many valence nucleons contribute coherently to nuclear excitations.

1.3 Collective Models

The excitation patterns in collective nuclei can be explained using macroscopic geometric models of the nucleus that describe vibrations and rotations. In the vibrational model, even-even nuclei have evenly-spaced energy levels associated with oscillations of an incompressible

liquid-drop nucleus about an average spherical shape. The first excited state has spin-parity 2^+ and the energy of a single phonon, the elementary excitation in the quantum-mechanical treatment of the surface vibrations on the liquid drop. The second excited state is a triplet of nearly-degenerate levels with $J^\pi = 0^+, 2^+, 4^+$ at twice the energy of the first excited state and comes from the coupling of two phonons. The three-phonon states, at three times the energy of the first excited state, are a nearly-degenerate quintet with $J^\pi = 0^+, 2^+, 3^+, 4^+, 6^+$ [23].

If an even-even nucleus is rigidly deformed, the excitation energies can be calculated as those of a quantum-mechanical rigid rotor:

$$E_{rot}(J) = \frac{\hbar^2}{2I} J(J+1), \tag{1.9}$$

where I is the moment of inertia of the nucleus and J is even. Note that these rotations are about an axis perpendicular to the symmetry axis of the deformed nucleus. As shown in Figure 1.5, even-even nuclei evolve from displaying signs of magicity near closed shells (e.g. high-lying first-excited 2^+ states) to spherically vibrational just outside of closed shells to deformed and rotational with low-lying first-excited 2^+ states near mid-shell. The ratio $R_{4/2}$ of energies for the first 2^+ and 4^+ states provides evidence for the type of collective motion: $R_{4/2} = 2$ for vibrations while $R_{4/2} = 3.33$ for rotations from Equation 1.9 [23]. The collective models described in this section can be extended to systems with odd numbers of nucleons by coupling the unpaired nucleons to the vibrator or rotor (particle-rotor models).

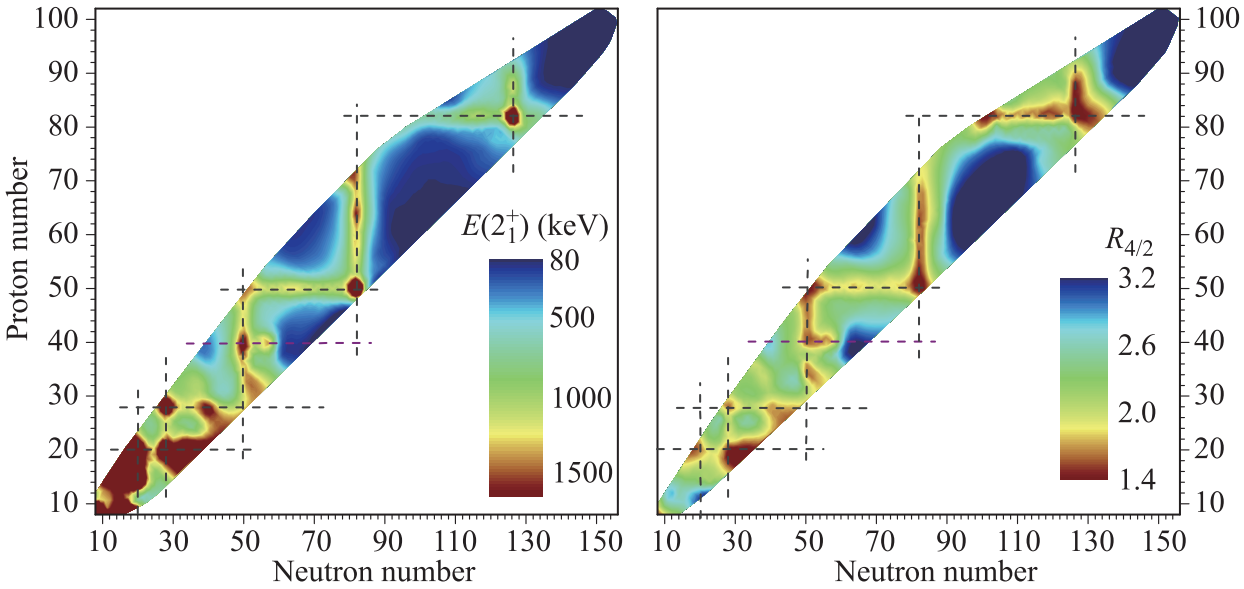

Figure 1.5: Energies of the first 2^+ excited state and ratios $R_{4/2}$ of energies for the first 2^+ and 4^+ states in even-even nuclei across the chart of nuclides. The neutron and proton magic numbers are denoted by dashed lines. Figure taken from [6].

1.4 Electromagnetic Transitions

The properties of low-lying bound excited states in nuclei can be used to probe collectivity, which is a measure of how many nucleons are involved in the excitation. The majority of nuclear excited states bound to particle emission will decay to a lower-energy level via the emission of a photon known as a γ ray. Neglecting the small recoil energy of the nucleus, the energy of this electromagnetic radiation is equal to the difference in energy of the initial and final states.

Electromagnetic transitions are characterized by their multipolarity λ and parity. Since the photon is a boson with intrinsic spin 1, the total angular momentum λ it carries cannot be 0. The allowed multipolarities for the γ ray are constrained by the spins of the initial

state (J_i) and final state (J_f) due to conservation of angular momentum:

$$\left|J_i - J_f\right| \leq \lambda \leq J_i + J_f. \tag{1.10}$$

Generally, transitions are referred to as 2^λpole: $\lambda = 1$ is dipole, $\lambda = 2$ is quadrupole, $\lambda = 3$ is octupole, and so on. In order to conserve parity, the following relation between the parity of the initial state (π_i), the parity of the final state (π_f), and the parity of the γ ray must be satisfied:

$$\pi_i \pi_f = \pi_\sigma (-1)^\lambda. \tag{1.11}$$

For electric transitions ($\sigma = E$), $\pi_\sigma = 1$ and for magnetic transitions ($\sigma = M$), $\pi_\sigma = -1$. Transitions are often labeled using the scheme $\sigma\lambda$. For instance, the allowed transitions for $\pi_i\pi_f = 1$ are $M1, E2, M3, E4, \ldots$ and the allowed transitions for $\pi_i\pi_f = -1$ are $E1, M2, E3, M4, \ldots$ for all λ allowed by Equation 1.10.

The electric transition operator can be written as:

$$\mathcal{O}(E\lambda) = \sum_i^A r_i^\lambda Y_\mu^\lambda(\theta, \phi) e_i e, \tag{1.12}$$

where $Y_\mu^\lambda(\theta, \phi)$ are the spherical harmonics, μ is the z-projection of λ, and $e_i e$ is the electric charge of the ith nucleon. For free neutrons, $e_n = 0$ and for free protons, $e_p = 1$. Effective charges for the nucleons can also be used to compensate for model space truncation in shell model calculations [5]. The magnetic transition operator can be written as:

$$\mathcal{O}(M\lambda) = \sum_i^A \left[\frac{2g_{li}}{\lambda + 1}\vec{l_i} + g_{si}\vec{s_i}\right] \vec{\nabla}\left[r^\lambda Y_\mu^\lambda(\theta, \phi)\right] \mu_N, \tag{1.13}$$

where g_{li} and g_{si} are the orbital and spin g-factors for the ith nucleon and $\mu_N = 0.105\ e\text{fm}$ is the nuclear magneton. The g-factors for free neutrons are $g_{ln} = 0$ and $g_{sn} = -3.826$ and the g-factors for free protons are $g_{lp} = 1$ and $g_{sp} = 5.586$. Effective values for the g-factors can also be used to take into account model-space truncation [5].

The electromagnetic transition rate W between an initial state with wavefunction $|J_i M_i\rangle$ and final state with wavefunction $|J_f M_f\rangle$ can be calculated as a sum over the allowed electric and magnetic transition operators using time-dependent perturbation theory:

$$W_{M_i,M_f,\mu} = \sum_{\sigma\lambda} \left(\frac{8\pi(\lambda+1)}{\lambda[(2\lambda+1)!!]^2} \right) \frac{1}{\hbar} \left(\frac{E_\gamma}{\hbar c} \right)^{2\lambda+1} \left| \langle J_f M_f \left| \mathcal{O}(\sigma\lambda)_\mu \right| J_i M_i \rangle \right|^2 . \tag{1.14}$$

Here, c is the speed of light in vacuum. Averaging over the initial magnetic substates M_i and summing over the projections μ and the final magnetic substates M_f, which are not typically observed individually in experiments, results in:

$$W = \frac{1}{2J_i+1} \sum_{M_i} \sum_{M_f,\mu} W_{M_i,M_f,\mu} \tag{1.15}$$

$$= \sum_{\sigma\lambda} \left(\frac{8\pi(\lambda+1)}{\lambda[(2\lambda+1)!!]^2} \right) \frac{1}{\hbar} \left(\frac{E_\gamma}{\hbar c} \right)^{2\lambda+1} \frac{\left| \langle J_f \left|| \mathcal{O}(\sigma\lambda) \right|| J_i \rangle \right|^2}{2J_i+1}, \tag{1.16}$$

through use of the Wigner-Eckart theorem and the orthogonality properties of the Clebsch-Gordan coefficients [5]. The last factor in this expression is defined as the reduced transition probability:

$$B(\sigma\lambda; J_i \to J_f) \equiv \frac{\left| \langle J_f \left|| \mathcal{O}(\sigma\lambda) \right|| J_i \rangle \right|^2}{2J_i+1}. \tag{1.17}$$

The double-bar notation of the Wigner-Eckart theorem for the reduced matrix element $\langle J_f \left|| \mathcal{O}(\sigma\lambda) \right|| J_i \rangle$ signifies that there is no dependence on M_i, μ, or M_f.

For γ decay, the initial state is higher in energy than the final state. Conversely, through Coulomb excitation, a projectile nucleus can be inelastically excited due to electromagnetic interaction with a target nucleus. Consider two states J_a and J_b. From Equation 1.17, the relation between the reduced transition probabilities in each direction is:

$$B(\sigma\lambda; J_b \rightarrow J_a) = \frac{2J_a + 1}{2J_b + 1} B(\sigma\lambda; J_a \rightarrow J_b). \tag{1.18}$$

From examination of Equation 1.16, it can be seen that the lowest allowed multipolarities dominate the transition rate W. For a typical γ-ray energy of 1 MeV, the rate for the next allowed electric (magnetic) multipole, $\lambda + 2$, is about seven orders of magnitude smaller than the rate for the lowest allowed electric (magnetic) multipole λ [5]. For transitions that can occur via both low-multipole electric and magnetic transitions, it is useful to define a multipole mixing ratio δ. For example, for electromagnetic transitions that can occur via $M1$ and $E2$:

$$\delta^2(E2/M1) = \frac{W_{E2}}{W_{M1}}, \tag{1.19}$$

and the branching fractions b are:

$$b(E2) = \frac{W_{E2}}{W_{M1} + W_{E2}} = \frac{\delta^2}{1 + \delta^2}, \tag{1.20}$$

$$b(M1) = \frac{W_{M1}}{W_{M1} + W_{E2}} = \frac{1}{1 + \delta^2}. \tag{1.21}$$

For even-even nuclei, the reduced electric quadrupole strength from the first 2^+ state to the ground state, $B(E2; 2_1^+ \rightarrow 0_1^+)$, is an indicator of collectivity. This strength can be expressed in terms of the Weisskopf unit, which is an estimate of the $B(E2; 2_1^+ \rightarrow 0_1^+)$ for a

single particle. In general, the Weisskopf units are given by [5]:

$$B_W(E\lambda) = \left(\frac{1}{4\pi}\right)\left[\frac{3}{3+\lambda}\right]^2 (1.2A^{1/3})^{2\lambda}\ e^2\mathrm{fm}^{2\lambda}, \tag{1.22}$$

$$B_W(M\lambda) = \left(\frac{10}{\pi}\right)\left[\frac{3}{3+\lambda}\right]^2 (1.2A^{1/3})^{2\lambda-2}\ \mu_N^2\mathrm{fm}^{2\lambda-2}. \tag{1.23}$$

$B(E2; 2_1^+ \rightarrow 0_1^+)$ strengths are largest at mid-shell and smallest near closed shells. Accordingly, there is also a link between the deformation in the rotational model and the reduced electric quadrupole strength. For an axially-symmetric quadrupole deformed nucleus, the deformation can be expressed using the Hill-Wheeler parameterization [24]:

$$R(\theta) = R_0\left(1 + \beta Y_0^2(\theta, 0)\right), \tag{1.24}$$

where the radius $R_0 = r_0 A^{1/3}$, $Y_0^2(\theta, 0)$ is a spherical harmonic, and β is the quadrupole deformation parameter. If β is positive, the nucleus has prolate deformation and if β is negative, the nucleus has oblate deformation. The magnitude of the quadrupole deformation parameter is related to the $B(E2; 0_1^+ \rightarrow 2_1^+)$ excitation strength:

$$|\beta| = \frac{4\pi}{3ZeR_0^2}\sqrt{B(E2; 0_1^+ \rightarrow 2_1^+)}. \tag{1.25}$$

1.5 Configuration Interaction Method

Going beyond the independent particle picture by including the residual interactions of Equation 1.4 in the nuclear shell model is required in order to perform predictive calculations of nuclear properties. However, solving the Schrödinger equation for all the nucleons in a

nuclear system as large as ^{42}Si, for example, is not feasible computationally. Instead, an inert core of A_{core} nucleons, often taken as a nearby doubly-magic nucleus, is utilized to simplify the problem. Only the $A - A_{core}$ valence nucleons outside of the core are allowed to contribute to the nuclear excitations. Furthermore, a model space limiting the available single-particle orbitals for the valence nucleons must be chosen.

The excitation energies for nuclear states are calculated through diagonalization of an effective interaction expressed in matrix form. Omitting higher-body terms, the Hamiltonian can be written as a series of zero-, one-, and two-body operators in the form $H = H_0 + H_1 + H_2$ where H_0 is the binding energy of the core, H_1 is a one-body operator with matrix elements given by the single-particle energies multiplied by the orbital occupancies, and H_2 is the two-body part [5]. The two-body matrix elements can be written in terms of the residual interaction as $\langle ab\,|V_{res}|\,cd\rangle_{JT}$ where the nucleons in orbits a, b and c, d, respectively, are coupled to total spin J and isospin T. The wavefunctions for the nuclear states found by diagonalizing the matrix are linear combinations of the different configurations of nucleons possible in the model space given the number of neutrons and protons in the nucleus, giving rise to the name "Configuration Interaction" for the method. The average number of nucleons in an orbital for a given shell-model state from the calculation is referred to as the orbital's occupancy. Two examples of Hamiltonians used in the configuration-interaction framework are SDPF-MU [25] and SDPF-U [26] which are described in detail in the following section.

1.6 Breakdown of the N=28 Magic Number

Studies of nuclei far from the valley of stability have revealed surprising changes in nuclear structure. For example, in some regions of the chart of the nuclides, the conventional magic

numbers disappear and new magic numbers emerge [27]. In particular, the neutron-rich silicon and sulfur isotopes approaching the conventional neutron magic number $N = 28$ have attracted much experimental and theoretical attention that has provided great insight into the evolution of shell structure in exotic nuclei. Recall that magic nuclei characteristically have high-lying first 2^+ excited states and small $B(E2; 0_1^+ \rightarrow 2_1^+)$ values. The first evidence for the breakdown of the $N = 28$ magic number was provided by the observation of moderate deformation in ^{40,42}S [28] and low-lying quadrupole collectivity in ^{44}S [29]. Figure 1.6 shows the systematic trends in the energies of first 2^+ excited states $E(2_1^+)$ and $B(E2; 0_1^+ \rightarrow 2_1^+)$ strengths across the Ca ($Z = 20$), Ar ($Z = 18$), S ($Z = 16$), and Si ($Z = 14$) isotopic chains. The Ca isotopes show the tell-tale signs of magicity at both $N = 20$ and $N = 28$ while the Ar isotopes at $N = 20$ and $N = 28$ only show small relative peaks in $E(2_1^+)$. However, for S and Si near $N = 28$, the $E(2_1^+)$ values are low and the $B(E2; 0_1^+ \rightarrow 2_1^+)$ strengths are large relative to their values closer to stability near $N = 20$. This provides evidence that while the conventional neutron magic number $N = 20$ holds for these nuclei, $N = 28$ is no longer a magic number at $Z = 14$ and $Z = 16$.

Reproducing the evolution of the $N = 28$ shell gap in the vicinity of ^{42}Si has been a major endeavor for modern nuclear shell model calculations. The mechanism driving the breakdown of $N = 28$ as a magic number in this region has been attributed to the neutron-proton monopole component of the tensor part of the nucleon-nucleon interaction [30]. Consider a nucleon in a single-particle orbit with spin j_a. The single-particle energy of this nucleon depends on the mean field generated by all the other nucleons in the nucleus, which changes when a nucleon is added to the orbit with spin j_b. The nucleons in the two orbitals couple to total spin J. The shift in energy of the single-particle orbital for a proton

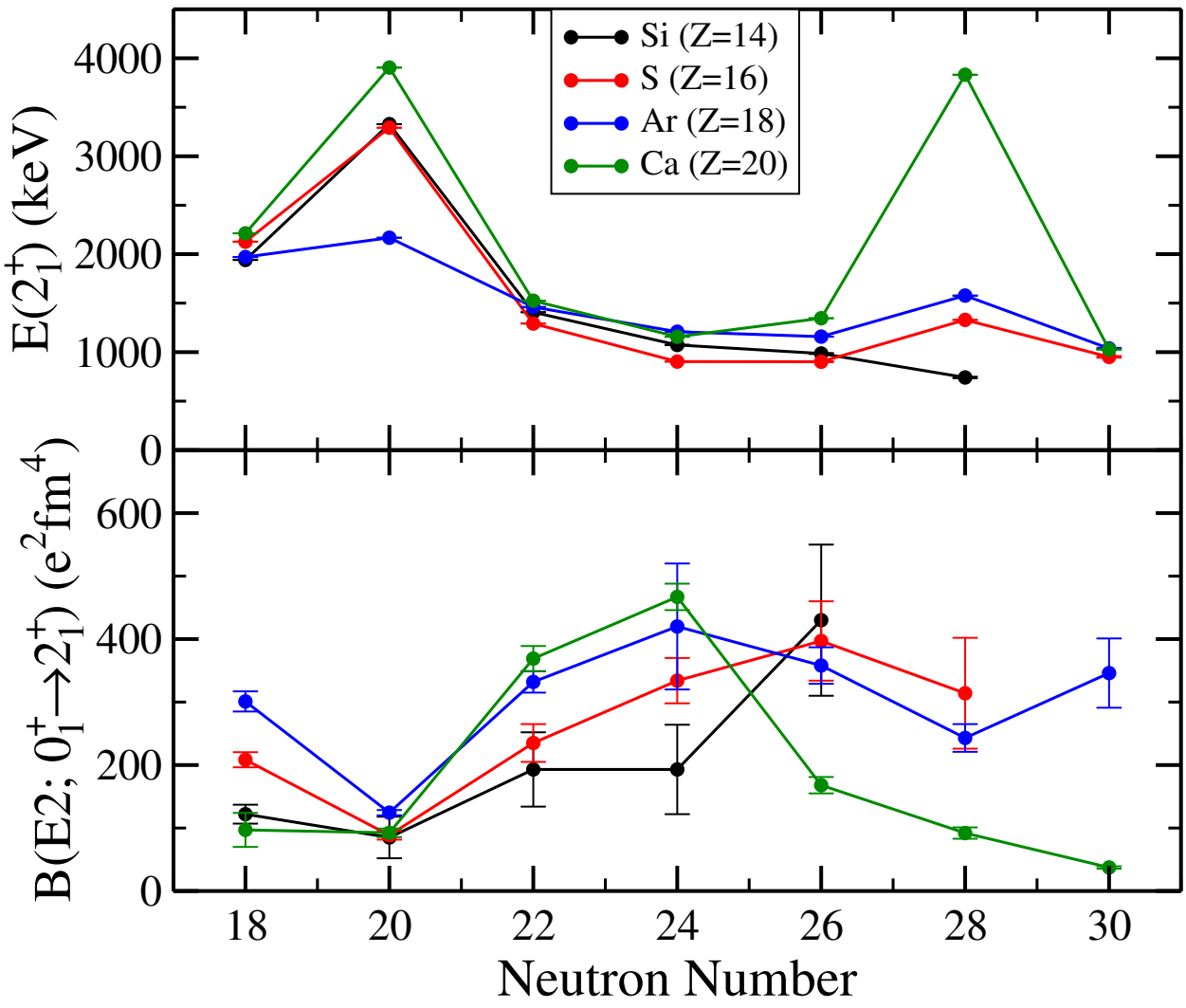

Figure 1.6: Experimental energies of the first 2^+ states [7] (top) and $B(E2; 0_1^+ \rightarrow 2_1^+)$ strengths [8] (bottom) for Si, S, Ar, and Ca isotopes showing the evolution of collectivity around the conventional neutron magic numbers $N = 20$ and $N = 28$.

in the orbital with spin j_a due to neutrons in the orbital with spin j_b is [9]:

$$\Delta\epsilon_p(j_a) = \frac{1}{2}\left[\bar{V}_{ab}^{T=0} + \bar{V}_{ab}^{T=1}\right] n_n(j_b), \tag{1.26}$$

where $n_n(j_b)$ is the number of neutrons in the orbital with j_b and $j_a \neq j_b$. Here, $\bar{V}_{ab}^{T}$ is the

angle-averaged (monopole) tensor interaction between the orbitals:

$$\bar{V}^T_{ab} = \frac{\sum_J (2J+1)\langle j_a j_b \,|V|\, j_a j_b\rangle_{JT}}{\sum_J (2J+1)}. \tag{1.27}$$

Above, T is the isospin quantum number for the coupled nucleons where the projection $T_z = \frac{1}{2}(N-Z)$. $T = 0$ for the neutron-proton interaction and $T = 1$ for the neutron-neutron and proton-proton interactions. The $T = 0$ component of the tensor interaction is stronger [9].

For a single nucleon with a given value of orbital angular momentum l, there are two possible values for the total angular momentum j: $j_< = l - \frac{1}{2}$ and $j_> = l + \frac{1}{2}$. The tensor interaction between orbitals with $j_a = j_<$ and $j_b = j'_>$ and with $j_a = j_>$ and $j_b = j'_<$ is attractive while the tensor interaction between orbitals with $j_a = j_<$ and $j_b = j'_<$ and with $j_a = j_>$ and $j_b = j'_>$ is repulsive. From $N = 20$ to $N = 28$, the neutron $0f_{7/2}(j_>)$ orbital is filled. The tensor force between the neutron $0f_{7/2}(j_>)$ orbital and the proton $0d_{5/2}(j_>)$ orbital is repulsive while the tensor force between the neutron $0f_{7/2}(j_>)$ orbital and the proton $0d_{3/2}(j_<)$ orbital is attractive. Therefore, as shown schematically in Figure 1.7, the $Z = 14$ sub-shell gap is reduced as the neutron $0f_{7/2}(j_>)$ orbital is filled.

At the same time, removing protons from the filled $0d_{3/2}(j_<)$ orbital in ^{48}Ca causes the energy of the neutron $0f_{7/2}(j_>)$ orbital to increase since the attractive interaction is weakened. This energy shift is larger than the energy shift due to the weakening of the attractive interaction between the proton $0d_{3/2}(j_<)$ orbital and the neutron $1p_{3/2}(j_>)$ orbital, resulting in a reduction of the $N = 28$ shell gap. The simultaneous narrowing of the $Z = 14$ and $N = 28$ shell gaps leads to mutually-enhanced deformation in the region surrounding ^{42}Si. The origin of this deformation has been argued in the context of a tensor-force-driven

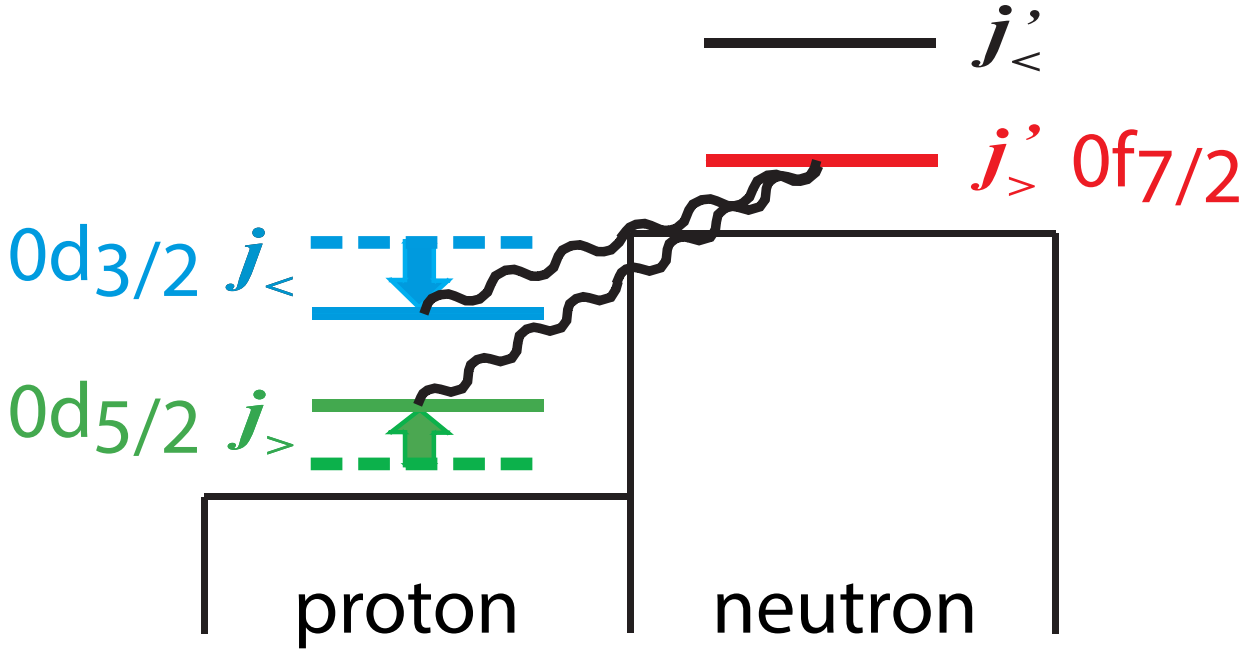

Figure 1.7: Schematic illustration of the tensor force. The repulsive interaction between the neutron $0f_{7/2}(j_>)$ orbital and proton $0d_{5/2}(j_>)$ and the attractive interaction between the neutron $0f_{7/2}(j_>)$ orbital and proton $0d_{3/2}(j_<)$ orbital reduce the $Z = 14$ sub-shell gap. Figure modified from [9].

Jahn-Teller effect [25] and within the context of SU(3)-like models of quadrupole correlations [26, 31, 32].

The SDPF-MU effective interaction was constructed to describe the shell and shape evolution in the S and Si isotopic chains toward $N = 28$ [25]. The valence space for the SDPF-MU Hamiltonian includes the proton $0d_{5/2}$, $1s_{1/2}$, and $0d_{3/2}$ orbitals (sd shell) and the neutron $0f_{7/2}$, $1p_{3/2}$, $0f_{5/2}$, and $1p_{1/2}$ orbitals (pf shell). The interactions within the sd shell are taken from the USD Hamiltonian [33, 34] except for the monopole interactions $V^{T=0,1}_{0d_{3/2},0d_{5/2}}$ which were taken from SDPF-M [35]. The interactions within the pf shell are taken from the GXPF1B Hamiltonian [36] except for the monopole and quadrupole pairing matrix elements $\langle 0f_{7/2}0f_{7/2}\,|V|\,0f_{7/2}0f_{7/2}\rangle_{J=0,2}$ which were taken from KB3, another pf-shell Hamiltonian [37]. Both the USD and GXPF1B effective interactions use the harmonic oscillator basis and

start with a set of single-particle energies and two-body matrix elements derived from the nucleon-nucleon interaction that are then allowed to vary to better reproduce experimental data. The cross-shell interactions between the neutrons and protons are based on the V_{MU} interaction [38], which consists of a Gaussian central force, a two-body spin-orbit force taken from the M3Y interaction [39], and a tensor force comprised of π and ρ meson exchanges.

Another shell-model interaction that has been successful in describing nuclei near $N = 28$ is the SDPF-U Hamiltonian [26]. SDPF-U also uses the USD interaction [33, 34] for protons in the *sd* shell and a variant of the KB3 interaction [37] for neutrons in the *pf* shell. The proton-neutron cross-shell matrix elements are taken from the Kahana-Lee-Scott G matrix [40] with adjusted monopole terms to better fit experimental data. SDPF-U has two formulations, one to be used for $Z \leq 14$ and one for $Z \geq 15$ with differences due to consideration of proton excitations into the *pf* shell. The SDPF-U-MIX interaction extends SDPF-U to include the *sd* shell for neutrons in addition to the *fp* shell [32].

1.7 Motivation for Studying the Neutron-Rich Sulfur Isotopes

The breakdown of the magic number $N = 28$ discussed in the previous section is accompanied by interesting changes in nuclear shell structure. For example, consider ^{43}S, which has 16 protons and 27 neutrons. If the single-particle orbitals are filled in their normal order then the one unpaired neutron will occupy the $0f_{7/2}$ orbital. Consequently, the ground state of ^{43}S should have a spin-parity of $7/2^-$. However, the ground state of ^{43}S has been determined to be $3/2^-$ [41, 42]. In a simple shell-model picture, this corresponds to promoting the unpaired neutron from the $0f_{7/2}$ orbital into the $1p_{3/2}$ orbital. Similarly, for even-even nuclei like ^{42}Si

and ^{44}S, the ground state would be expected to have a completely filled neutron $0f_{7/2}$ orbital. Instead, shell-model calculations suggest that the dominant configuration for the ground state has two neutrons promoted to the $1p_{3/2}$ orbital, leaving two holes in the $0f_{7/2}$ orbital. Due to deformation, the energies of these so-called intruder configurations, which normally correspond to excited states, are lower than the energies of the spherical normal-order configurations. For this reason, the nuclei surrounding ^{42}Si and ^{44}S are said to belong to the so-called $N = 28$ island of inversion [32]. Typically, the excited states with structure dominated by the spherical normal-order configuration are at low excitation energy with respect to the deformed ground state leading to a phenomenon known as shape coexistence. The concept of an island of inversion is not restricted to the neutron-rich nuclei around the conventional magic number $N = 28$. Historically, the first island of inversion investigated was at $N = 20$ centered around ^{32}Mg and it is now known that there are islands of shell breaking for neutron-rich nuclei associated with normal-order shell closures and sub-shell closures at $N = 8$, 14, 20, and 28 and the harmonic oscillator magic number $N = 40$ [43].

With ^{44}S lying near the center of the island of inversion at $N = 28$, it is of interest to systematically study the structure of the sulfur isotopes with neutron numbers between 22 and 28 in order to gain understanding of the details of the mechanism driving shell evolution in this region. Due to their importance, the even-even neutron-rich sulfur isotopes beyond the heaviest stable isotope of sulfur at $N = 20$ have been studied using a variety of experimental techniques. Levels in radioactive ^{38}S have been studied using β decay, proton scattering, two-neutron transfer, two-proton transfer, intermediate-energy Coulomb excitation, and in-beam γ-ray spectroscopy following fragmentation of ^{48}Ca [7]. States in ^{40}S have been studied using β decay, proton scattering, four-neutron transfer, intermediate-energy Coulomb excitation, and in-beam γ-ray spectoscopy following fragmentation of ^{48}Ca and ^{46}Ar [7]. ^{42}S

has been studied using β decay, intermediate-energy Coulomb excitation, and in-beam γ-ray spectroscopy following fragmentation of ^{48}Ca, fragmentation of ^{46}Ar, and knockout from ^{44}Cl [7]. Finally, ^{44}S has been studied using intermediate-energy Coulomb excitation, in-beam γ-ray spectroscopy following fragmentation of ^{48}Ca, following two-proton knockout from ^{46}Ar, and following one-proton knockout from ^{45}Cl [7]. In particular, lifetime measurements in ^{44}S [44, 45] and supporting theoretical calculations [46, 47] have established the coexistence of levels dominated by zero-, one-, and two-neutron particle-hole configurations.

In a recent in-beam γ-ray spectroscopy measurement, an interesting systematic trend for the $2_2^+ \rightarrow 0_1^+$ and $2_2^+ \rightarrow 2_1^+$ γ-ray branching ratios in the sulfur isotopic chain was observed by Lunderberg *et al.* and discussed in comparison with shell-model calculations [10]. The SDPF-MU interaction predicts that for ^{38}S and ^{40}S, the $2_2^+ \rightarrow 2_1^+$ transitions will dominate with 96.4% and 99.4% branching ratios, respectively. In ^{42}S, the reverse occurs with a prediction of 84.2% for the $2_2^+ \rightarrow 0_1^+$ transition and only 15.8% for the $2_2^+ \rightarrow 2_1^+$ transition. These shell-model predictions were validated experimentally with the non-observation of the $2_2^+ \rightarrow 0_1^+$ branch in ^{38}S [10, 48] and a measurement of 85(2)% for the tentative $(2_2^+) \rightarrow 0_1^+$ branch in ^{42}S [10]. Shell-model calculations link the abrupt change in decay pattern for ^{42}S with the difference in occupancies for the neutron $0f_{7/2}$ and $1p_{3/2}$ orbitals for the 2_1^+ and 2_2^+ states. The occupancies of the neutron $1p_{3/2}$ orbital for 0^+ and 2^+ levels up to 4.5 MeV in excitation energy for ^{38,40,42,44}S from SDPF-MU calculations are provided in Figure 1.8. An increase in neutron $1p_{3/2}$ occupancy is strongly correlated with a decrease in occupancy for the neutron $0f_{7/2}$ orbital. As seen in Figure 1.8, the neutron $1p_{3/2}$ occupancies of the 2_1^+ and 2_2^+ states differ the most for ^{42}S. The $1p_{3/2}$ and $0f_{7/2}$ orbitals cannot be connected by the magnetic dipole operator, leading to a strongly hindered $B(M1; 2_2^+ \rightarrow 2_1^+)$ transition strength in ^{42}S of 0.14×10^{-3} μ_N^2 compared to 0.19 μ_N^2 in ^{40}S and 0.48 μ_N^2 in ^{38}S. As a

result, the $2_2^+ \rightarrow 0_1^+$ branch is favored in ^{42}S. The dramatic increase in level density for 0^+ and 2^+ states below 4.5 MeV in ^{44}S signals the sudden and massive gain in correlation energy of the intruder configuration formed by moving two neutrons into the $1p_{3/2}$ orbital compared to the closed $0f_{7/2}$ shell configuration, placing ^{44}S inside of the $N = 28$ island of inversion with ^{42}S right at the boundary. Due to this particular interplay of the single-particle configurations, a measurement of the $B(E2)$ excitation strengths to higher-lying 2^+ states provides a unique window into the breakdown of the $N = 28$ shell gap at $Z = 16$ and the underlying driving forces that are a cornerstone in explaining shell evolution in rare isotopes.

As discussed above, one of the characteristics of the $N = 28$ island of inversion is the coexistance of multiple shapes at low excitation energy. Studies of ^{44}S have indicated that the ground state is prolate deformed while the second 0^+ state is spherical [42, 49]. One neutron below ^{44}S, the discovery of a long-lived (isomeric) $7/2^-$ state at 320 keV provided evidence for shape coexistence in ^{43}S [41]. The half-life ($T_{1/2} = \ln(2) \cdot \tau$) of the isomer has been reported as 415 ns [50, 51] and the structure of the isomeric state has been interpreted as a spherical $0f_{7/2}$ single-neutron hole state while the intruder $3/2^-$ ground state is prolate deformed [50]. The spins and parities of other excited states have not been firmly established [15, 52, 53], as will be discussed in later chapters. Furthermore, recent work has indicated that proton-neutron correlations prevent the isomeric state from being regarded as purely spherical and noted that it would be of great interest to experimentally identify the levels belonging to the ground-state rotational band in order to give unambiguous evidence of shape coexistence in ^{43}S [51].

In this work, intermediate-energy Coulomb excitation is used to populate higher-lying 2^+ states in the even-even S isotopes and to search for collective structures built on the ^{43}S

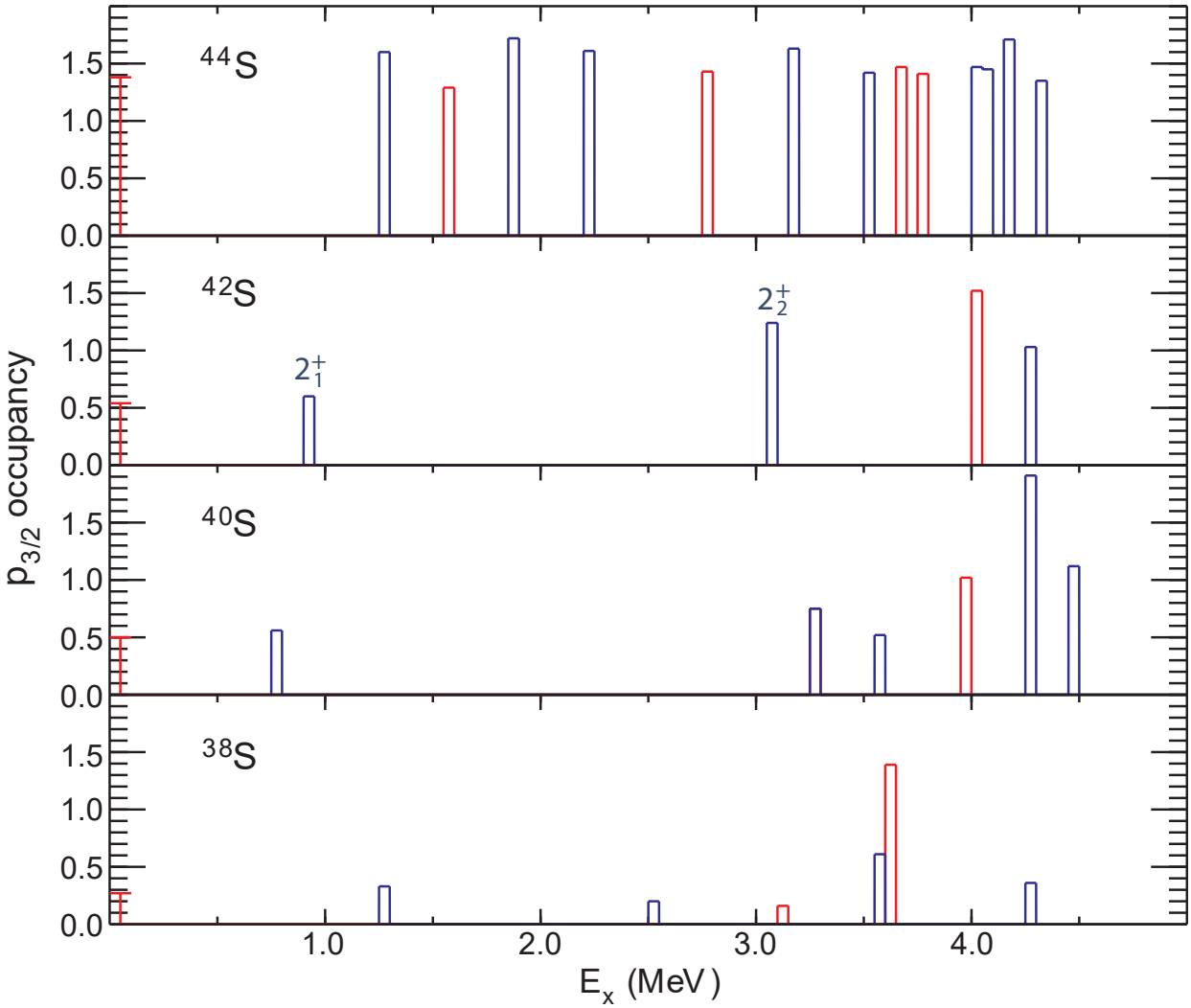

Figure 1.8: SDPF-MU neutron $1p_{3/2}$ occupancies for 0^+ (red) and 2^+ states (blue) below 4.5 MeV in ^{38,40,42,44}S. The increase in occupancy for the second 2^+ state in ^{42}S relative to ^{38}S explains the observed change in γ-decay pattern. Figure modified from [10].

ground and isomeric states. Measurements of the experimental $B(E2)$ strengths from the 0^+ ground state to higher-lying 2^+ states allow the onset of intruder configurations in the S isotopic chain to be characterized. Shell-model calculations using the SDPF-MU interaction, which predict a fragmentation of the strength over many different 2^+ states in ^{44}S are shown in Figure 1.9. Testing the predictions of the most successful effective Hamiltonian in this region is an important step toward confirming the underlying mechanism of shell evolution.

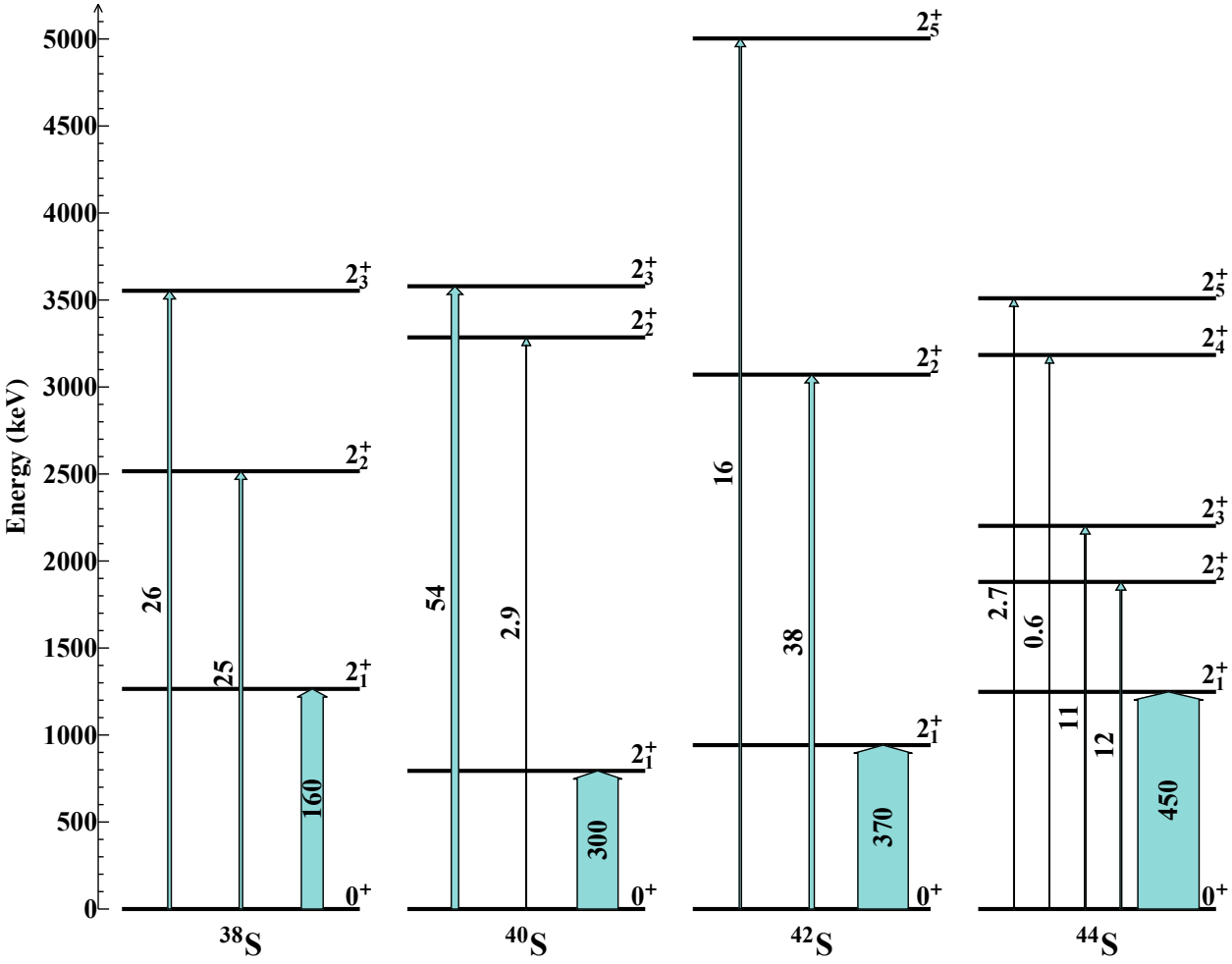

Figure 1.9: SDPF-MU predictions for $B(E2; 0_1^+ \rightarrow 2^+)$ strengths in e^2fm^4 for levels in ^{38,40,42,44}S. Arrow widths are proportional to transition strength. 2^+ states above 4 MeV with $B(E2)$ values less than 10 e^2fm^4 are omitted in this figure. Effective proton and neutron charges of 1.35 and 0.35, respectively, were used in the SDPF-MU calculations.

Chapter 2

Intermediate-Energy Coulomb Excitation

Coulomb excitation is the inelastic excitation of a projectile (target) nucleus due to electromagnetic interaction with a target (projectile) nucleus and is a well-established experimental probe in nuclear science [54–59]. With the high-intensity, low-velocity stable beams used in the early days of this method, experiments were performed at energies below the Coulomb barrier in order to ensure physical separation of the target and projectile, thus avoiding nuclear contributions to the excitation mechanism [54, 55]. More recently, the in-flight production of fast beams of radioactive nuclei has made it possible to study the structure of nuclei far from the valley of stability, prompting the development of intermediate-energy Coulomb excitation as an experimental tool [56, 57, 60, 61].

In intermediate-energy Coulomb excitation experiments, exotic nuclei at energies in excess of 30 MeV per nucleon are scattered off stable high-Z targets. The scattered nuclei are detected in coincidence with the de-excitation γ rays and the Coulomb excitation cross section is calculated from the efficiency-corrected number of detected γ rays. At these beam energies, the analysis should be restricted to a maximum scattering angle, or equivalently a minimum impact parameter, which is chosen to exceed the sum of the radii of the target and projectile nuclei by several fm [57, 62]. The impact parameter b and center-of-mass

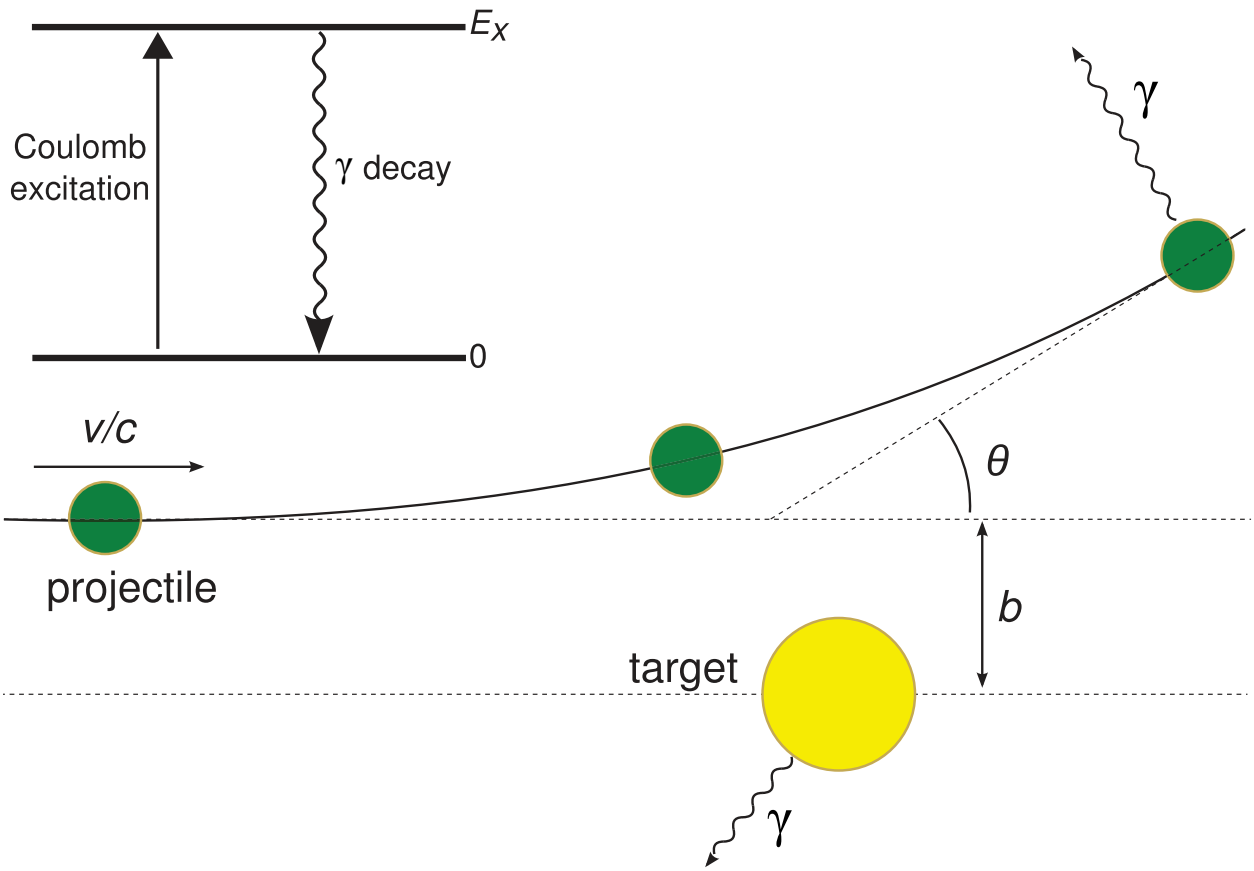

Figure 2.1: Schematic of intermediate-energy Coulomb excitation. The projectile (target) nucleus is inelastically excited in the Coulomb field of the target (projectile) nucleus. In analysis, a maximum center-of-mass scattering angle θ (minimum impact parameter b) is considered to ensure no nuclear contribution to the cross section. Figure adapted from [11].

scattering angle θ are related by:

$$b = \frac{a_0}{\gamma} \cot\left(\frac{\theta}{2}\right), \tag{2.1}$$

where the Lorentz factor $\gamma = 1/\sqrt{1-(v/c)^2}$ and a_0 is the half-distance of closest approach:

$$a_0 = \frac{Z_t Z_p e^2}{m_0 v^2}, \tag{2.2}$$

which depends on the proton numbers of the target and projectile, Z_t and Z_p, the reduced

mass m_0 of the system, and the velocity v of the projectile. The scattering angle restriction ensures that the Coulomb interaction dominates over nuclear and nuclear-Coulomb interference contributions to the excitation. A schematic illustrating intermediate-energy Coulomb excitation is provided in Figure 2.1. From the angle-integrated cross section, the reduced transition probability $B(\sigma\lambda; i \rightarrow f)$ from the initial state i of the projectile to the populated excited state f can be calculated, for example, using the semi-classical theory of relativistic Coulomb excitation developed by Alder and Winther [61].

2.1 Alder-Winther Formalism

In the Alder-Winther formalism [61], the relative motion of the projectile and the target is described using the classical Rutherford trajectory while the single-step electromagnetic excitation of the projectile is treated quantum mechanically using perturbation theory. Since this theoretical framework assumes there is no overlap between the charge distributions of the target and projectile, the excitation is pure Coulomb and the cross section can be expressed in terms of the same electromagnetic multipole matrix elements as those in the expression for the electromagnetic decay of nuclear states.

Assuming the relative motion takes place on the classical Rutherford trajectory, the differential cross section for exciting the projectile from its initial nuclear state i to final state f can be written as the Rutherford differential cross section multiplied by the probability of excitation:

$$\left(\frac{d\sigma}{d\Omega}\right)_{i\rightarrow f} = \left(\frac{d\sigma}{d\Omega}\right)_{\text{Rutherford}} P_{i\rightarrow f}. \tag{2.3}$$

The Coulomb excitation probability can be calculated using first-order time-dependent per-

turbation theory:

$$P_{i\to f} = \left|a_{i\to f}\right|^2, \tag{2.4}$$

where

$$a_{i\to f} = \frac{1}{i\hbar}\int_{-\infty}^{\infty} e^{i\omega_{fi}t}\langle f\left|V(\mathbf{r}(t))\right|i\rangle dt. \tag{2.5}$$

Here, $\omega_{fi} = (E_f - E_i)/\hbar = \Delta E/\hbar$ and $V(\mathbf{r}(t))$ is the Coulomb potential which depends on the relative positions of the projectile and target nucleus.

The transition amplitude $a_{i\to f}$ can be expanded in terms of electric and magnetic multipole matrix elements and written as a product of two factors:

$$a_{i\to f} = i\sum_{\lambda}\chi^{(\lambda)}_{i\to f} f_\lambda(\xi), \tag{2.6}$$

with $\chi^{(\lambda)}_{i\to f}$ being a measure of the strength of the interaction:

$$\chi^{(\lambda)}_{i\to f} \approx \frac{Z_t e}{\hbar c b^\lambda}\langle f\left|\mathcal{O}(\sigma\lambda)_\mu\right|i\rangle, \tag{2.7}$$

The function $f_\lambda(\xi)$ incorporates the dependence of the amplitude on the adiabaticity of the reaction. The adiabatic parameter ξ is the ratio of the amount of time the projectile spends in the vicinity of the target nucleus (called the collision time $\tau_{\rm coll}$) to the timescale of internal motion in the nucleus being excited $\tau_{\rm nuc}$. The collision time is expressed as:

$$\tau_{\rm coll} = \frac{b}{\gamma v}, \tag{2.8}$$

while the internal motion timescale is:

$$\tau_{\text{nuc}} = \frac{1}{\omega_{fi}} = \frac{\hbar}{\Delta E}. \tag{2.9}$$

Therefore, the adiabaticity parameter can be written as:

$$\xi = \frac{\tau_{\text{coll}}}{\tau_{\text{nuc}}} = \frac{\Delta E}{\hbar \gamma v} b. \tag{2.10}$$

For large values of ξ, corresponding to low projectile velocity, large impact parameter, or high excitation energy, the reaction is referred to as adiabatic. In these cases, the projectile is unlikely to be excited. Consequently, $f_\lambda(\xi)$ decreases exponentially as a function of ξ. Conversely, for violent reactions with ξ nearing 0, excitation is likely to occur and $f_\lambda(\xi)$ approaches 1.

At relativistic velocities, the violent reactions that have nuclear contributions are avoided by considering small scattering angles (large impact parameters). Furthermore, excitations are predominantly single-step due to the limited amount of time the projectile is in the vicinity of the Coulomb field of the target nucleus. Therefore, Winther and Alder have made the approximation that the projectile travels on a straight-line trajectory in the equations above. In order to account for the distortion of the trajectory due to the Coulomb interaction in first order, the impact parameter is rescaled by:

$$b \to b + \frac{\pi}{2} \frac{a_0}{\gamma}, \tag{2.11}$$

correcting the adiabaticity parameter to:

$$\xi = \frac{\Delta E}{\hbar\gamma v}\left(b + \frac{\pi}{2}\frac{a_0}{\gamma}\right) = \frac{\Delta E}{\hbar\gamma v} b_a. \tag{2.12}$$

Neglecting $f_\lambda(\xi)$ for simplicity, the Coulomb excitation cross section can be approximated by integrating $\left|\chi^{(\lambda)}_{i\to f}\right|^2$ over impact parameters from $b_{\min}$ to $b_{\max}$. The lower limit is the experimentally-chosen minimum impact parameter and the upper limit is the impact parameter corresponding to ξ=1:

$$b_{\max} = b_a = \frac{\hbar\gamma v}{\Delta E}. \tag{2.13}$$

Note that this also sets the maximum excitation energy to be $\Delta E = \hbar\gamma v / b_{\max}$. The cross section is then:

$$\sigma_\lambda = 2\pi \int_{b_{\min}}^{b_{\max}} b db P_{i\to f} \approx 2\pi \int_{b_{\min}}^{b_{\max}} b db \left|\chi^{(\lambda)}_{i\to f}\right|^2. \tag{2.14}$$

Evaluating this expression results in the Coulomb excitation cross section in terms of the reduced transition probability:

$$\sigma_{\sigma\lambda} \approx \left(\frac{Z_t e^2}{\hbar c}\right)^2 \frac{\pi}{e^2 b_{\min}^{2\lambda-2}} B(\sigma\lambda; 0\to\lambda) \begin{cases} (\lambda-1)^{-1} & \text{for } \lambda \geq 2 \\ 2\ln(b_{\max}/b_{\min}) & \text{for } \lambda = 1, \end{cases} \tag{2.15}$$

and the total cross section is the sum over all allowed electric and magnetic multipolarities:

$$\sigma_{i\to f} = \sum_{\sigma\lambda} \sigma_{\sigma\lambda}. \tag{2.16}$$

Here, σ is electric E or magnetic M in the sum and subscript. As seen in Equation 2.15,

the Coulomb cross section is directly proportional to the reduced transition strength $B(\sigma\lambda)$. For the $0_1^+ \rightarrow 2^+$ excitations of interest in this work, the multipolarity is pure $E2$ and the cross section is proportional to $B(E2; 0_1^+ \rightarrow 2^+)$ strength.

The exact expression for the Coulomb excitation cross section is derived in detail by Winther and Alder in [61]. Their result for the excitation amplitude is:

$$a_{i\rightarrow f} = -i\frac{Z_t e^2}{\hbar\gamma v}\sum_{\sigma\lambda\mu} G_{\sigma\lambda\mu}\left(\frac{c}{v}\right)(-1)^{\mu} K_{\mu}\left(\xi(b)\right)\left(\frac{\Delta E}{\hbar c}\right)^{\lambda}\sqrt{2\lambda+1} \times \frac{\langle J_f M_f \left|\mathcal{O}(\sigma\lambda)_{-\mu}\right| J_i M_i\rangle}{e}, \quad (2.17)$$

where K_μ are the modified Bessel functions of the second kind. For electric transitions, the function $G_{E\lambda\mu}$ is defined for $\mu \geq 0$ as:

$$G_{E\lambda\mu}\left(\frac{c}{v}\right) = i^{\lambda+\mu}\frac{\sqrt{16\pi}}{\lambda(2\lambda+1)!!}\left(\frac{(\lambda-\mu)!}{(\lambda+\mu)!}\right)^{1/2}\left(\left(\frac{c}{v}\right)^2 - 1\right)^{-1/2} \times \left(\frac{(\lambda+1)(\lambda+\mu)}{2\lambda+1}P^{\mu}_{\lambda-1}\left(\frac{c}{v}\right) - \frac{\lambda(\lambda-\mu+1)}{2\lambda+1}P^{\mu}_{\lambda+1}\left(\frac{c}{v}\right)\right), \quad (2.18)$$

and for magnetic transitions, the function $G_{M\lambda\mu}$ is defined for $\mu \geq 0$ as:

$$G_{M\lambda\mu}\left(\frac{c}{v}\right) = i^{\lambda+\mu+1}\frac{\sqrt{16\pi}}{\lambda(2\lambda+1)!!}\left(\frac{(\lambda-\mu)!}{(\lambda+\mu)!}\right)^{1/2}\left(\left(\frac{c}{v}\right)^2 - 1\right)^{-1/2}\mu P^{\mu}_{\lambda}\left(\frac{c}{v}\right). \quad (2.19)$$

In these expressions, P^{μ}_{λ} are the associated Legendre polynomials. Note that for negative μ there are the relations:

$$G_{E\lambda-\mu}\left(\frac{c}{v}\right) = (-1)^{\mu} G_{E\lambda\mu}\left(\frac{c}{v}\right), \quad (2.20)$$

$$G_{M\lambda-\mu}\left(\frac{c}{v}\right) = (-1)^{\mu+1} G_{M\lambda\mu}\left(\frac{c}{v}\right). \quad (2.21)$$

The full Coulomb excitation cross section is then:

$$\sigma_{i\to f} = 2\pi \int_{b_{\min}}^{\infty} bdb \frac{1}{2J_i+1} \sum_{M_i M_f} \left|a_{i\to f}\right|^2 \tag{2.22}$$

$$= \left(\frac{Z_t e^2}{\hbar c}\right)^2 \sum_{\sigma\lambda\mu} \left(\frac{\Delta E}{\hbar c}\right)^{2(\lambda-1)} \frac{B(\sigma\lambda; J_i \to J_f)}{e^2} \left|G_{\sigma\lambda\mu}\left(\frac{c}{v}\right)\right|^2 g_\mu\left(\xi(b_{\min})\right), \tag{2.23}$$

where the function $g_\mu\left(\xi(b_{\min})\right)$ is:

$$g_\mu\left(\xi(b_{\min})\right) = 2\pi \left(\frac{\Delta E}{\hbar\gamma v}\right)^2 \int_{b_{\min}}^{\infty} bdb \left|K_\mu\left(\xi(b)\right)\right|^2 \tag{2.24}$$

$$= 2\pi \int_{\xi}^{\infty} \left|K_\mu\left(x\right)\right|^2 xdx. \tag{2.25}$$

This integral can be evaluated in terms of the modified Bessel functions of the second kind. For $\mu \geq 0$:

$$g_\mu(\xi) = g_{-\mu}(\xi) = \pi\xi^2 \left[\left|K_{\mu+1}\left(\xi\right)\right|^2 - \left|K_\mu\left(\xi\right)\right|^2 - \frac{2\mu}{\xi} K_{\mu+1}\left(\xi\right) K_\mu\left(\xi\right)\right]. \tag{2.26}$$

The full result of Equation 2.23 also shows a direct proportionality between the Coulomb excitation cross section and the reduced transition strength. A Mathematica script has been developed to perform the full Alder-Winther calculations and is used in this work to determine reduced transition strengths given the experimentally-measured Coulomb excitation cross sections. The basis of the Mathematica script is provided in [63].

2.2 Experimental Considerations

As seen in Equation 2.23, the Coulomb excitation cross section is proportional to Z_t^2. In this work, the heaviest stable nuclide ^{209}Bi ($Z = 83$) is utilized for the target material in order to maximize Z_t. ^{209}Bi is one proton above doubly-magic ^{208}Pb and the adopted $B(E2; 9/2^- \rightarrow 7/2^-)$ strength between the ground state and first excited state at 896.28(5) keV is only 26.1(16) $e^2\text{fm}^4$ [7]. Consequently, the Coulomb excitation of target nuclei due to the S ($Z = 16$) projectiles is hindered and γ rays from the target do not significantly contribute to the observed γ-ray spectra. The general expression for the experimental cross section is:

$$\sigma_{i\rightarrow f} = \frac{N_{\gamma, f\rightarrow g}}{N_{\text{beam}} n_{\text{target}}}. \tag{2.27}$$

Here, $N_{\gamma,f\rightarrow g}$ is the efficiency-corrected number of γ-ray transitions from the populated state to all levels g it γ decays to, N_{beam} is the number of incoming beam particles, and n_{target} is the areal number density of the target (number of target nuclei per unit area). Cross sections in nuclear physics are often given in units of millibarns (1 mb = 10^{-31} m^2 = 0.1 fm^2).

In the Coulomb excitation process, the magnetic substates μ are not populated equally [64]. Therefore, the de-excitation γ rays are not emitted isotropically in the center-of-mass frame. The γ-ray angular distribution can be parameterized in terms of Legendre polynomials P_k:

$$W(\phi) = \sum_{k \text{ even}} a_k P_k(\cos\phi), \tag{2.28}$$

where ϕ is the center-of-mass angle of the γ ray with respect to the beam axis. The index k runs from 0 to the smaller of 2λ or $2J_i$. The angle measured in the center-of-mass frame ϕ

is related to the laboratory-frame angle $\phi_{\rm lab}$ by:

$$\cos\phi = \frac{\cos\phi_{\rm lab} - \beta}{1 - \beta\cos\phi_{\rm lab}}. \tag{2.29}$$

The coefficients a_k found using the Alder-Winther excitation amplitudes are [63]:

$$a_k = \sum_{\mu LL'} \left| G_{\lambda\mu}\left(\frac{c}{v}\right)\right|^2 g_\mu(\xi)(-1)^\mu \begin{pmatrix} \lambda & \lambda & k \\ \mu & -\mu & 0 \end{pmatrix} \times \begin{Bmatrix} J_f & J_f & k \\ \lambda & \lambda & J_i \end{Bmatrix} F_k(L, L', J_{ff}, J_f)\sqrt{2k+1}\delta_L\delta_{L'}, \tag{2.30}$$

where J_{ff} is the spin of the state the γ decay populates and the γ-γ correlation function $F_k(L, L', J_f, J_i)$ is:

$$F_k(L, L', J_f, J_i) = (-1)^{J_f+J_i-1}\sqrt{(2k+1)(2J_i+1)(2L+1)(2L'+1)} \times \begin{pmatrix} L & L' & k \\ 1 & -1 & 0 \end{pmatrix} \begin{Bmatrix} L & L' & k \\ J_f & J_i & J_f \end{Bmatrix}. \tag{2.31}$$

The effect of the γ-ray angular distribution on the detection efficiency must be taken into account when determining the efficiency-corrected number of γ decays if the γ-ray detection array does not cover the full 4π solid angle.

The uncertainties associated with the approximations used in the semi-classical method of Winther and Alder have been studied through fully quantal coupled-channels calculations. Due to nuclear effects, mult-step excitations, and unobserved feeding, the theoretical uncertainty for the semi-classical model is approximately 13% compared to a theoretical

uncertainty of less than 7% for the coupled-channels analysis [65]. The results obtained for reduced transition strengths from intermediate-energy Coulomb excitation experiments have shown excellent agreement with the results found using other experimental probes [66].

2.3 Reduced Transition Probabilities and Lifetimes

The lifetime τ of a nuclear state is the inverse of the transition rate W introduced in Section 1.4:

$$\frac{1}{\tau} = W = \sum_{\sigma\lambda} \left(\frac{8\pi(\lambda+1)}{\lambda[(2\lambda+1)!!]^2} \right) \frac{1}{\hbar} \left(\frac{E_\gamma}{\hbar c} \right)^{2\lambda+1} B(\sigma\lambda; J_i \rightarrow J_f). \tag{2.32}$$

Therefore, lifetime measurements can be performed to extract $B(\sigma\lambda)$ strengths for γ decay, which are related to the $B(\sigma\lambda)$ strengths for Coulomb excitation by Equation 1.18. Plugging in the values, the $B(\sigma\lambda)$ strengths for γ decay are related to the partial lifetimes ($\tau_p = \tau/b$ where b is the branching fraction) by [5]:

$$B(E1) = \frac{0.629}{E_\gamma^3 \tau_p}\ e^2\mathrm{fm}^2\mathrm{MeV}^3\mathrm{fs}, \tag{2.33}$$

$$B(E2) = \frac{816}{E_\gamma^5 \tau_p}\ e^2\mathrm{fm}^4\mathrm{MeV}^5\mathrm{ps}, \tag{2.34}$$

$$B(E3) = \frac{1760}{E_\gamma^7 \tau_p}\ e^2\mathrm{fm}^6\mathrm{MeV}^7\mu\mathrm{s}, \tag{2.35}$$

$$B(M1) = \frac{56.8}{E_\gamma^3 \tau_p}\ \mu_N^2\mathrm{MeV}^3\mathrm{fs}, \tag{2.36}$$

$$B(M2) = \frac{74.1}{E_\gamma^5 \tau_p}\ \mu_N^2\mathrm{fm}^2\mathrm{MeV}^5\mathrm{ns}, \tag{2.37}$$

$$B(M3) = \frac{0.1585}{E_\gamma^7 \tau_p}\ \mu_N^2\mathrm{fm}^4\mathrm{MeV}^7\mathrm{s}. \tag{2.38}$$

Chapter 3

Experimental Method

The neutron-rich isotopes ^{38,40,42,43,44}S were studied using intermediate-energy Coulomb excitation at the National Superconducting Cyclotron Laboratory (NSCL) [67] at Michigan State University. In this experiment, each sulfur isotope was studied at a different time over the period of a week. Roughly 12 hours of data were taken for ^{38,40}S and about 24 hours of data were taken for ^{42,43,44}S. The five separate beams of radioactive ^{38,40,42,43,44}S were all produced by the Coupled Cyclotron Facility using the projectile fragmentation method [68] and transported to the experimental hall where they were impinged on a 492 mg/cm^2 ^{209}Bi target to electromagnetically excite the levels of interest. The de-excitation γ rays were detected using the CsI(Na) scintillator array CAESAR [14] and the outgoing beam particles and reaction products were identified on an event-by-event basis with the S800 magnetic spectrograph [69]. The following sections describe these experimental systems in detail.

3.1 Beam Production and Purification

A schematic of the NSCL Coupled Cyclotron Facility is provided in Figure 3.1. In order to produce the radioactive sulfur isotopes of interest in this work, a stable primary beam of ^{48}Ca was first developed. A solid block of metallic ^{48}Ca was heated in an oven until vaporization. Once in gaseous form, the ^{48}Ca atoms were ionized via the electron cyclotron resonance (ECR) technique in the Advanced Room TEMperature Ion Source (ARTEMIS)

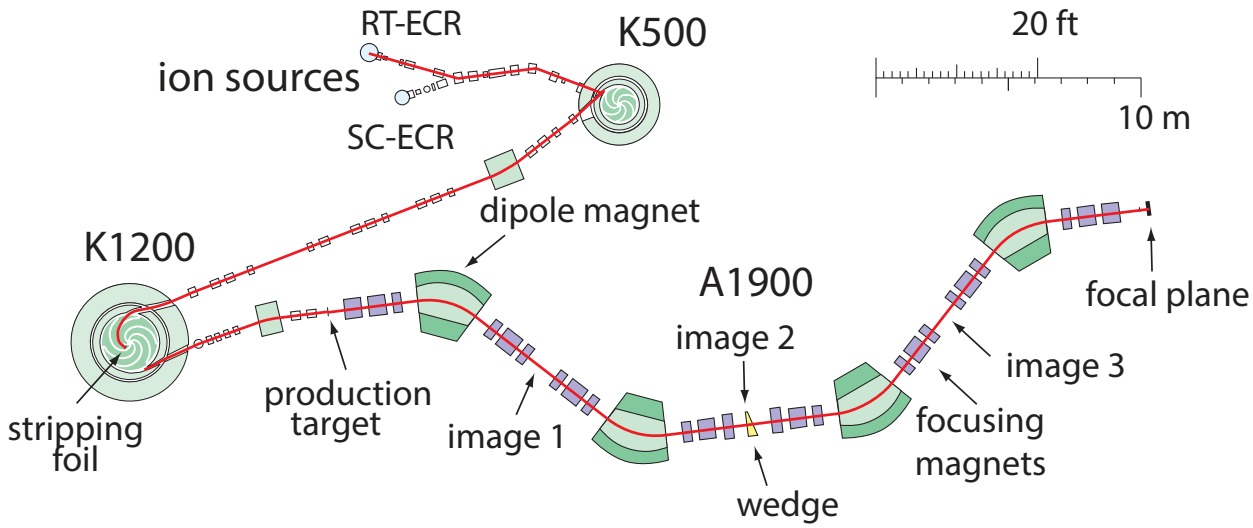

Figure 3.1: Layout of the Coupled Cyclotron Facility at the National Superconducting Cyclotron Laboratory showing the ion sources, K500 and K1200 cyclotrons, and A1900 fragment separator [12]. Figure adapted from [13].

[70]. In Figure 3.1, ARTEMIS is represented by RT-ECR standing for room temperature ECR. In the ECR method, the gas is injected into the ion source and confined in a magnetic trap. Electrons are accelerated using microwave radiation tuned to the resonant frequency ω of the cavity:

$$\omega = \frac{eB}{m_e}, \tag{3.1}$$

where e and m_e are the charge and mass of an electron and B is the strength of the magnetic field. The accelerated electrons ionize the gas atoms by stripping electrons during collisions. In this experiment, ^{48}Ca was ionized in ARTEMIS to a charge state of 8+ meaning that eight electrons were removed from the neutral atom.

Next, the $^{48}Ca^{8+}$ ions were injected into the K500 cyclotron. According to the Lorentz law, particles with charge q and momentum p perpendicular to a magnetic field B will follow a radius of curvature ρ given by:

$$\rho = \frac{p}{qB} = \frac{\gamma m v}{qB}, \tag{3.2}$$

where m and v are the mass and velocity of the particle and γ is the relativistic factor. The quantity $B\rho$ is referred to as the magnetic rigidity:

$$B\rho = \frac{p}{q} = \frac{\gamma m v}{q}. \tag{3.3}$$

The K500 and K1200 cyclotrons at the NSCL operate using this principle. The cyclotrons consist of three "dees", copper electrodes surrounded by a superconducting electromagnet, which produce a radio-frequency (RF) electric field that accelerates the ions in the gaps between the dees. The trajectories of the ions are confined by the applied magnetic field from the superconducting electromagnets. As the energy of the ions increases, the radius of curvature gets larger. Once the ions reach the maximum energy given the radius constraints of the cyclotron, they are extracted at a port on the outer edge. For the $^{48}Ca^{8+}$ ions in this experiment, the primary beam energy was accelerated to 12.28 MeV per nucleon (12.28 MeV/u) after the K500 cyclotron.

After extraction from the K500 cyclotron, the ions are transported and injected into the K1200 cyclotron. A carbon stripper foil is located at the center of the K1200 cyclotron to increase the charge state of the ions in order to increase the maximum possible final energy. In this work, the ^{48}Ca ions were fully stripped ($^{48}Ca^{20+}$) and accelerated to 140 MeV/u.

The ^{48}Ca primary beam was then impinged on a thick ^{9}Be production target, producing a cocktail secondary beam of different fully-stripped ions, including the rare neutron-rich sulfur isotopes, through projectile fragmentation. To purify the secondary beam, the A1900 fragment separator [12] was utilized. The A1900 consists of four large 45° dipole bending magnets and 24 quadrupole focusing magnets with additional magnets for higher-order corrections and achieves isotopic separation using the $B\rho$-ΔE-$B\rho$ technique [12]. In the initial

$B\rho$ stage, the secondary beam is purified by tuning the magnetic fields of the first two dipoles. From Equation 3.3, the chosen magnetic rigidity selects the momentum-to-charge ratio p/q of the ions that will pass through the fixed-radius dipoles. However, particles with similar p/q ratios to the projectiles of interest will also make it through this selection process. In order to limit these contaminants, slits at the image points and focal plane of the A1900 (see Figure 3.1) can be employed to only allow a certain range of momenta. However, particles with the same p/q ratio cannot be unambiguously selected with $B\rho$ alone. Therefore, in the ΔE step, the beam is impinged on an achromatic aluminum wedge degrader (actually a curved aluminum foil) located at the mid-acceptance position of the A1900. The differential energy loss of the ions traversing the wedge per differential path length is described by the Bethe formula [71]:

$$-\frac{dE}{dx} = \frac{4\pi e^4 n_e Z^2}{m_e (v/c)^2}\left[\ln\left(\frac{2m_e\gamma^2(v/c)^2}{I}\right) - (v/c)^2\right], \tag{3.4}$$

where e is the electron charge, n_e is the electron number density of the degrader, Z is the atomic number of the incoming ion, m_e is the electron mass, v/c is the ion velocity relative to the speed of light, γ is the relativistic factor, and I is the mean excitation potential of the degrader. From this equation, the energy loss is proportional to the square of the charge of the ion. Consequently, particles starting with the same momentum but with different atomic numbers Z will have different momenta after passing through the wedge. A 450 mg/cm^2 Al wedge was used for all settings in this experiment. The final step in the purification process is another $B\rho$ selection using the magnetic rigidities of the final two dipole magnets. In this experiment, the slits were adjusted to give a momentum acceptance dp/p of about 1% for ^{38,40,42,43}S and 2% for ^{44}S. The production targets used for each secondary beam

are provided in Table 3.1 along with the energies of the projectiles before the ^{209}Bi reaction target calculated using the program LISE++ [72].

Table 3.1: Production target, momentum acceptance dp/p, and energy as inferred from the magnetic rigidity setting of the segment of the analysis line just before the 492 mg/cm^2 ^{209}Bi reaction target in front of the S800 spectrograph for each secondary beam setting.

Setting	^{9}Be Production Target (mg/cm^2)	dp/p	Energy (MeV/u)
^{38}S	1034	1.07%	81.85
^{40}S	987	1.07%	82.18
^{42}S	940	1.08%	86.48
^{43}S	1034	1.07%	83.03
^{44}S	1081	2.02%	79.40

3.2 S800 Magnetic Spectrograph

After separation in the A1900, the secondary beam passed through a thin plastic scintillator at the extended focal plane of the A1900 (XFP scintillator) and was delivered through the transfer hall to the analysis beam line where it was impinged on the ^{209}Bi reaction target at the target position of the high-resolution, high-acceptance, S800 magnetic spectrograph [69]. In this experiment, the analysis line, which consists of four dipoles, five sets of quadrupole triplets, one quadrupole doublet, and four sextupole magnets [73], was operated in focus mode, where the focal point for the beam is at the ^{209}Bi reaction target and the beam is dispersed at the S800 focal plane. Following the reaction target, there is a quadrupole magnet that refocuses the beam and two large dipole magnets that bend the charged particles based on their momentum-to-charge ratios. The magnetic rigidity of the dipoles is set to center the reaction products of interest in the focal plane of the S800. The analysis line and S800 magnetic spectrograph are shown in Figure 3.2.

There are a number of detectors at the focal plane of the S800 that are used for particle

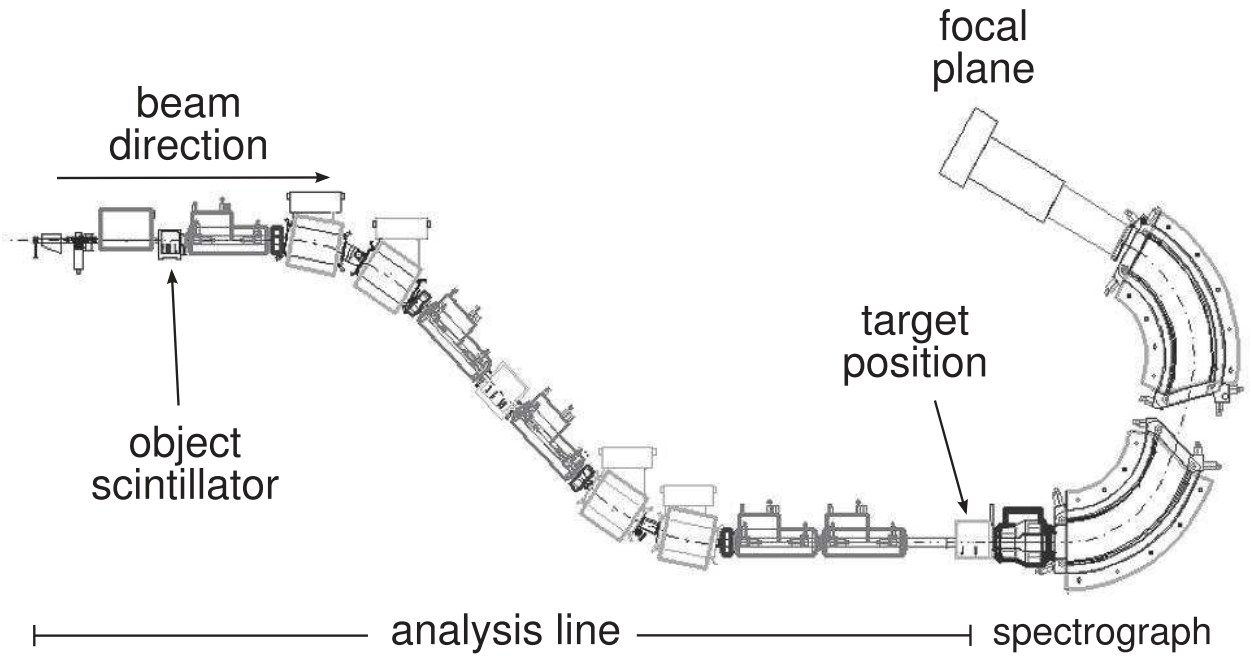

Figure 3.2: Illustration of the S800 magnetic spectrograph including the analysis line. The target position was surrounded by the CsI(Na) array CAESAR. Figure taken from [11].

identification and trajectory reconstruction [74]. A diagram of the S800 focal plane is shown in Figure 3.3. The reaction products first pass through two cathode readout drift chambers (CRDCs). The upstream (CRDC1) and downstream (CRDC2) CRDCs are spaced one meter apart and are used to determine the xy-positions and angles necessary for the reconstruction of the trajectory for each ion. Next, the energy loss of the ions is measured in an ionization chamber to determine the atomic number of the ion. Afterward, the ions traverse a thin plastic scintillator (E1 scintillator) that is used for timing measurements and to trigger the data acquisition system. As described in detail in the sections below, timing measurements and the S800 focal plane detectors allow the incoming beam particles and the reaction products to be identified event-by-event.

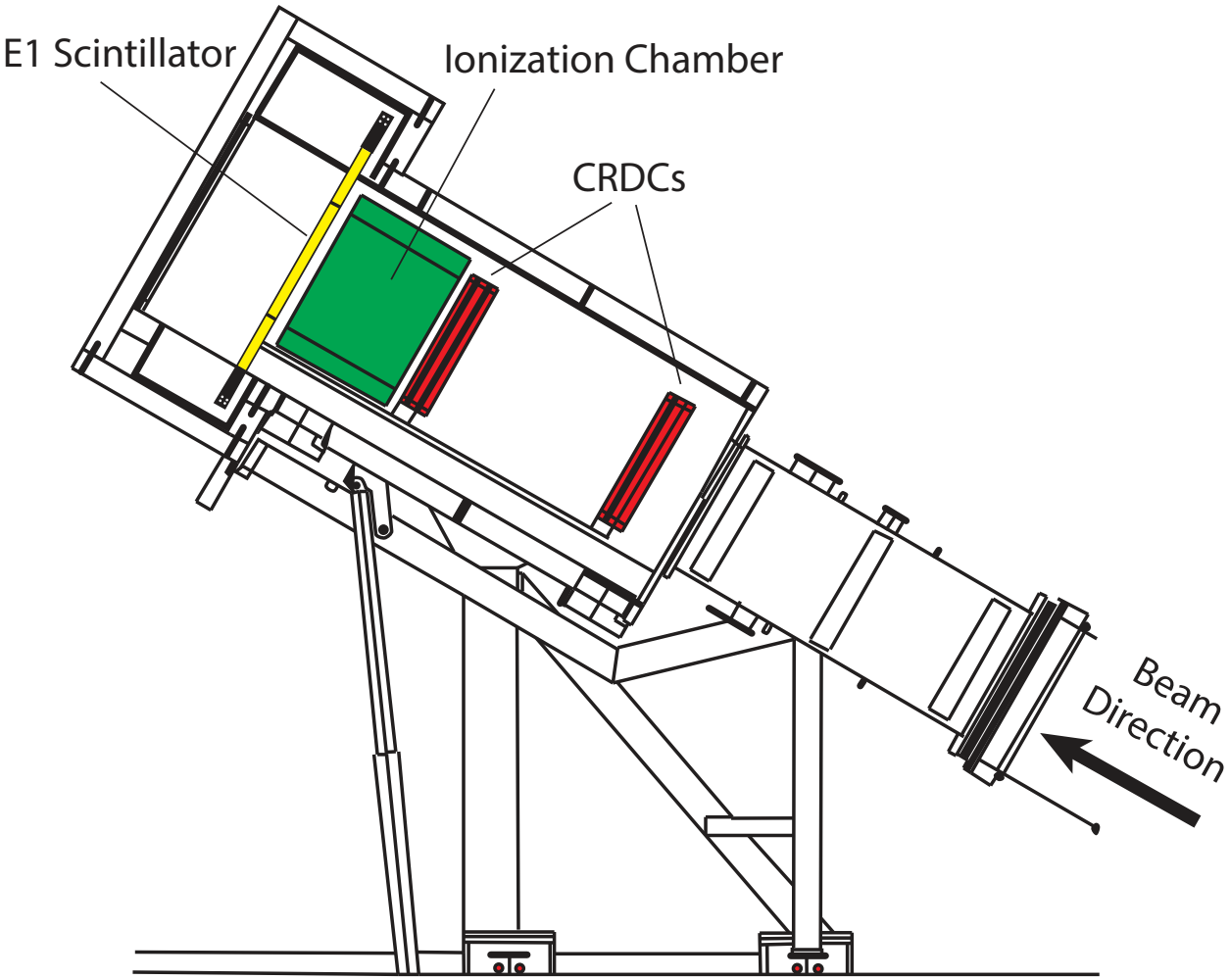

Figure 3.3: S800 focal plane diagram showing the cathode readout drift chambers (CRDCs), ionization chamber, and E1 plastic scintillator. Figure modified from [13].

3.2.1 Particle Identification and Trajectory Reconstruction

Near the beginning of the analysis line, there is another thin plastic scintillator at the object position of the S800 (OBJ scintillator). The XFP and OBJ scintillators are used in conjunction with the E1 plastic scintillator at the S800 focal plane to perform time-of-flight measurements. The scintillators are coupled to photomultiplier tubes that detect the fluorescence light generated when ions pass through the plastic. The incoming secondary beam ions have been selected by $B\rho = \gamma mv/q$. Therefore, assuming a fixed flight path through

the analysis line and S800, the time of flight, which is inversely proportional to velocity, is proportional to the mass-to-charge ratio. Since the ions are fully stripped, selecting on the ratio m/q is equivalent to selecting on A/Z. Consequently, the time-of-flight difference XFP-OBJ (both relative to E1) is sensitive to the A/Z of the incoming beam components. Since the proportionality to A/Z depends on the assumption that the flight path is fixed, correcting for the correlations between time of flight (for XFP-E1 and OBJ-E1) and the dispersive angle and position in the S800 focal plane provides significant improvement in timing resolution.

To unambiguously identify the reaction products, the time-of-flight difference between the OBJ and E1 scintillators is used in conjunction with the energy loss in the ionization chamber. The ionization chamber consists of 16 individual parallel plate chambers and is filled with P10 gas (90% Ar and 10% methane). When the reaction products travel through the ionization chamber, the P10 gas is ionized and the electrons drift toward the anode providing a signal proportional to the energy deposition. The energy loss in the ionization chamber is proportional to Z^2 as seen in Equation 3.4. As discussed above, the time-of-flight difference is proportional to A/Z. Therefore, reaction products are uniquely identified by plotting the energy deposited in the ionization chamber against the time of flight through the S800 spectrograph (so-called ΔE-ToF technique).

In intermediate-energy Coulomb excitation, analysis must be restricted to small scattering angles to limit nuclear contributions to the cross section (see Chapter 2). The position information from the CRDCs in the S800 focal plane is used to track the trajectory of the scattered particles back to the reaction target. As a result, the scattering angle for each particle on an event-by-event basis can be determined.

Each CRDC has an active depth of 1.5 cm and an active area of about 60 cm in the

x (dispersive) direction and 30 cm in the y (non-dispersive) direction [74]. The CRDCs are filled with 80% carbon tetrafluoride (CF_4) and 20% isobutane (C_4H_{10}). A negative bias voltage is applied across each CRDC in the y direction. When nuclei pass through the CRDC the gas is ionized and the electrons drift toward the anode wire. Bordering the anode wire are 224 cathode pads, each 2.54 mm wide [74]. The collection of charge in the anode induces a positive charge on the cathode pads. The interaction point in the x (dispersive) direction for the incoming particle is determined by fitting the measured charge on the pads with a Gaussian distribution. The y (non-dispersive) position of the interaction is determined from the drift time of the electrons to the anode measured with respect to the timing signal from the E1 scintillator.

In order to calibrate the x and y positions of the CRDCs during the experiment, thick masks with holes and slits drilled into them at known positions can be inserted in front of each CRDC. An example of a CRDC calibration run using a mask is shown in Figure 3.4. During the experiment, the drift time can vary due to changes in the composition of the CRDC fill gas. Therefore, mask runs for each CRDC were taken at several times during the experiment and the slope of the linear y position calibration was adjusted run-by-run to align the centroids of the measured y positions for the sulfur isotopes of interest.

From the xy-positions measured in the CRDCs (referred to as xfp and yfp, respectively), the dispersive (afp) and non-dispersive (bfp) angles at the S800 focal plane can be calculated. The trajectory of the ions from the reaction target through the spectrograph is reconstructed using an inverse map of the S800 magnetic field generated from the ion optics code COSY infinity [75]. The positions and angles calculated at the focal plane are related to quantities

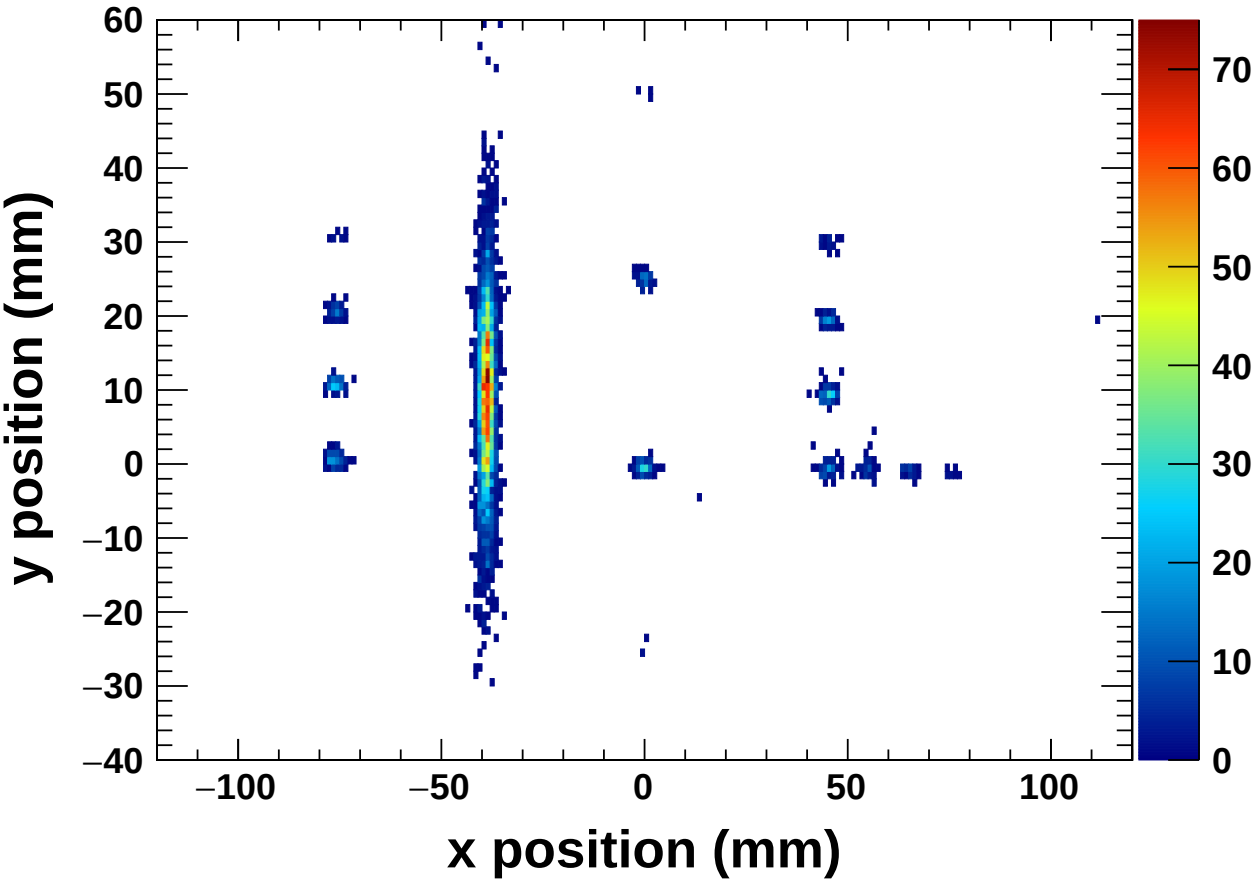

Figure 3.4: Typical calibrated mask run for CRDC1 (upstream) taken from the ^{38}S setting.

at the reaction target through the inverse map (S^{-1}) by:

$$(ata, yta, bta, dta) = S^{-1}(xfp, afp, yfp, bfp). \tag{3.5}$$

Here, *ata* and *bta* are the dispersive and non-dispersive angles at the target, *yta* is the y position at the target, and *dta* is the deviation in energy relative to a particle taking the central path through the spectrograph ($dta = (E - E_0)/E_0$). The scattering angle of the projectile in the laboratory frame can be written as:

$$\theta = \arcsin\left(\sqrt{\sin^2(ata) + \sin^2(bta)}\right). \tag{3.6}$$

The uncertainty in the scattering angle due to the position resolution of the CRDCs is about 2 mrad [74].

As mentioned earlier in this section, there are correlations between the time-of-flight differences between plastic scintillators XFP-E1 and OBJ-E1 and the dispersive positions and angles (xfp and afp) measured in the S800 focal plane. These correlations are corrected for by removing the linear dependence on xfp and afp via:

$$\mathrm{XFP_{corr}} = \mathrm{XFP} + A_1 \times xfp + A_2 \times afp, \tag{3.7}$$

$$\mathrm{OBJ_{corr}} = \mathrm{OBJ} + B_1 \times xfp + B_2 \times afp. \tag{3.8}$$

An example of the ΔE-ToF particle identification using the S800 ionization chamber and the corrected OBJ-E1 time of flight for the ^{44}S setting is shown in Figure 3.5. The vertical lines spanning energy loss at a constant time of flight are due to pileup in the ionization chamber. The total number of pileup counts at the time of flight corresponding to ^{44}S are less than 3% of the counts in the energy loss peak.

3.2.2 Isomer Tagging

The ^{43}S secondary beam at the NSCL is known to be produced with some fraction of the ^{43}S nuclei in the low-lying $7/2^-$ excited state at 320 keV with a half-life of 415 ns [50, 51]. In order to infer if the Coulomb excitation occurred with this isomeric state as the initial state, the CsI(Na) hodoscope at the S800 focal plane [76] was utilized. The hodoscope consists of 32 closely-packed CsI(Na) scintillator crystals and is located downstream of the E1 scintillator. A 6.35 mm aluminum plate is added 10.5 cm before the hodoscope to stop the

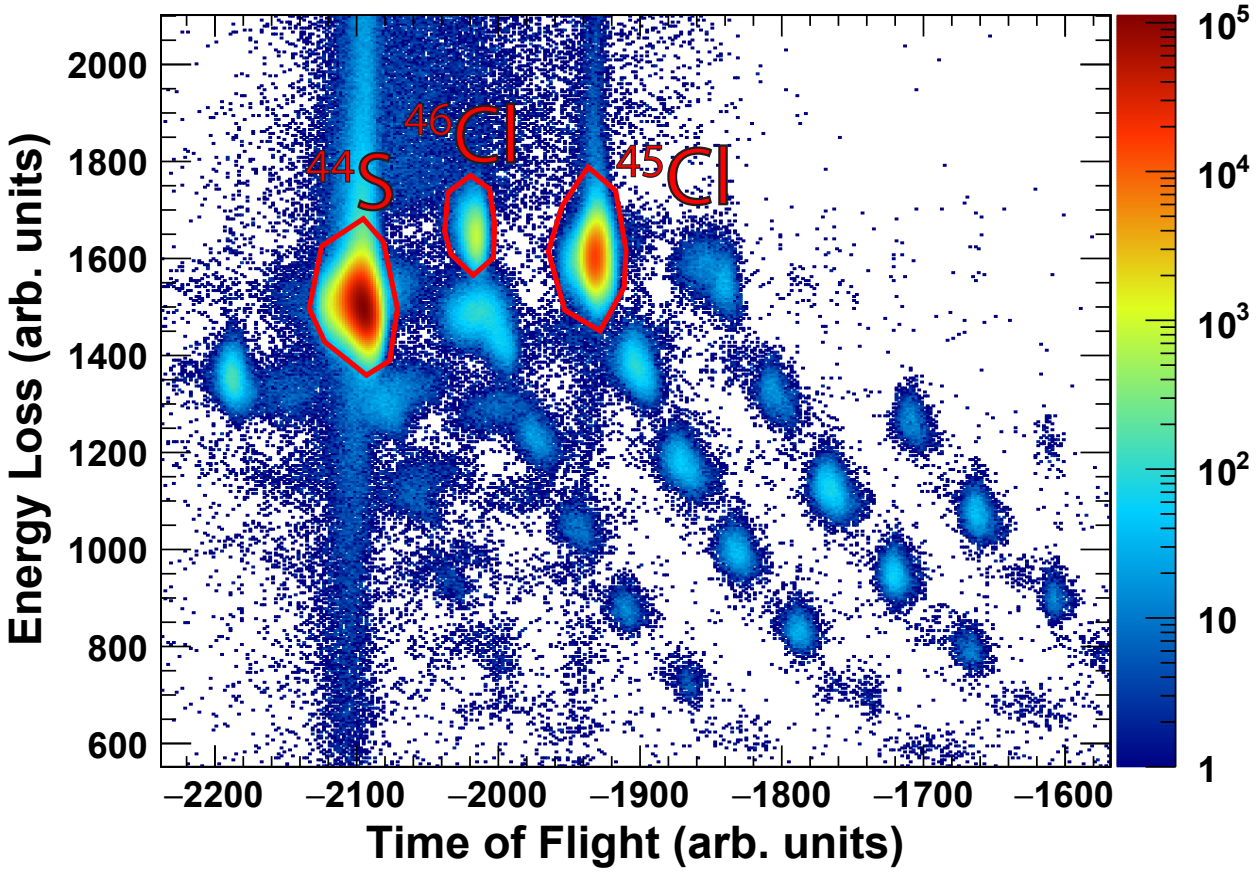

Figure 3.5: Particle identification plot utilizing energy loss and time of flight for the ^{44}S setting. The energy loss is measured in the S800 ionization chamber and is proportional to Z^2 and the time of flight is measured between the OBJ and E1 plastic scintillators and is proportional to A/Z.

reaction products in the so-called IsoTagger configuration [77]. Suppose a short-lived level above the $7/2^-$ isomeric state is populated in Coulomb excitation and then decays back to the isomer via γ-ray emission. The prompt γ ray can be measured by CAESAR surrounding the target. Since the flight path through the S800 spectrograph is approximately 15 m, a particle moving at about v=0.4c will take roughly 125 ns to traverse the S800 spectrograph. Consequently, the isomer (415 ns half-life) will predominantly decay after reaching the S800 focal plane. In this experiment, the aluminum stopper plate and CsI(Na) array were used to search for 320-keV γ rays from the decay of the isomeric state in coincidence with prompt γ

rays from higher-lying states in ^{43}S at the reaction target.

3.3 In-Beam γ-Ray Spectroscopy with CAESAR

To measure de-excitation γ rays following the Coulomb excitation of the neutron-rich sulfur isotopes, the 492 mg/cm^2 ^{209}Bi reaction target at the target position of the S800 spectrograph was surrounded by the high-efficiency CAESium-iodide scintillator ARray CAESAR [14]. CAESAR consists of 192 total CsI(Na) detectors arranged into 10 rings and provides about 95% solid angle coverage. 48 of the detectors are $3 \times 3 \times 3$ inches while the remaining 144 crystals are 2×2 inches on the front face and 4 inches in depth. An illustration of the arrangement of the 192 CsI(Na) detectors is shown in Figure 3.6. Rings A (most upstream) and J (most downstream) have 10 detectors each, rings B and I have 14 detectors each, and the middle six rings C-H each hold 24 detectors. The full-energy-peak efficiency of the array exceeds 35% for 1 MeV γ rays emitted by a source at rest. The in-beam energy resolution is approximately 9.2% full width at half maximum (FWHM) for 1 MeV γ rays emitted from a nucleus traveling at 0.35c [14]. A photograph of CAESAR set up in front of the S800 spectrograph is provided in Figure 3.7.

3.3.1 Interaction of γ Rays with Matter

The CsI(Na) scintillator crystals in the CAESAR detectors are housed in an aluminum casing and coupled to a photomultiplier tube (PMT). When γ rays interact with the detector material, the atoms in the scintillator become excited or ionized resulting in the emission of de-excitation photons. When this scintillation light strikes the photocathode in the PMT, electrons are ejected via the photoelectric effect. The photoelectrons are accelerated due to

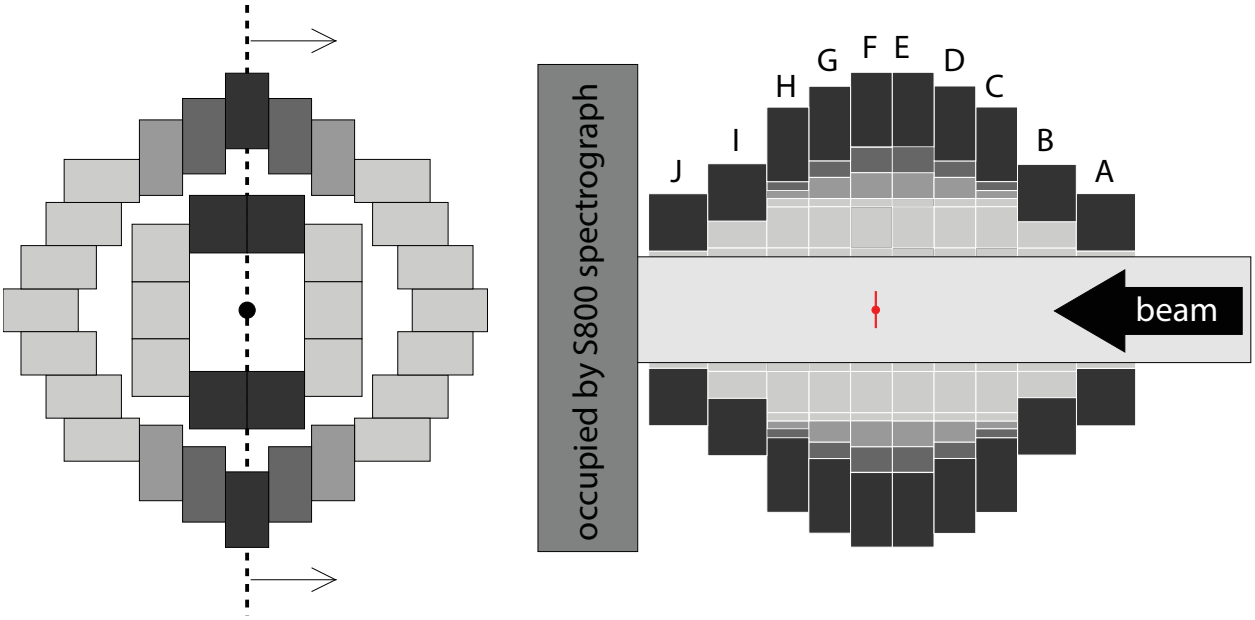

Figure 3.6: Illustration of the arrangement of CAESAR into 10 rings of detectors. Left: cross-sectional view of rings F and J perpendicular to the beam axis. Right: the $3 \times 3 \times 3$ inch detectors occupy the two most upstream (A,B) and two most downstream (I,J) rings while the $2 \times 2 \times 4$ inch detectors occupy the six middle rings (C-H). The target position is shown in red. Figure taken from [14].

an applied voltage across the PMT and collide with a series of dynodes, which release many additional electrons. The resulting signal from the electric current, which is proportional to the energy of the initial γ ray, can then be read out. Since PMTs are affected by magnetic fields, several layers of μ metal were added between the aluminum housing and the PMTs. [14]. In addition, a large soft-iron plate (the green metal sheet at the back of Figure 3.7) was installed between CAESAR and the S800 spectrograph to shield the detectors from the S800 fringe field.

There are three main processes by which γ rays interact with matter: the photoelectric effect, Compton scattering, and pair production. The photoelectric effect is the dominant interaction channel for γ ray energies below a few hundred keV [71]. In photoelectric absorption, the γ ray transfers all of its energy E_γ to an electron, ejecting it from the atom.

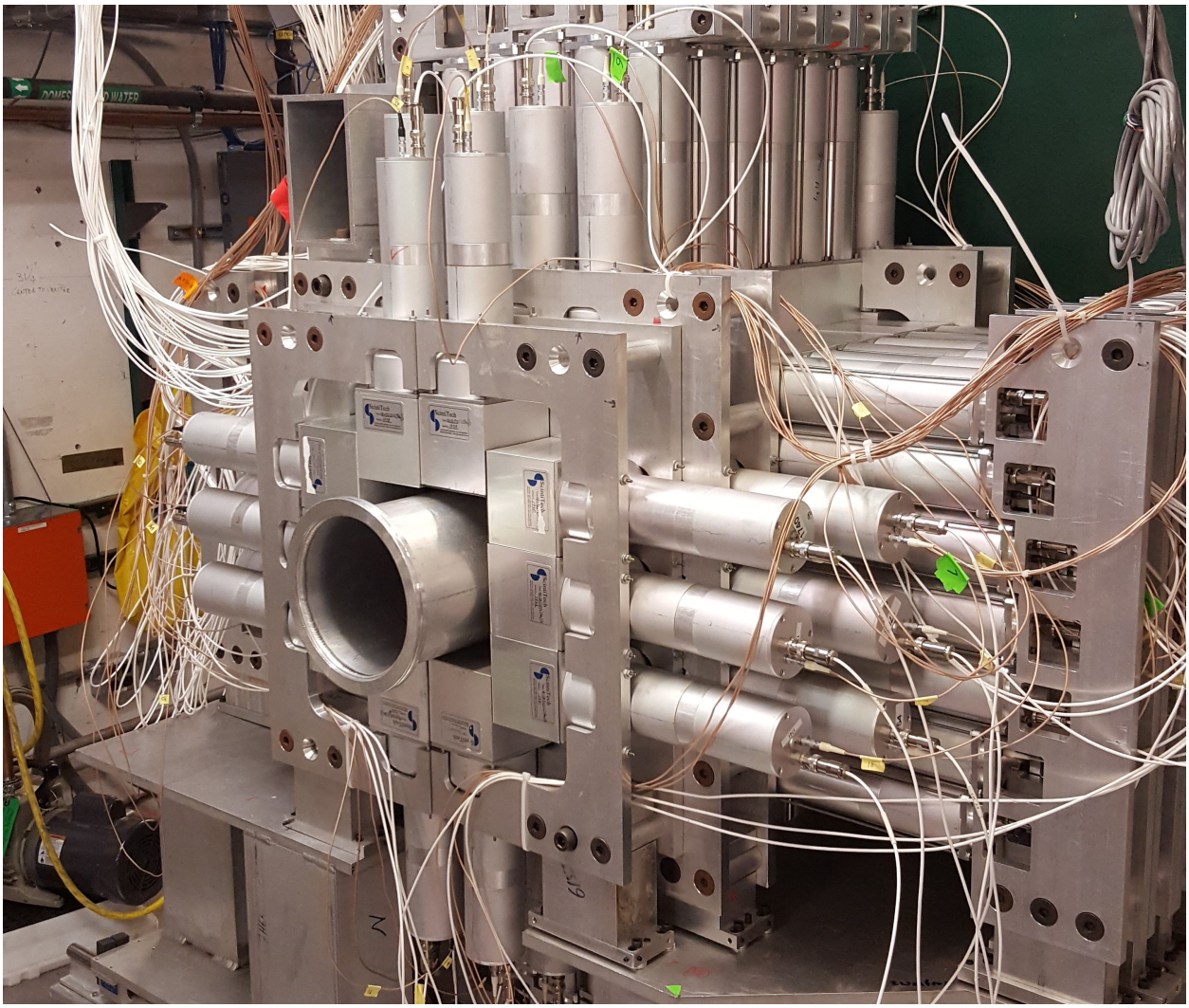

Figure 3.7: Photograph of the 192 CsI(Na) detectors composing CAESAR in front of the S800 spectrograph.

The remaining energy of the electron E_{e^-} is:

$$E_{e^-} = E_\gamma - E_b, \tag{3.9}$$

where E_b is the typically small binding energy of the electron. In this case, assuming the electron remains in the detector volume, the full energy of the initial γ ray is collected. In this case, a count will be added to the full-energy peak in the spectrum shown in Figure 3.8.

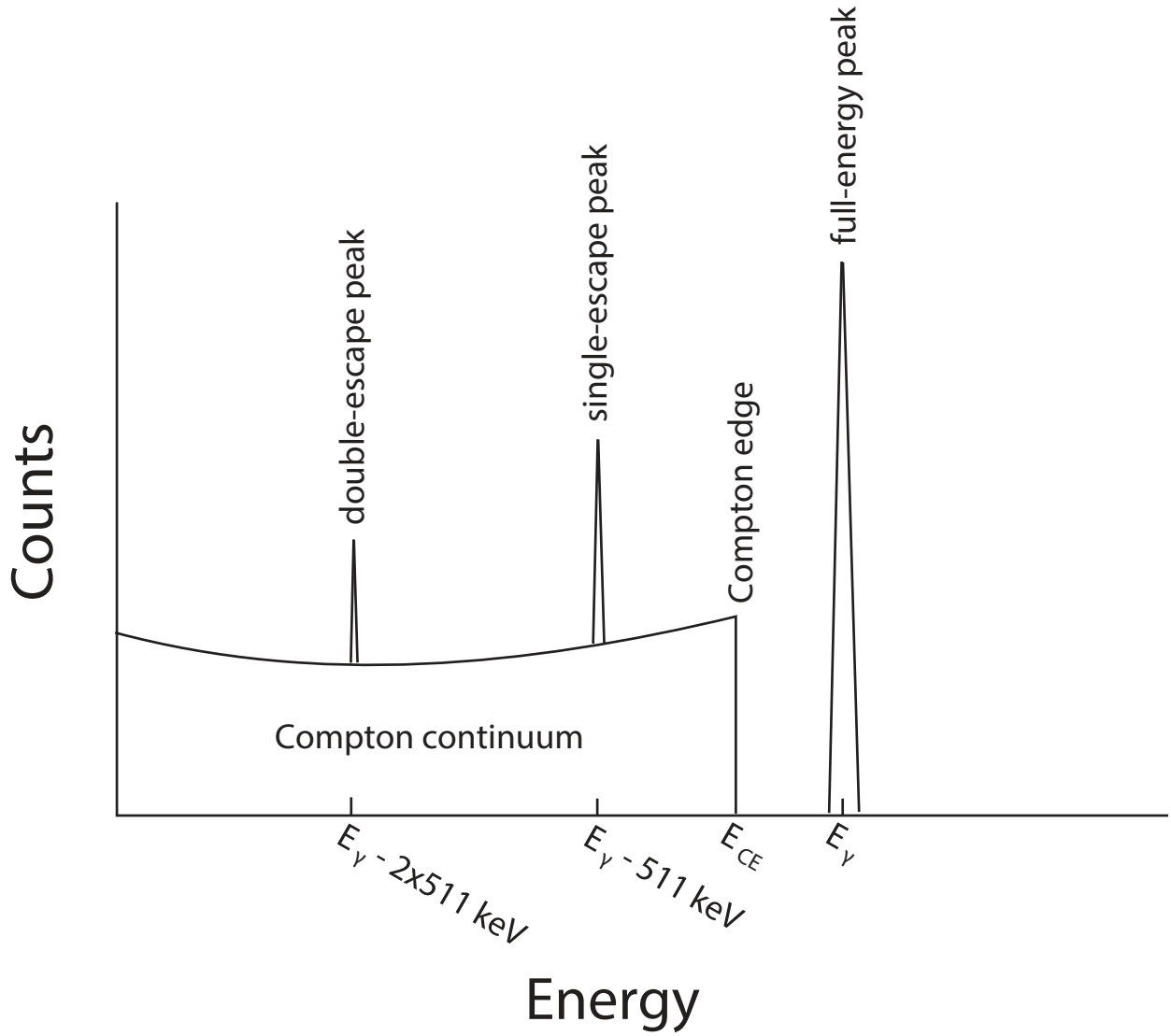

Figure 3.8: Illustration of the response of a γ-ray detector to many monoenergetic γ rays showing characteristic features including the full-energy peak, Compton edge, Compton continuum, and single and double-escape peaks. Figure taken from [11].

In Compton scattering, a γ ray with initial energy E_γ inelastically scatters off of an atomic electron, transferring only some of its energy. The remaining energy of the γ ray E'_γ is related to the initial energy by:

$$E'_\gamma = \frac{E_\gamma}{1 + \left(\frac{E_\gamma}{m_e c^2}\right)(1 - \cos\theta)}, \tag{3.10}$$

where θ is the scattering angle and m_e is the mass of the electron. The minimum energy transfer is 0 for scattering at 0° while the maximum energy transfer is for scattering at 180°:

$$E_{CE} = \frac{2E_\gamma^2}{m_e c^2 + 2E_\gamma}. \tag{3.11}$$

Here, the maximum energy transferred to the electron E_{CE} is the energy of the Compton edge. As a result, the energy collected in the detector from Compton scattering ranges from 0 to E_{CE} leading to a feature in the energy spectrum known as the Compton continuum as seen in Figure 3.8. The scattered γ ray can leave the detector volume or undergo multiple Compton scatterings until it is absorbed via the photoelectric effect. Compton scattering is the dominant interaction process for γ rays with energy between a few hundred keV and a few MeV [71].

If the γ ray energy is above two times the rest mass of the electron, pair production can occur through interaction with the electric field of one of the nuclei in the detector material. In this case, the γ ray is converted into an electron-positron pair and through energy conservation:

$$E_\gamma = E_{e^-} + E_{e^+} + 2m_e c^2. \tag{3.12}$$

Here E_{e^-} and E_{e^+} are the kinetic energies of the electron and positron and $m_e c^2 = 511$ keV. The positron will quickly annihilate with an electron in the detector material producing two 511-keV photons. These photons can undergo photoelectric absorption, Compton scattering, or leave the detector. If one of the annihilation photons escapes the detector while the other is fully absorbed, the total energy detected will be $E_{SE} = E_\gamma - 511$ keV leading to a single-escape peak in the spectrum. If both annihilation photons escape the detector, the double-escape peak will be at $E_{DE} = E_\gamma - 1022$ keV. The single and double-escape peaks

are shown in Figure 3.8. Pair production only becomes the dominant interaction process for γ-ray energies of several MeV [71].

3.3.2 Doppler Reconstruction

In this experiment, the velocity of the sulfur isotopes at mid-target was about 0.38c on average. Therefore, the γ rays are emitted from a source moving at a relativistic velocity with respect to the detectors in the laboratory frame. As a result, the energy of the γ ray measured in the laboratory frame E_{lab} is Doppler shifted with respect to the energy of the γ ray in the rest frame of the nucleus E_{rest} according to:

$$E_{\mathrm{rest}} = E_{\mathrm{lab}}\gamma(1 - \beta\cos\theta), \tag{3.13}$$

where γ is the relativistic factor, $\beta = v/c$ is the velocity of the nucleus relative to the speed of light, and θ is the angle of emission of the γ ray with respect to the velocity vector of the nucleus in the laboratory frame. In order to precisely Doppler reconstruct the rest-frame energy of the γ ray, the uncertainty in the detection angle θ should be kept as small as possible. The high-granularity of CAESAR resulting from the use of 192 individual detectors provides acceptable angular resolution. The total energy resolution of a detector is related to the uncertainties in detection angle ($\Delta\theta$) and beam velocity ($\Delta\beta$) by [56]:

$$\left(\frac{\Delta E_\gamma}{E_\gamma}\right)^2 = \left(\frac{\beta\sin\theta}{1-\beta\cos\theta}\right)^2 (\Delta\theta)^2 + \left(\frac{\cos\theta-\beta}{\left(1-\beta^2\right)(1-\beta\cos\theta)}\right)^2 (\Delta\beta)^2 + \left(\frac{\Delta E_{\mathrm{intr}}}{E_\gamma}\right)^2, \tag{3.14}$$

where ΔE_γ is the FWHM of the peak at energy E_γ. The uncertainty in the velocity $\Delta\beta$ arises from the fact that the γ decay can occur anywhere in the reaction target. As the

nucleus passes through the reaction target, it losses energy and its velocity is lowered. The uncertainty in detection angle $\Delta\theta$ is dominated by the finite angle coverage of the detector. ΔE_{intr} is the intrinsic energy resolution of the detector. For CAESAR, the detectors have an intrinsic energy resolution of about 7% at 1 MeV [14]. The intrinsic energy resolution characteristically goes as $1/\sqrt{E_\gamma}$ [71].

3.3.3 Nearest-Neighbor Addback

In order to increase the full-energy peak efficiency, a technique known as nearest-neighbor addback can be employed. At typical γ-ray energies, Compton scattering has a significant contribution to the observed γ-ray spectra. Due to the selectivity of the states populated in intermediate-energy Coulomb excitation, the average number of de-excitation γ rays for each excitation (the γ-ray multiplicity) is low. Suppose that two neighboring crystals in CAESAR register within a short time coincidence window. Since the average γ-ray multiplicity is low, the probability that two coincident γ rays hit two neighboring crystals in CAESAR is lower than the probability that one γ ray has Compton scattered from one detector into the neighboring detector. Assuming that the Compton scatter has occurred, the full energy of the γ ray can be recovered by summing the energies deposited in the neighboring detectors together. This transfers two counts in the Compton continuum into one count in the full-energy peak of Figure 3.8. For in-beam γ-ray spectroscopy with CAESAR, the detector with the highest energy deposition is used to determine the emission angle of the γ ray for Doppler reconstruction. In source measurements, utilizing nearest-neighbor addback has been shown to recover more than 20% of the full-energy peak intensity for γ-ray energies above 1 MeV and more than 30% of the full-energy peak intensity for γ-ray energies above 2 MeV [14].

In order to derive the results discussed in Chapter 5, both addback and non-addback

spectra were utilized. To determine Coulomb excitation cross sections from the de-excitation γ-ray yields, no addback was applied to the singles spectra. Using addback would add an additional systematic uncertainty to the γ-ray detection efficiency, which would in turn increase the uncertainty on the cross section. Specifically, when using addback the energy thresholds for each detector need to be considered. Furthermore, the efficacy of the GEANT4 simulation for handling the scatter between detectors, which is sensitive in reality to the detector housing and insensitive layers of the scintillator crystals, would have to be studied in great detail. Therefore, the additional uncertainty in the detection efficiency does not justify the gain in full-energy-peak statistics provided by employing addback. The gain in statistics afforded by addback was exploited in the multiplicity-two γ-γ plots used to identify coincidences and in the multiplicity-one plots used to identify transitions to the ground state. Here, using addback properly converts a multiplicity-two event where one γ ray Compton scatters from one detector to another detector into a multiplicity-one event.

3.3.4 CAESAR Calibrations

The first step in the analysis of the data was to perform the necessary calibrations and corrections for the detector systems used in the experiment. To begin, all 192 CAESAR detectors were energy calibrated using γ-ray spectra obtained from a set of standard γ-ray calibration sources including ^{22}Na, ^{60}Co, ^{88}Y, ^{137}Cs, ^{133}Ba, and ^{207}Bi. In addition, natural background lines from the decays of ^{40}K and ^{208}Tl were utilized. Energies ranging from 356 keV to 2614 keV were used in the calibration. To account for drifts in energy calibration over time, calibration runs were taken at the beginning and end of the experiment. Furthermore, the calibrations were performed with the rigidities of the S800 dipoles set since the detector PMTs are sensitive to magnetic fields. For all detectors individually, the channel

numbers for the full-energy-peak centroids from the source data were obtained through Gaussian fits and mapped to the known γ-ray energies with a second order polynomial. The results of the energy calibration for the ^{88}Y source are shown in Figure 3.9.

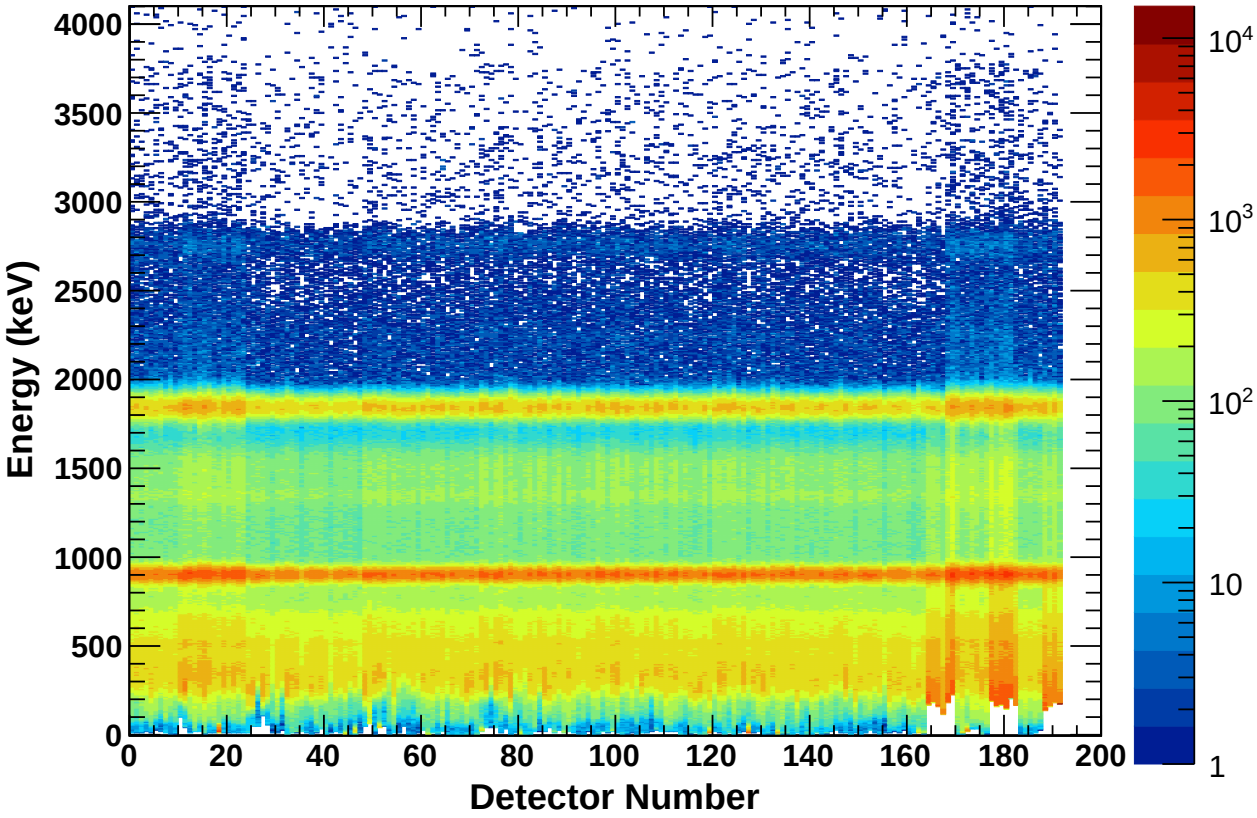

Figure 3.9: Energies after calibration for the 192 CAESAR detectors for the ^{88}Y source. The 898-keV and 1836-keV transitions are aligned for all detectors. The 2614-keV transition from room background is also visible.

The timing calibration was performed for all 192 detectors using a portion of the in-beam data. The CAESAR timing is taken relative to the time of flight of the projectile from the OBJ scintillator to the E1 scintillator at the S800 focal plane. However, the timing dispersion for CAESAR is 250 ps/channel while the timing dispersion for the plastic scinitllators is 100 ps/channel. Therefore, the corrected CAESAR time is given by:

$$\mathrm{CAESAR}_{\mathrm{corrtime}} = \mathrm{CAESAR}_{\mathrm{time}} - \mathrm{E1}_{\mathrm{time}} \times (0.1/0.25) - \mathrm{OBJ}_{\mathrm{time}} \times (0.1/0.25). \quad (3.15)$$

For detector hits with laboratory energies greater than 500 keV, the corrected CAESAR timing spectrum was generated for all detectors using one of the in-beam runs for the ^{38}S setting. One detector was then chosen as the reference and the centroids of the timing spectra for all other detectors were aligned to the timing centroid for the reference detector. The results of the timing calibration are shown in Figure 3.10.

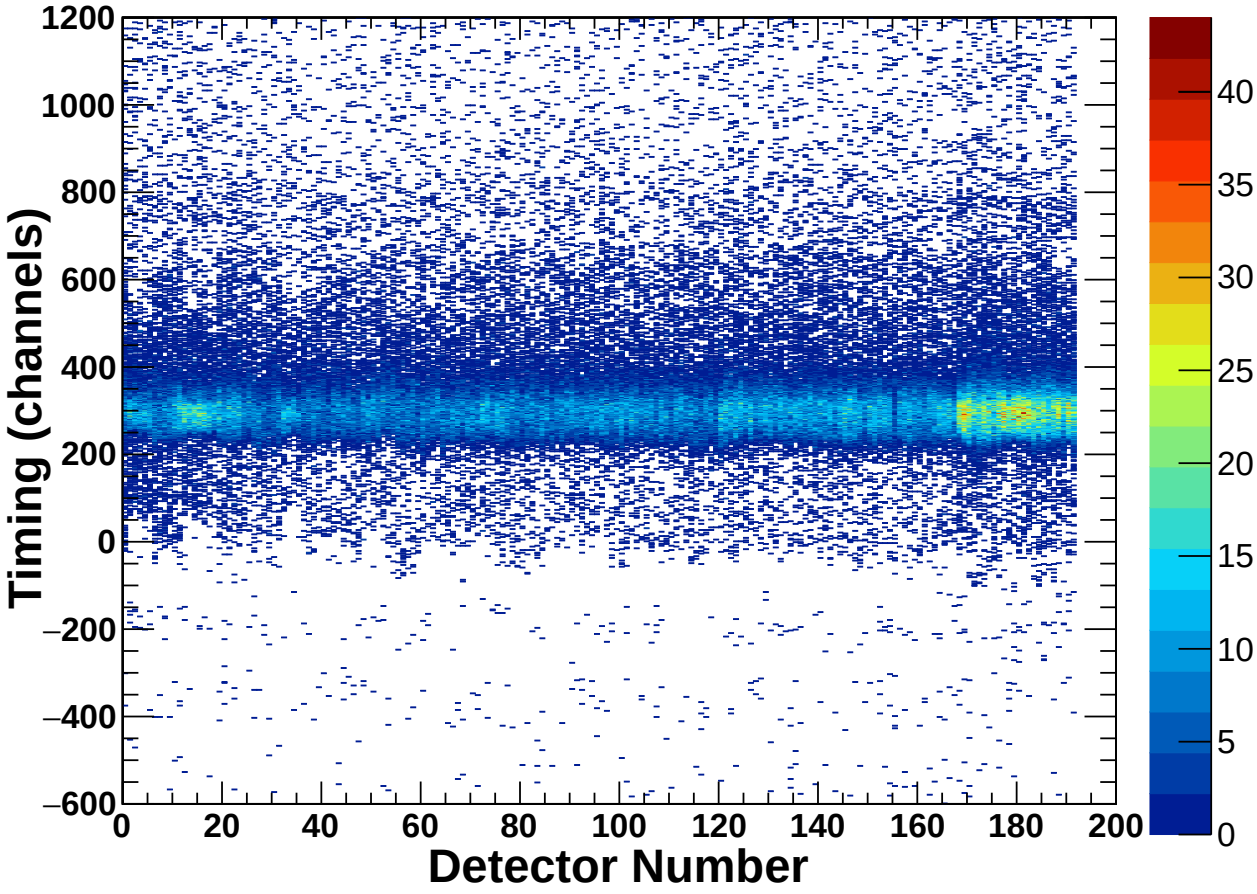

Figure 3.10: Alignment of the corrected CAESAR timings for all 192 detectors after calibration gated on γ-ray energies above 500 keV in the laboratory frame for one of the ^{38}S runs.

In order to avoid issues stemming from high count rates, the absolute full-energy peak γ-ray detection efficiency of CAESAR was determined using a low-activity ^{207}Bi source (around 3433 decays per second). The β^+ decay of ^{207}Bi results in γ-ray transitions with energies

at 570 keV, 1064 keV, and 1770 keV. In this measurement, the efficiency was determined from the number of full-energy peak counts above background (modeled with an exponential) divided by the number of emitted γ rays at that energy by the source. Furthermore, efficiency data points for ^{60}Co, ^{88}Y, and ^{207}Bi sources were obtained using coincidences with a $LaBr_3$(Ce) scintillator placed in the beam pipe near the source. Consider, for example, gating on the 1332-keV full-energy peak from a ^{60}Co source measured in the $LaBr_3$(Ce) detector. Since the 1332-keV transition feeds the 1173-keV level, the number of coincident 1173-keV full-energy peak counts in CAESAR divided by the total number of 1332-keV counts in the $LaBr_3$(Ce) detector within the applied gate is the absolute full-energy peak efficiency for CAESAR at 1173 keV. More details on the method are provided in [78].

A GEANT4 [79] simulation of CAESAR called UCCAESAR was developed to determine the in-beam efficiency of the array (for some details on the simulation see [11, 80]). The simulation takes into account the Lorentz boost, energy loss of the incoming projectiles in the reaction target, absorption of emitted γ rays in the target and beam pipe, the angular distributions of the γ rays emitted following Coulomb excitation, and the lifetime of the populated state. The efficiencies predicted from the simulation are compared with the efficiencies extracted from source data in Figure 3.11. The vertical error bars for the experimental data in the direct efficiency determination from the ^{207}Bi source include statistical and fit uncertainties added in quadrature with a 3% systematic uncertainty in the source activity. The vertical error bars for the experimental data from coincidences with the $LaBr_3$(Ce) detector include statistical and fit uncertainties added in quadrature with uncertainties due to random coincidences, $\gamma - \gamma$ angular correlations, and scattering out of the $LaBr_3$(Ce) scintillator (see also [78]). On average, the experimental source efficiencies are 5% higher than the simulated source efficiencies. Accordingly, in the analysis of the

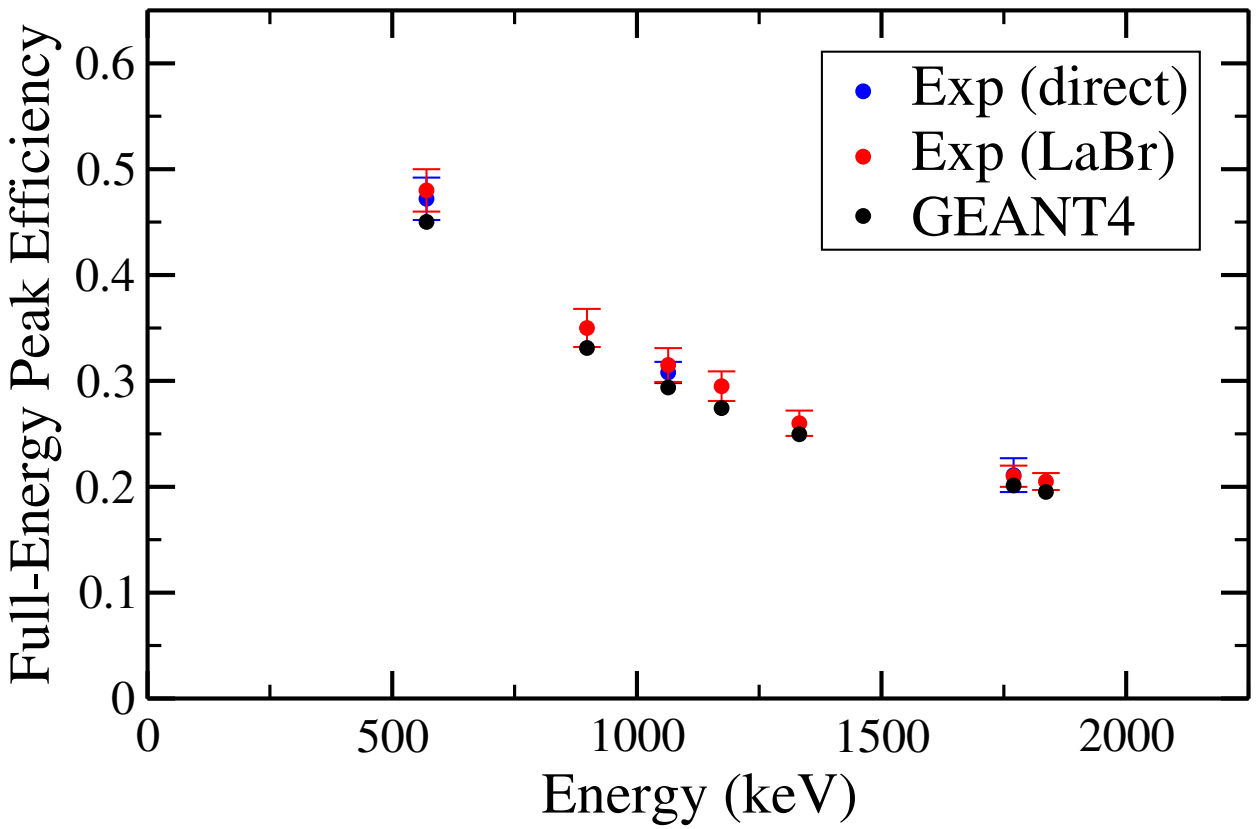

Figure 3.11: Full-energy peak efficiency of CAESAR as a function of energy as determined from direct measurement of a low-activity ^{207}Bi source and from coincidence measurements with a $LaBr_3$(Ce) detector for ^{60}Co, ^{88}Y, and ^{207}Bi sources compared to predictions from GEANT4 simulations. The efficiency curves here were produced treating the 192 detectors of CAESAR independently (no addback applied).

neutron-rich sulfur isotopes the in-beam efficiency of CAESAR was taken as the GEANT4 efficiency times a scaling factor of 1.05 and a systematic uncertainty of 5% was adopted following the method of [81].

The energy resolution of CAESAR was parameterized in the form:

$$\sigma(E) = aE^b, \tag{3.16}$$

where the resolution σ is related to the FWHM by FWHM $= 2\sqrt{2\ln(2)}\sigma$. The fit parameters a and b for each ring of CAESAR were found from the widths of full-energy peaks from source

data over the same range of energies used for the energy calibration. This parameterization was then used as an input for the CAESAR GEANT4 simulation to set the laboratory-frame resolution as a function of energy. The values of a and b (for energies in keV) are provided in Table 3.2 for each ring.

Table 3.2: Energy resolution parameters for each of the 10 rings of CAESAR for energies in keV.

Ring	a	b
A	0.6346	0.5589
B	0.5376	0.5826
C	0.7518	0.5252
D	0.6151	0.5507
E	0.6416	0.5475
F	0.6099	0.5511
G	0.6183	0.5507
H	0.5899	0.5600
I	0.6041	0.5691
J	0.5005	0.5930

Chapter 4

Data Analysis and Results

4.1 General Method

Reduced transition strengths for excited states in the neutron-rich sulfur isotopes ^{38,40,42,43,44}S were determined by measuring the cross sections for the excitation of these states in intermediate-energy Coulomb excitation. The experimental excitation cross section can be written as:

$$\sigma_{CE} = \frac{N_{\text{decays}}}{N_{\text{beam}} n_{\text{target}}}, \tag{4.1}$$

where N_{decays} is the total number of γ decays from the excited state to all final states, N_{beam} is the number of incoming beam particles incident on the reaction target, and n_{target} is the areal number density of the reaction target.

The areal number density of the 492(4) mg/cm^2 ^{209}Bi target used in the experiment is 1.42(1)$\times 10^{-6}$ nuclei/mb and can be calculated using:

$$n_{\text{target}} = \frac{\rho_A N_A}{M}, \tag{4.2}$$

where ρ_A is the areal density of the target, N_A is Avogadro's number (6.0221409×10^{23} particles/mole), and M is the molar mass of the target.

The number of incoming beam particles is given by:

$$N_{\text{beam}} = \frac{N_S \cdot DS_{S800}}{LT_{S800}}. \tag{4.3}$$

Here, N_S is the number of sulfur projectiles of interest detected at the S800 focal plane in the gate applied on the ΔE-ToF particle identification plot, DS_{S800} is the downscale factor applied to S800 particle triggers, and LT_{S800} is the livetime of the S800 data acquisition (DAQ) system, which is triggered by the E1 scintillator. Note that there are two trigger conditions, one for particles that is downscaled and one for particle-γ coincidences that is not downscaled. After a trigger initiates the readout cycle of the event, there is an amount of time in which the DAQ cannot process another trigger known as the deadtime. During this deadtime, any particle interacting with the E1 scintillator will not be read out by the DAQ. The number of times the DAQ is read out is the number of S800 singles events ($N_{singles}$). This number is extracted from the data using information from the S800 trigger register included with each event. The S800 livetime is found by dividing the number of S800 singles by the total number of events meeting the S800 trigger condition recorded by the S800 scaler module ($S800.Triggers$), which is not affected by the deadtime:

$$LT_{S800} = \frac{N_{singles}}{S800.Triggers}. \tag{4.4}$$

A downscaler was applied to the S800 singles in order to reduce the deadtime of the system. For all settings in this experiment, a downscale factor of 20 was used, meaning that only every 1/20 S800 events meeting the trigger condition of the DAQ were read out.

The total number of γ decays is the number of counts in the full-energy peak detected by

CAESAR N_{fep} divided by the corresponding energy-dependent full-energy peak efficiency $\epsilon(E_\gamma)$ and corrected for the livetime for detecting a reaction product in the S800 focal plane in coincidence with a γ ray in CAESAR

$$N_{\text{decays}} = \frac{N_{fep}}{\epsilon(E_\gamma) \cdot LT_{coinc}}. \tag{4.5}$$

No downscale factor was applied for particle-γ (S800-CAESAR) coincidence events. The livetime for coincidences LT_{coinc} is given by:

$$LT_{coinc} = \frac{N_{coinc}}{Coinc.Triggers}, \tag{4.6}$$

where N_{coinc} is the number of coincidence events recorded by the S800 trigger register and $Coinc.Triggers$ is the total number of events meeting the coincidence trigger condition recorded by the scaler module, which is not affected by the deadtime.

The average livetime for particle triggers in the S800 magnetic spectrograph LT_{S800} and the average livetime for particle-γ coincidences LT_{coinc} for each setting, along with the number of beam particles for the sulfur isotopes of interest corrected for S800 livetime and the downscaler factor of 20 (N_{beam}), are provided in Table 4.1. The quoted uncertainties are statistical. The efficiency of both CRDCs combined relative to the ionization chamber was approximately 99% for all settings.

Each time a particle triggers the E1 scintillator in the S800 focal plane, a coincidence window between particles in the S800 and γ rays in CAESAR is opened. In order to reduce background from random coincidences measured in CAESAR in the Doppler-corrected γ-ray spectra, prompt time-energy cuts were utilized. An example of the two-dimensional

Table 4.1: Corrected number of sulfur isotopes N_{beam} and average livetimes for particle triggers in the S800 LT_{S800} and S800-CAESAR coincidences LT_{coinc} for each of the settings.

Setting	N_{beam}	LT_{S800}	LT_{coinc}
^{38}S	$4.522(2) \times 10^8$	0.9159(3)	0.8548(4)
^{40}S	$4.106(2) \times 10^8$	0.9151(4)	0.8543(4)
^{42}S	$1.0463(3) \times 10^9$	0.8662(2)	0.8454(3)
^{43}S	$7.343(3) \times 10^8$	0.9237(3)	0.8830(3)
^{44}S	$2.934(2) \times 10^8$	0.9557(4)	0.9512(5)

prompt time-energy cut used for ^{40}S is provided in Figure 4.1. Applying the time-energy cut removes background counts without affecting the prompt γ rays from de-excitation following Coulomb excitation.

The number of full-energy peak counts N_{fep} was determined through the use of GEANT4 simulations. As discussed in Subsection 3.3.4, the UCCAESAR GEANT4 simulations take into account the incoming beam energy, energy loss in the 492 mg/cm^2 ^{209}Bi target, absorption of γ rays in the target and beam pipe, the angular distributions of the emitted γ rays, and the state lifetime. The GEANT4 simulation outputs histograms as ROOT files [82] that were converted into ROOT TF1 fit functions using the ParamFunctor class. Multiple TF1s, including a double exponential background model, were then summed together with individual scaling factors and energy shifts in order to perform a simultaneous fit over the desired energy range of the spectrum. In addition, UCCAESAR was used to simulate the effect of the background lines at 511 keV from electron-positron annihilation and 1460 keV from the β decay of ^{40}K (naturally-occurring background radiation) in the laboratory frame. These spectra were Doppler-corrected in the same way as the prompt γ-ray simulations and added to the fit function. In general, the fit functions were of the form:

$$f(E) = a_1 \exp(a_2 E) + a_3 \exp(a_4 E) + b_1 S_{511} + b_2 S_{1460} + \sum_i c_i S_i(E - d_i). \tag{4.7}$$

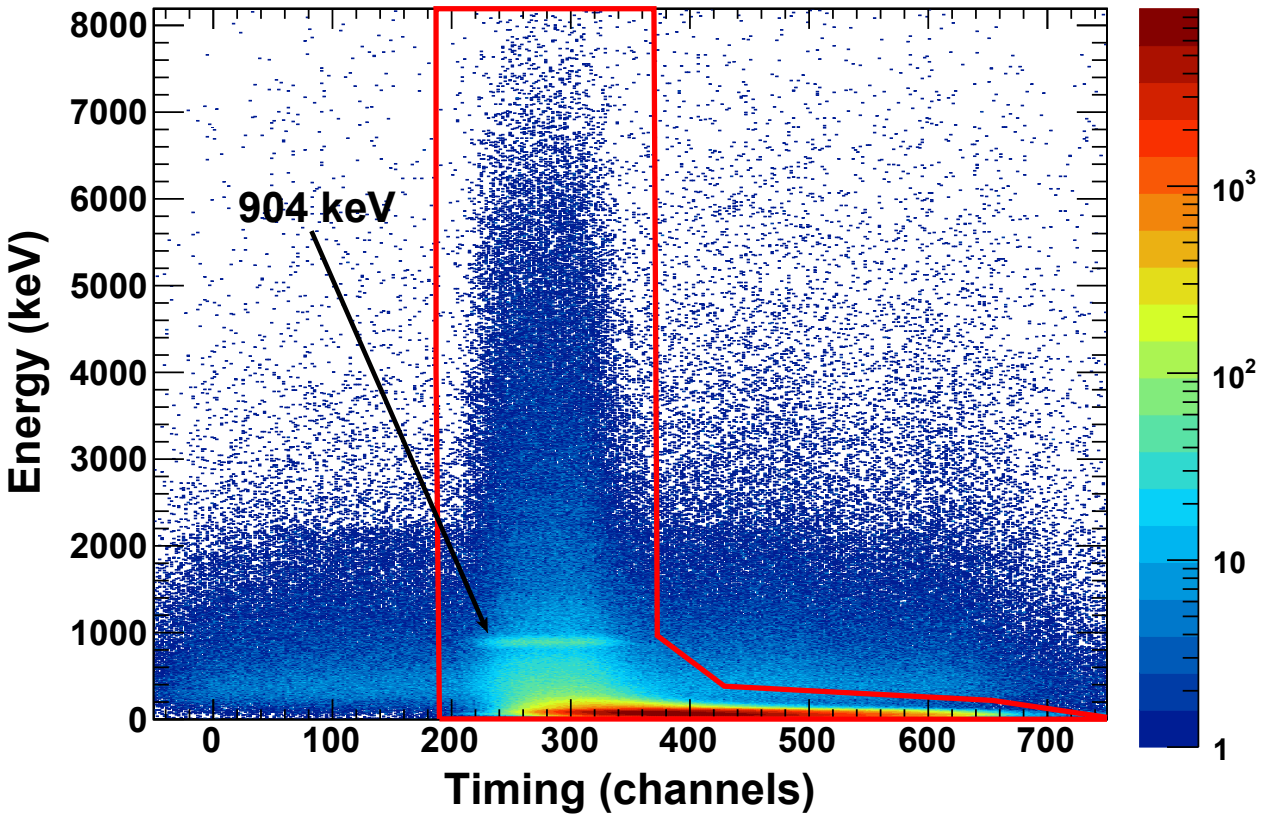

Figure 4.1: Doppler-corrected energy versus corrected CAESAR timing gated on ^{40}S. As seen from the 904-keV peak, the prompt time-energy cut (red) removes random background counts without affecting the prompt γ decays that occur after Coulomb excitation.

Here, the first two terms compose the double exponential background and b_1 and b_2 are scaling factors for the Doppler-shifted 511 keV and 1460 keV background spectra (S_{511} and S_{1460}). The simulations of the observed prompt γ-ray transitions S_i are scaled by the factors c_i and are allowed to shift in energy by the parameter d_i. In the fits, d_i was constrained to be less than 10 keV. The values of the parameters are determined by fitting to the experimental spectrum using the MINUIT fitting package [83] in ROOT. The experimental number of full-energy peak counts N_{fep} is taken as the scaling factor c_i times the number of full-energy peak counts in the GEANT4 simulation and is divided by the livetime for coincidences LT_{coinc} and the efficiency to calculate the total number of γ decays N_{decays}. After the

Coulomb excitation cross section was determined, the reduced transition strength $B(E2)$ was calculated using the relativistic Alder-Winther theory with a Mathematica script [63].

4.2 Results for Even-Even Neutron-Rich Sulfur Isotopes

The experimental data were analyzed using the GRUTinizer software package built on the ROOT framework, which is available at [84] and also described in [85]. The results for the intermediate-energy Coulomb excitation of the even-even neutron-rich isotopes ^{38,40,42,44}S are described in the following subsections. Extracted $B(E2)$ values are compared to calculations using the SDPF-MU interaction [25] with effective proton and neutron charges of 1.35 and 0.35, respectively.

4.2.1 Intermediate-Energy Coulomb Excitation of ^{38}S

The Doppler-corrected γ-ray spectrum for ^{38}S measured with CAESAR is provided in Figure 4.2 with a laboratory-frame scattering angle cut of 40 mrad applied. The low-energy region of the spectrum is dominated by bremsstrahlung, which is electromagnetic radiation produced by the acceleration of electrons from the target atoms due to interactions with the beam, and other beam-correlated background such as target breakup and reaction products interacting with the beampipe. The highest intensity peak corresponds to the known $2_1^+ \rightarrow 0_1^+$ transition in ^{38}S at 1292.0(2) keV [7]. The energy of the transition measured in this work is 1289(5) keV. The weak γ-ray peaks at 1513 keV and 2508 keV were included on the basis of γ-γ coincidence data. Furthermore, Doppler-corrected background from 1460-keV γ

rays emitted in the laboratory frame is clearly visible and was included in the fit.

The two-dimensional matrix for events where exactly two γ rays were detected with CAESAR within the coincidence time window is shown in Figure 4.3. In this plot, nearest-neighbor addback was employed and no scattering angle cut was applied in order to maximize statistics. As seen in the matrix, the 1292-keV and 1513-keV γ decays are in coincidence. In addition, events with both the 1292-keV and 2508-keV transitions are visible. The background-subtracted projection of this matrix gated on the 1292-keV peak is shown in Figure 4.4. The background subtraction was performed by gating on a projection of the same width as the 1292-keV gate but at higher energy and subtracting the resulting spectrum from the 1292-keV projection. This plot provides further evidence for the coincidence relationships inferred from the matrix. The 1513-keV peak has been observed previously and tentatively assigned as the $(2_2^+) \rightarrow 2_1^+$ transition [10, 48, 86–88]. The adopted energy for the transition is 1513(2) keV [7] and the energy measured here is 1512(9) keV. Its observation from intermediate-energy Coulomb excitation in this work confirms the 2_2^+ assignment. The uncertainty in energy was derived from the fit uncertainty added in quadrature with a systematic uncertainty of 4.5 keV [89]. The 2508(25)-keV transition from a level at 3800(25) keV has not been observed in previous works. The SDPF-MU interaction predicts that the 2_3^+ level in ^{38}S is at 3553 keV in excitation energy and decays with a relative branching ratios of 100% to the 2_1^+, 18% to the ground state and 18% to the 2_2^+ level. This is consistent with the 2508-1292 keV cascade from a 3800-keV level established here. Due to low statistics, any additional γ-decay branches from the 3800-keV state were not observed.

The nominal maximum safe scattering angle is 66 mrad in the center-of-mass frame or

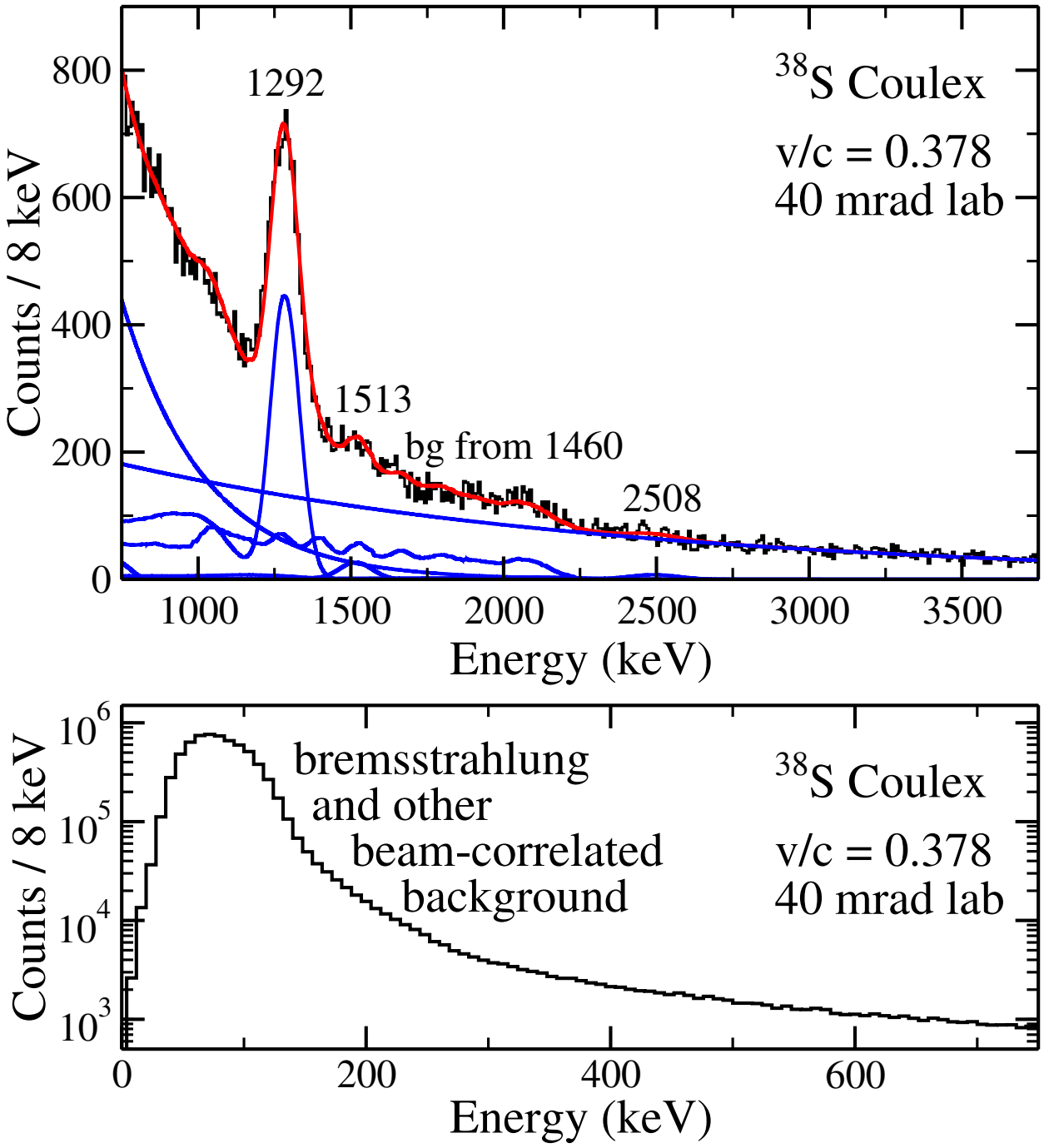

Figure 4.2: Top: Doppler-corrected energy spectrum for ^{38}S gated on scattering angles smaller than 40 mrad in the laboratory frame. The blue curves are the individual components of the fit function derived from GEANT4 simulations along with a double exponential background. The red curve is the total fit function. Bottom: Low-energy portion of the Doppler-corrected energy spectrum for ^{38}S. The large background at low energies is due to bremsstrahlung and other beam-correlated background.

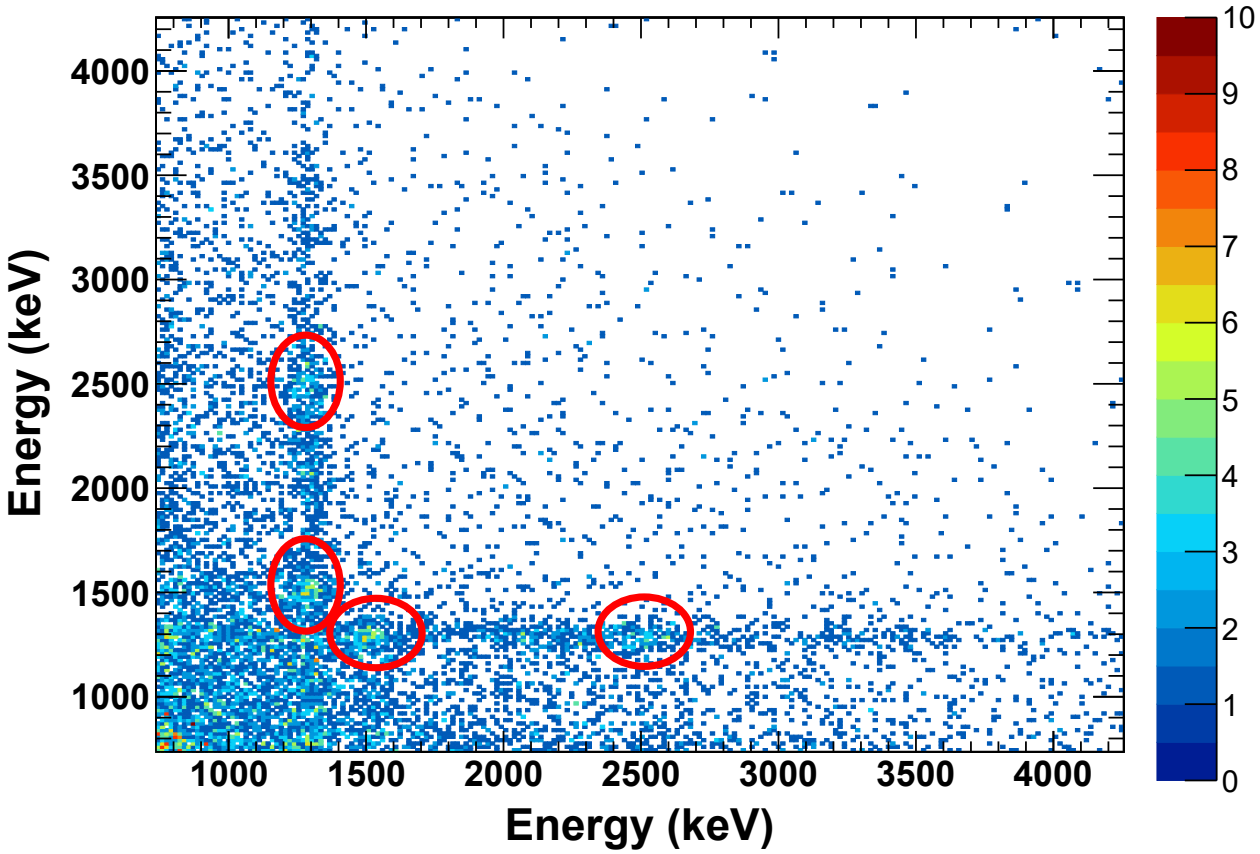

Figure 4.3: Doppler-corrected coincidence matrix for ^{38}S events with exactly two γ rays detected in CAESAR. Both the x and y axes have 16-keV wide bins. The matrix is filled symmetrically. The 1292-keV and 1513-keV transitions are in coincidence and the 1292-keV and 2508-keV transitions are in coincidence.

55 mrad in the laboratory frame. This corresponds to a minimum impact parameter of:

$$b_{min} = \left(1.2 \cdot (209)^{1/3} + 1.2 \cdot (38)^{1/3} + 2\right) \text{ fm} = 13.16 \text{ fm}, \tag{4.8}$$

using the touching spheres plus 2 fm approximation [57, 66]. The maximum center-of-mass maximum scattering angle θ_{max} was calculated from the minimum impact parameter b_{min} with the rescaling factor of Equation 2.11:

$$b_{min} = \frac{a_0}{\gamma} \cot\left(\frac{\theta_{max}}{2}\right) + \frac{\pi}{2}\frac{a_0}{\gamma}. \tag{4.9}$$

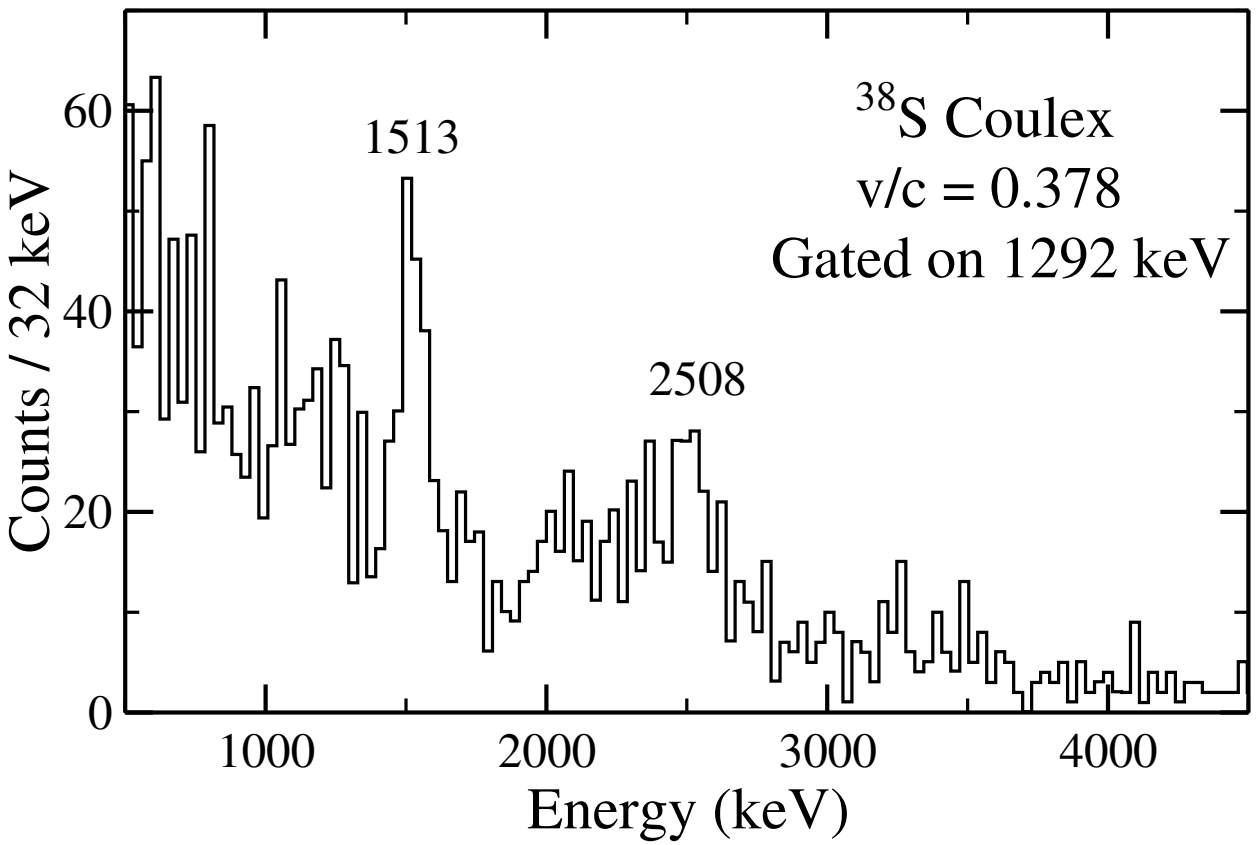

Figure 4.4: Background-subtracted, Doppler-corrected γ-ray spectrum for ^{38}S counts in coincidence with the 1292-keV transition. The 1513-keV and 2508-keV peaks are visible.

The maximum scattering angle was then converted from the center-of-mass frame to the laboratory frame using the relativistic kinematics calculator in LISE++ [72].

It is known that the angular emittance of the beam and angular straggling in the target can necessitate a more restrictive choice for the maximum scattering angle [81, 90]. Figure 4.5 shows the number of background-subtracted counts in the 1292-keV full-energy peak as a function of scattering angle in the laboratory frame. As shown here, the angle-integrated cross section would be underestimated for a scattering angle cut of 55 mrad. The angle-integrated cross section for the 1292-keV transition as a function of scattering angle cut is shown in the top panel Figure 4.6. Here, the cross section has been corrected for the feeding contributions of the 1513-keV and 2508-keV transitions. Furthermore, GEANT4

simulations were used to take into account the small changes in detection efficiency with choice of scattering angle cut due to the anisotropic angular distribution of the emitted γ rays. The corresponding $B(E2; 0_1^+ \rightarrow 2_1^+)$ strengths calculated using the semiclassical approach of Alder and Winther are shown in the bottom panel of Figure 4.6. Up until about 40 mrad, the extracted $B(E2; 0_1^+ \rightarrow 2_1^+)$ values are rather flat while for larger scattering angle cuts, some cross section is lost consistent with Figure 4.5.

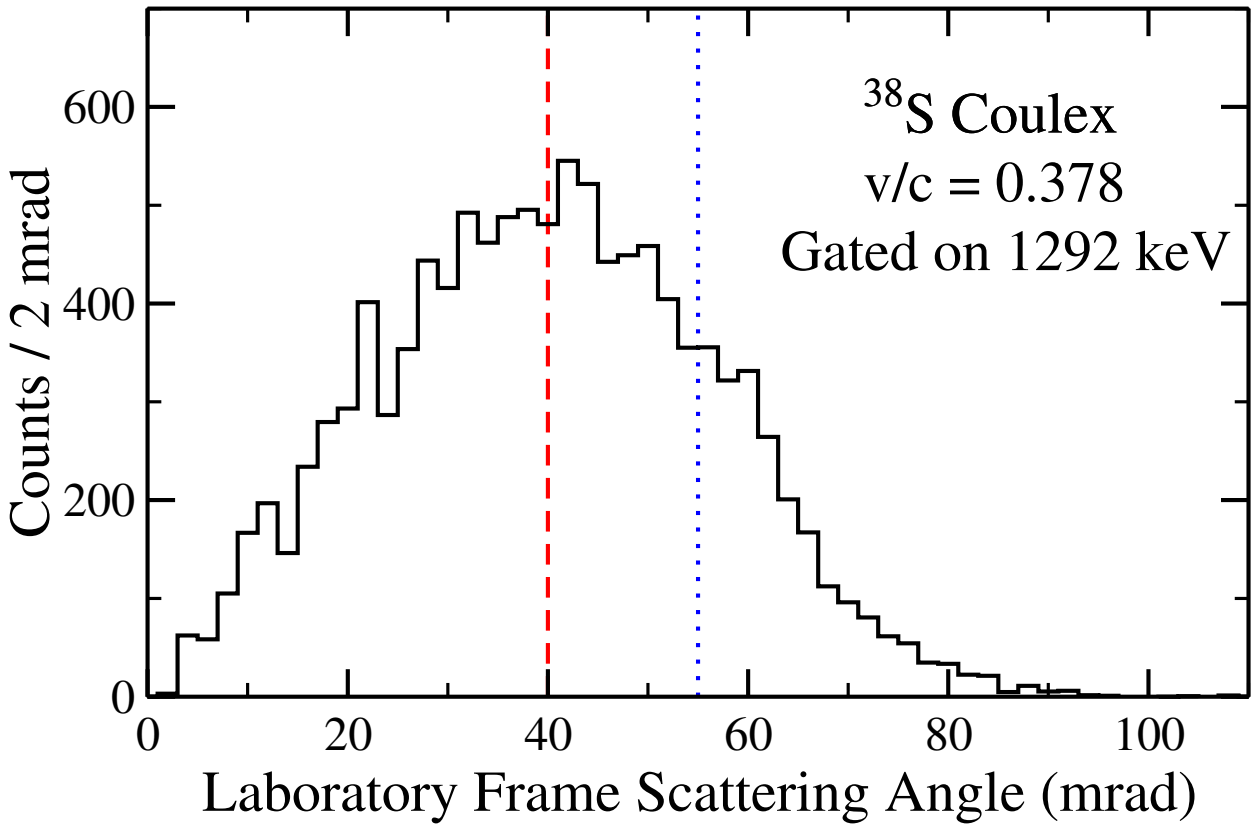

Figure 4.5: Counts in the 1292-keV peak as a function of scattering angle in the laboratory frame. Using the nominal safe scattering angle of 55 mrad would lead to an underestimation of the angle-integrated cross section. A maximum safe scattering angle of 40 mrad was considered in the analysis.

Using a maximum scattering angle of 40 mrad in the laboratory frame, the $B(E2; 0_1^+ \rightarrow 2_1^+)$ strength was determined to be 229(19) e^2fm^4. Similarly, the $B(E2; 0_1^+ \rightarrow 2_2^+)$ strength was found to be 21(8) e^2fm^4 and the $B(E2; 0_1^+ \rightarrow 2_3^+)$ strength was found to be 11(8) e^2fm^4

for the same maximum scattering angle. It should be noted that the 1513-keV $2_2^+ \rightarrow 2_1^+$ and 2508-keV $2_3^+ \rightarrow 2_1^+$ decays have contributions from both $M1$ and $E2$ multipoles. Since the multipole mixing ratio affects the angular distribution of the emitted γ rays, there is an effect on the detection efficiency of the array. The quoted $B(E2)$ strengths were extracted using the predicted multipole mixing ratios from the SDPF-MU interaction. From GEANT4 simulations of CAESAR for the 1513-keV $2_2^+ \rightarrow 2_1^+$ transition, the difference in efficiency using the angular distribution predicted from the shell-model multipole mixing ratio compared to assuming a pure $E2$ transition is about 0.1%. The SDPF-MU multipole mixing ratios were used to determine the angular distributions for all mixed transitions in this work.

The literature value for the $B(E2; 0_1^+ \rightarrow 2_1^+)$ strength from the previous intermediate-energy Coulomb excitation experiment by Scheit *et al.* is 235(30) e^2fm^4 [28]. The 1513-keV and 2508-keV feeding transitions were not observed by Scheit *et al.* due to limited statistics. If feeding is neglected in this analysis, the extracted $B(E2; 0_1^+ \rightarrow 2_1^+)$ strength is 261 e^2fm^4, which is also consistent with the previous value [28].

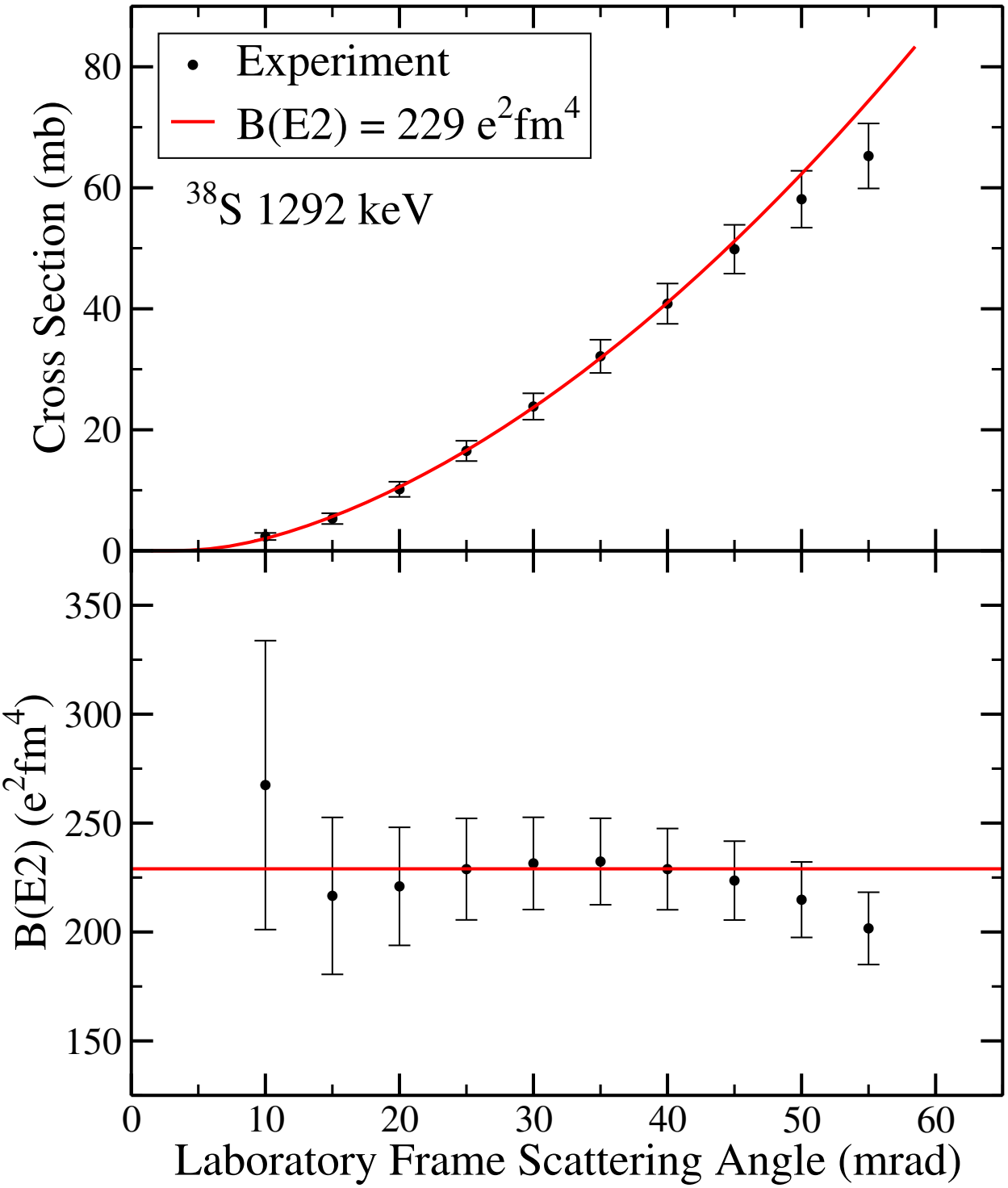

Figure 4.6: Top: feeding-subtracted angle-integrated cross section as a function of choice of scattering angle cut derived from the experimental data for the 2_1^+ state in ^{38}S (black). The red curve is the expected cross section assuming a $B(E2; 0_1^+ \rightarrow 2_1^+)$ strength of 229 e^{2}fm^4. Bottom: $B(E2; 0_1^+ \rightarrow 2_1^+)$ strength calculated using Alder-Winther theory for different choices of maximum scattering angle.

4.2.2 Intermediate-Energy Coulomb Excitation of ^{40}S

The Doppler-corrected γ-ray spectrum for ^{40}S measured with CAESAR is shown in Figure 4.7. Here, a laboratory-frame scattering angle cut of 40 mrad has been applied. The known $2_1^+ \rightarrow 0_1^+$ transition in ^{40}S at 903.68(9) keV [7] is clearly visible. The energy of the transition measured in this work is 902(5) keV. In addition, there is a weak transition at 2452(23) keV. The 2452-keV transition is more clearly observed in the two-dimensional γ-γ coincidence matrix shown in Figure 4.8. As for ^{38}S, nearest-neighbor addback was utilized and no scattering angle cut was applied for this plot to maximize statistics. Figure 4.9 shows that the 2452-keV peak is also clearly seen in the background-subtracted projection of the coincidence matrix gated on the 904-keV transition. From this coincidence relationship, the 2452(23)-keV transition is inferred to originate from a level at 3356(23) keV.

The angle-integrated cross section for the 904-keV transition, corrected for feeding by the 2452-keV transition, is shown in the top panel Figure 4.6 as a function of scattering angle cut. The nominal maximum scattering angle in the laboratory frame from the touching spheres plus 2 fm approximation is 51 mrad. The bottom panel shows the corresponding $B(E2; 0_1^+ \rightarrow 2_1^+)$ values. The $B(E2; 0_1^+ \rightarrow 2_1^+)$ strength adopted in this work is 284(26) e^2fm^4 using the more conservative 30 mrad laboratory-frame scattering angle cut. Angle cuts beyond 30 mrad begin to yield smaller $B(E2; 0_1^+ \rightarrow 2_1^+)$ values due to angular emittance of the beam and angular straggling in the reaction target. The value for the $B(E2; 0_1^+ \rightarrow 2_1^+)$ strength reported by Scheit *et al.* from intermediate-energy Coulomb excitation experiment, in which no feeding was observed due to limited statistics, is 334(36) e^2fm^4 [28]. If feeding from the 2452-keV transition is neglected in this work, the extracted $B(E2; 0_1^+ \rightarrow 2_1^+)$ strength is 305 e^2fm^4, which is consistent with the previous measurement within uncertainties.

SDPF-MU shell-model calculations for ^{40}S predict that the 2_2^+ level is at 3285 keV and that the 2_3^+ state is at 3579 keV. The 2_2^+ state in the calculation decays nearly 100% of the time to the 2_1^+ level. Similarly, the 2_3^+ state decays with a relative 100% branch to the 2_1^+ level and an 8% branch to the ground state. However, the predicted $B(E2; 0_1^+ \rightarrow 2_2^+)$ strength is only 2.9 e^{2}fm^4 compared to 54 e^{2}fm^4 for the $B(E2; 0_1^+ \rightarrow 2_3^+)$ strength. The experimental $B(E2; 0_1^+ \rightarrow 2_x^+)$ strength for the 3356(23)-keV state calculated from the yield of the 2452-keV transition in this work is 26(17) e^{2}fm^4 using the 30 mrad scattering angle cut. No higher-lying 2^+ states beyond the first 2^+ are listed in the current data evaluation [7].

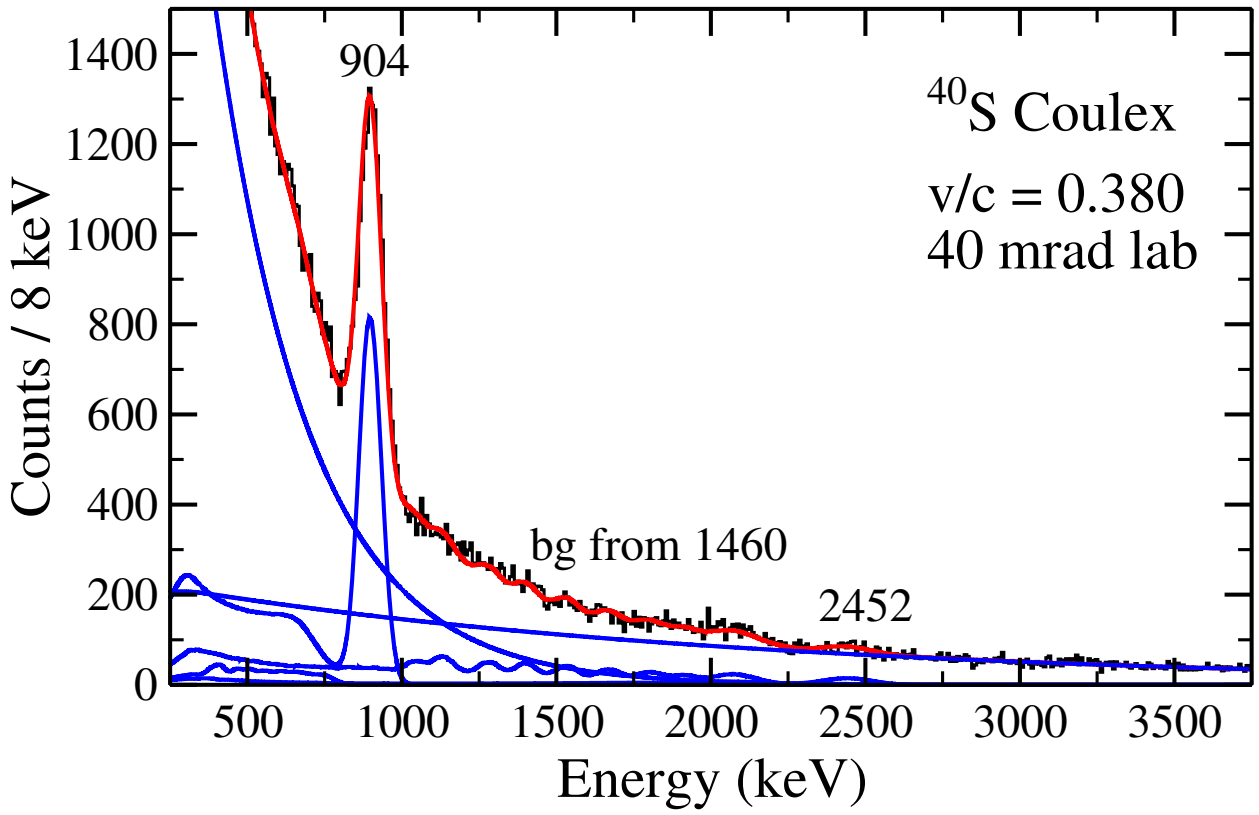

Figure 4.7: Doppler-corrected energy spectrum for ^{40}S gated on scattering angles smaller than 40 mrad in the laboratory frame. The blue curves are the individual components of the fit function derived from GEANT4 simulations along with a double exponential background. The red curve is the total fit function.

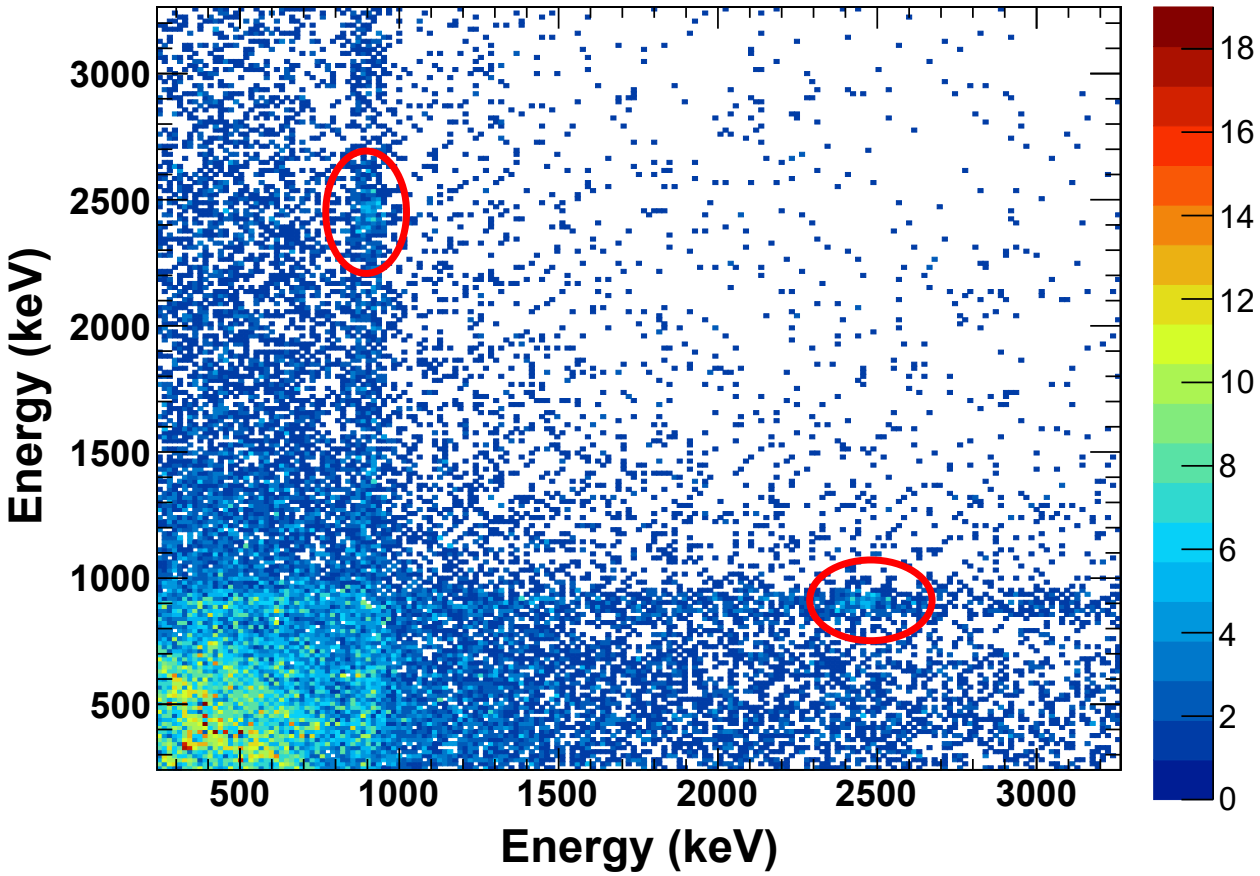

Figure 4.8: Doppler-corrected coincidence matrix for ^{40}S events with exactly two γ rays detected in CAESAR. Both the x and y axes have 16-keV wide bins. The matrix is filled symmetrically. The 904-keV and 2452-keV transitions are in coincidence.

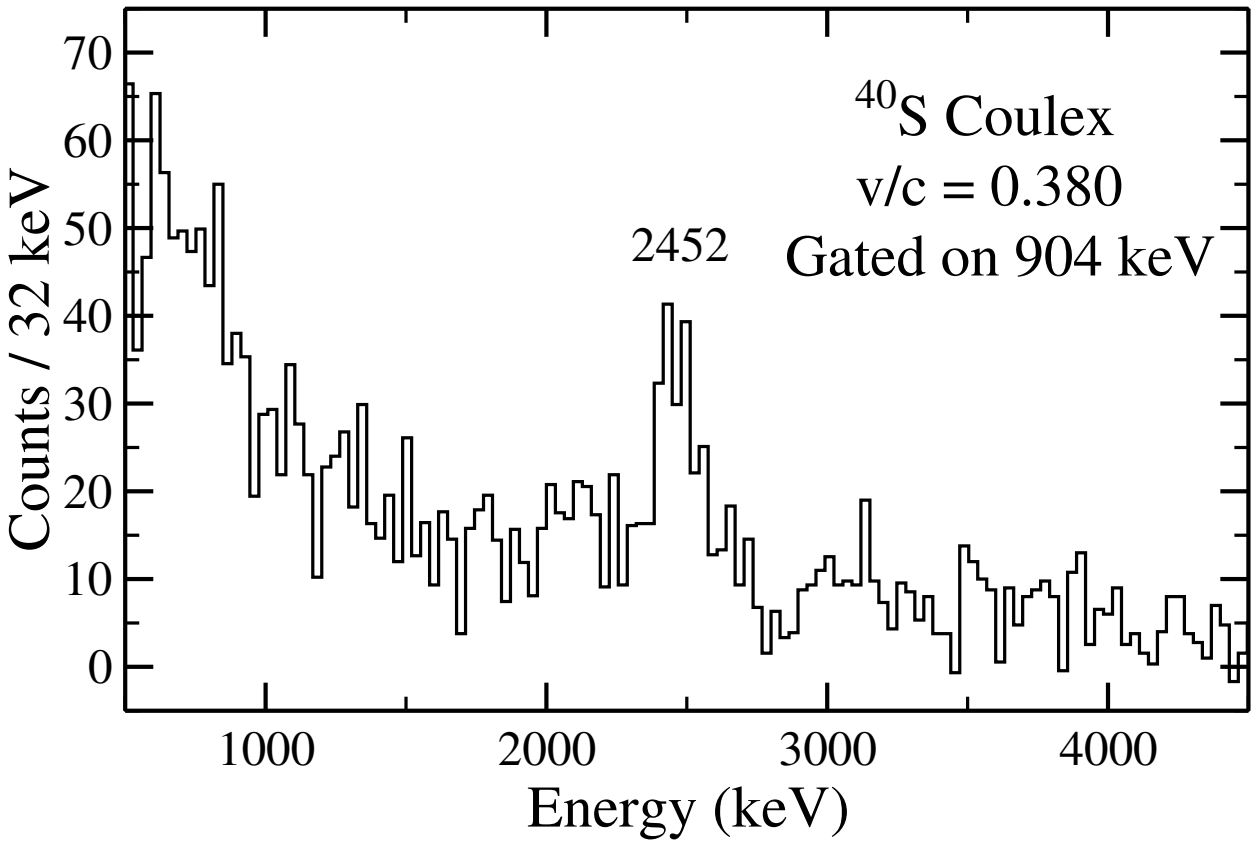

Figure 4.9: Background-subtracted, Doppler-corrected γ-ray spectrum for ^{40}S counts in coincidence with the 904-keV transition. A peak at 2452 keV is visible.

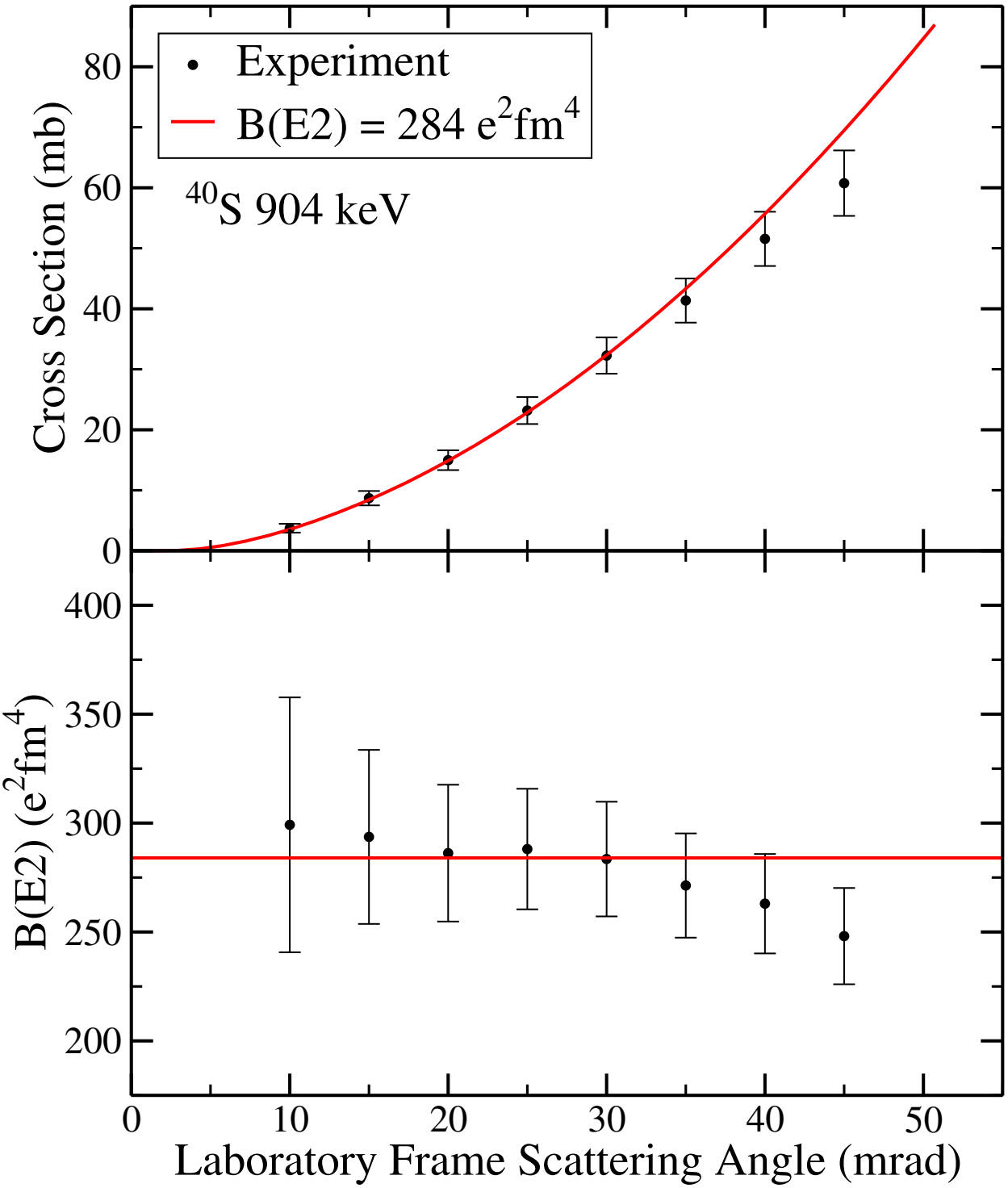

Figure 4.10: Top: feeding-subtracted angle-integrated cross section as a function of choice of scattering angle cut derived from the experimental data for the 2_1^+ state in ^{40}S (black). The red curve is the expected cross section assuming a $B(E2; 0_1^+ \rightarrow 2_1^+)$ strength of 284 e^{2}fm^4. Bottom: $B(E2; 0_1^+ \rightarrow 2_1^+)$ strength calculated using Alder-Winther theory for different choices of maximum scattering angle.

4.2.3 Intermediate-Energy Coulomb Excitation of ^{42}S

Figure 4.11 shows the non-addback Doppler-corrected γ-ray spectrum for ^{42}S measured with CAESAR using a scattering angle cut of 40 mrad in the laboratory frame. An intense peak corresponding to the $2_1^+ \rightarrow 0_1^+$ transition reported at 903(5) keV [7] is clearly visible. The energy of the transition extracted from the fit performed in this experiment is 904(5) keV.

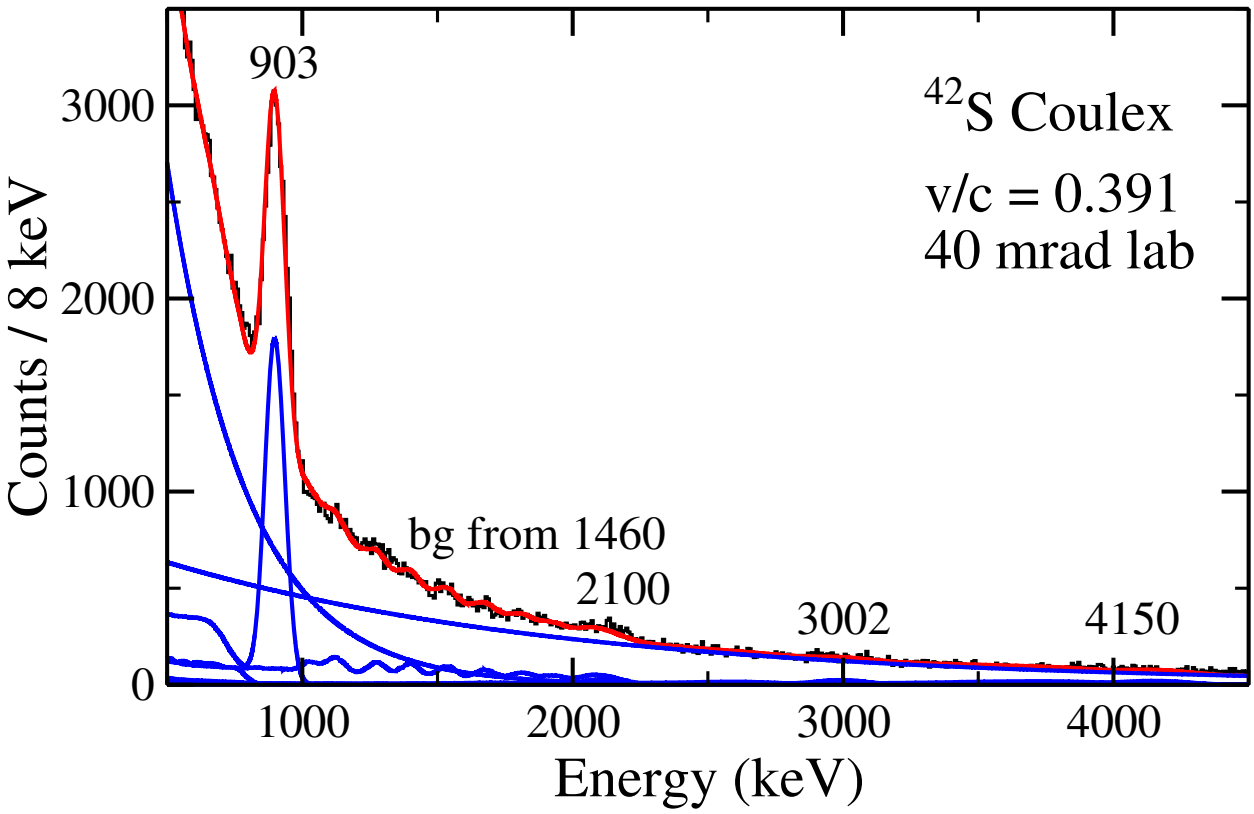

Figure 4.11: Doppler-corrected energy spectrum for ^{42}S gated on scattering angles smaller than 40 mrad in the laboratory frame. The blue curves are the individual components of the fit function derived from GEANT4 simulations along with a double exponential background. The red curve is the total fit function.

Lunderberg *et al.* observed a 3002(4) keV γ ray in ^{42}S and tentatively associated this transition with the decay from the (2_2^+) state to the ground state [10]. This weak transition can be seen at 3005(13) keV in the nearest-neighbor addback spectrum gated on multiplicity 1 events shown in Figure 4.12. For an array like CAESAR covering nearly the full solid angle,

the relative enhancement of the 3002-keV peak for events where only one γ ray was detected (a so-called multiplicity one event) compared to all events is indicative of a direct transition to ground state. The observation of the 3002-keV transition in intermediate-energy Coulomb excitation in this work confirms the assignment by Lunderberg *et al.* rather than the proposal for the (2_2^+) level lying at 2779 keV and decaying predominantly to the 2_1^+ state put forth by Sohler *et al.* [91].

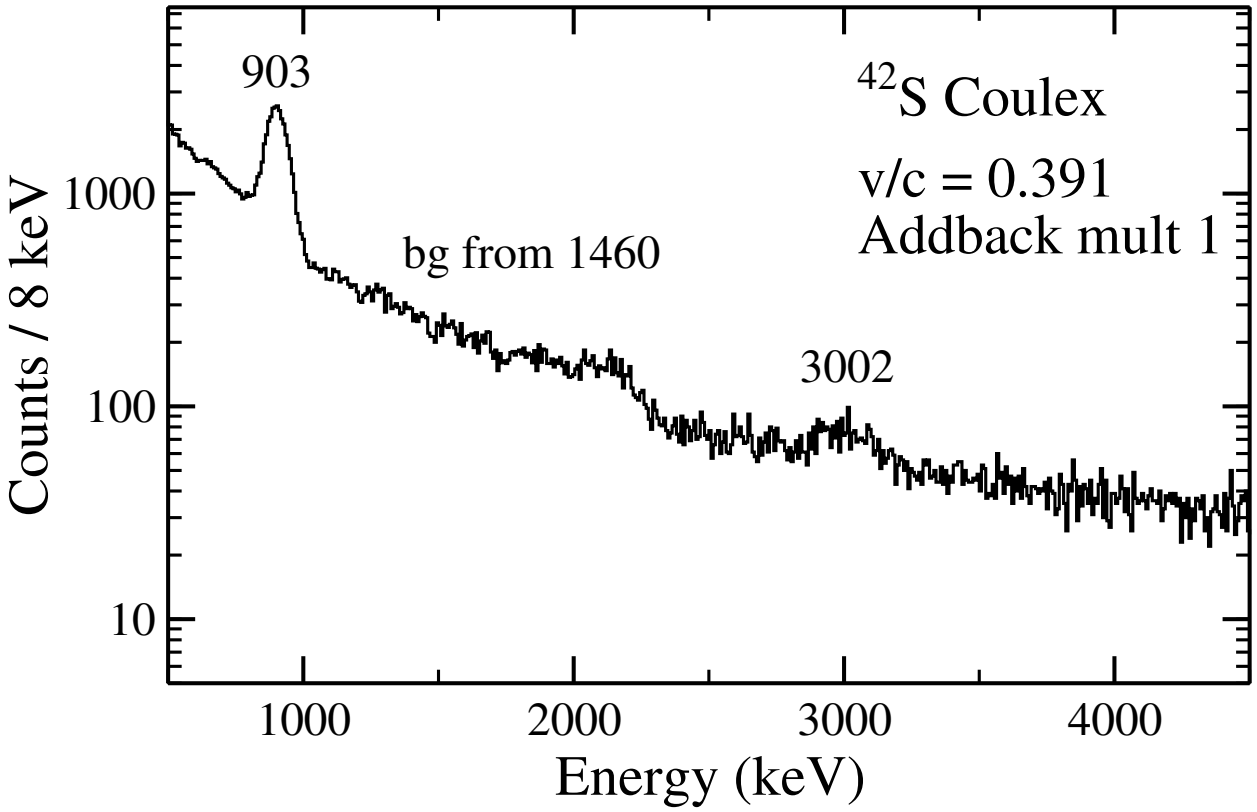

Figure 4.12: Doppler-corrected energy spectrum for ^{42}S for events where only one γ ray was detected by CAESAR. Nearest-neighbor addback was utilized. The 3000-keV transition from the 2_2^+ state to the ground state is visible.

From [10], the 3002-keV level has relative decay branches of 100(2)% to the ground state and 18(2)% to the 2_1^+ state via a 2100(4)-keV γ-ray transition. The 2100-keV transition can be seen in the two-dimensional γ-γ coincidence matrix shown in Figure 4.13, along with

a broad feature around 4150(110) keV. The projection of this matrix gated on the 903-keV peak is provided in Figure 4.14, showing the same peaks. The energy of the 2100-keV transition measured in this work is 2117(31) keV, consistent with the more precise value of 2100(4) keV from [10]. Due to the feature from Doppler-corrected 1460-keV background, the relative intensities of the 3002-keV and 2100-keV transitions were fixed to the known efficiency-corrected branching ratio from [10] in the fit of Figure 4.11 and in the similar fits performed using different scattering angle cuts.

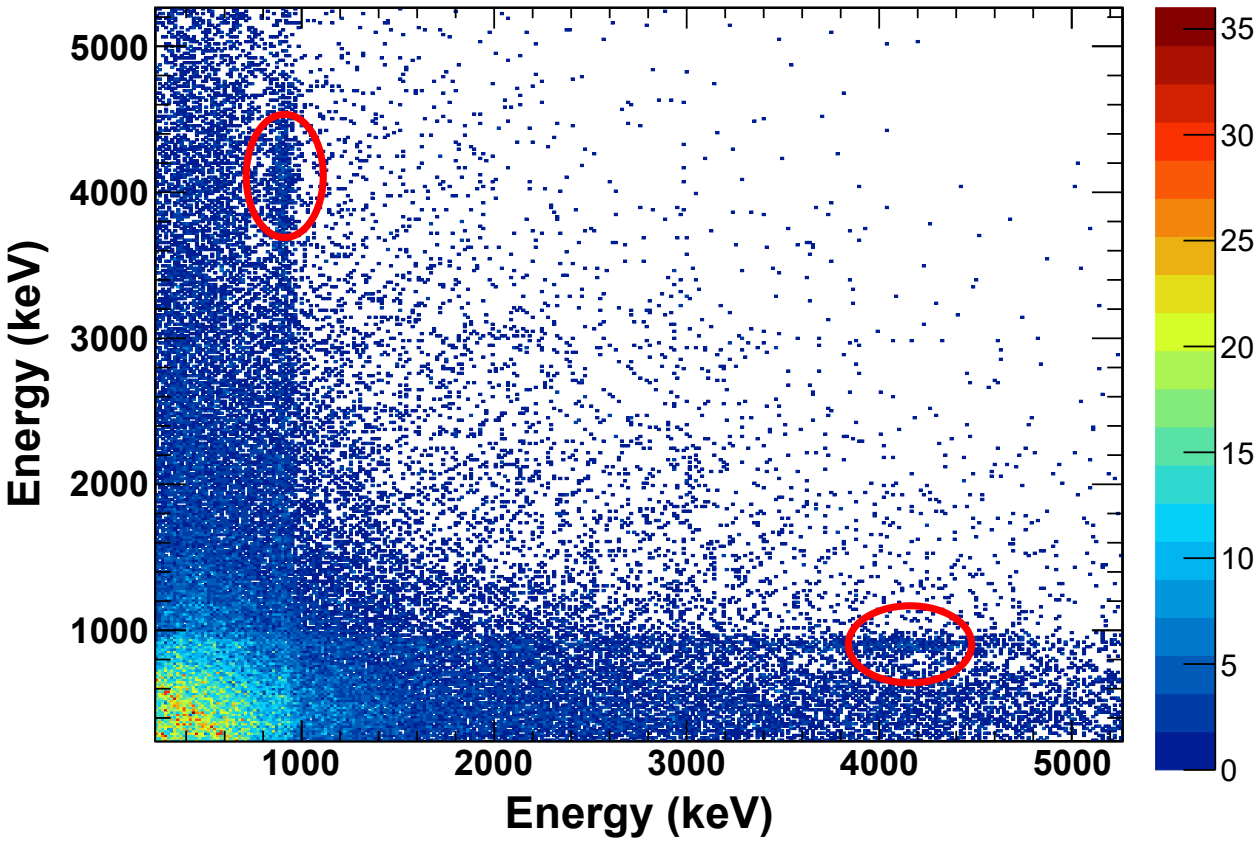

Figure 4.13: Doppler-corrected coincidence matrix for ^{42}S events with exactly two γ rays detected in CAESAR. Both the x and y axes have 16-keV wide bins. The matrix is filled symmetrically. The 903-keV transition is in coincidence with peaks at 2100 keV (more clearly observed in the projection of Figure 4.14) and 4150 keV.

Figure 4.15 shows the angle-integrated cross section for the 903-keV transition as a function of scattering angle cut. The cross sections have been corrected for feeding from the

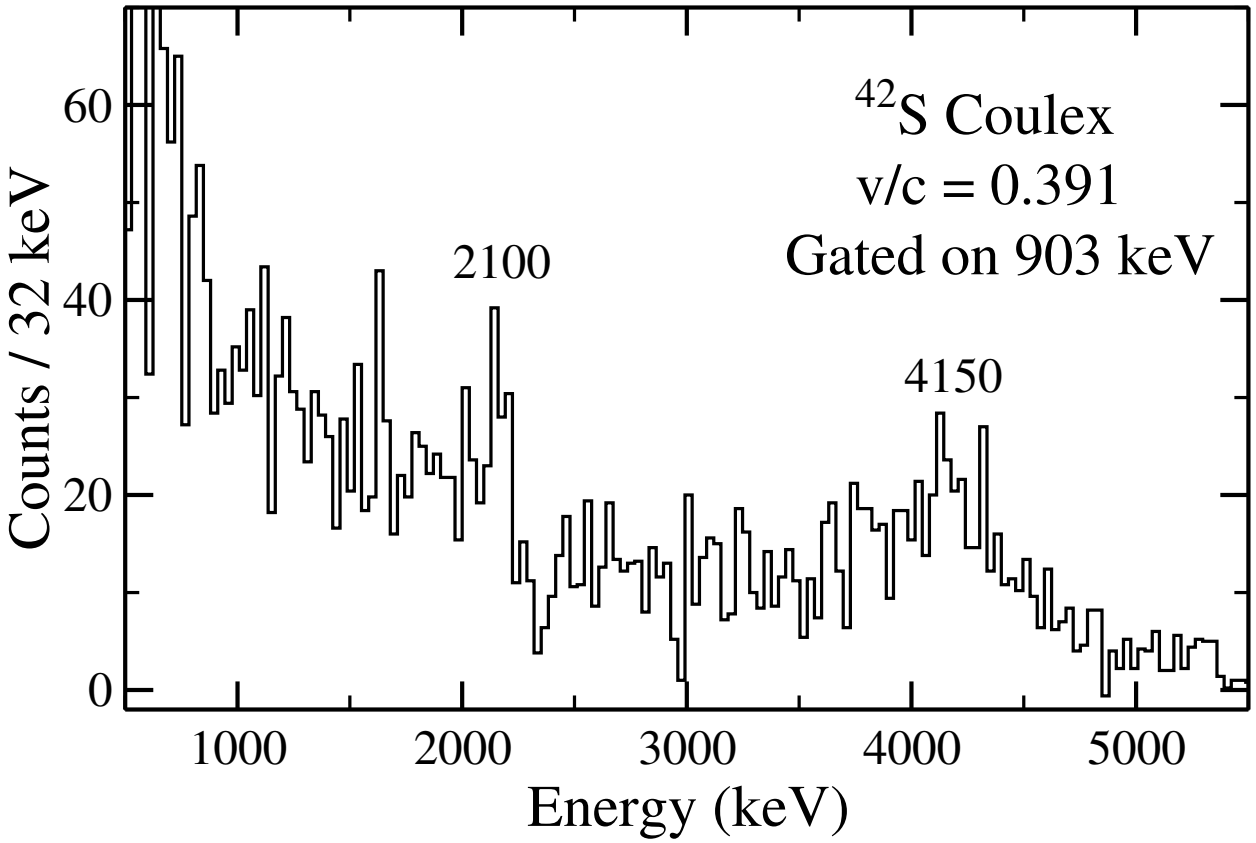

Figure 4.14: Background-subtracted, Doppler-corrected γ-ray spectrum for ^{42}S counts in coincidence with the 903-keV transition.

2100-keV and 4150-keV transitions. Unlike for ^{38}S and ^{40}S, this plot shows a clear and significant dependence of extracted $B(E2; 0_1^+ \rightarrow 2_1^+)$ strength on laboratory-frame scattering angle cut for all choices of maximum scattering angle. A method similar in principle to the CRDC scaling method introduced in [92, 93] was developed to correct this dependence. The shape of the theoretical cross section curve as a function of maximum scattering angle is fixed by the A and Z of the target and projectile, multipolarity of the transition, energy of the state being excited, and velocity of the beam at mid-target. Therefore, the experimental cross section curve should have the same shape over the range of scattering angles smaller than the scattering angle at which the angular straggling begins to affect the data, as seen in Figure 4.6 for ^{38}S and Figure 4.10 for ^{40}S. The $B(E2; 0_1^+ \rightarrow 2_1^+)$ strength is propor-

tional to the scaling factor of the curve. The theoretical cross section was parameterized as $a_t\theta^2 + b_t\theta + c_t$ where θ is the maximum scattering angle. Similarly, the experimental data were parameterized as $a_e\theta^2 + b_e\theta + c_e$ for experimental laboratory-frame scattering angles from 10 mrad to 35 mrad. A quadratic correction factor was then applied to the experimental scattering angles where the value of this factor was chosen to minimize $(a_t/b_t - a_e/b_e)^2$. Since the minimization is based on the ratios a_t/b_t and a_e/b_e, the shape of the experimental curve is adjusted to match the shape of the theoretical curve without matching the absolute scaling. Therefore, the $B(E2; 0_1^+ \rightarrow 2_1^+)$ strength is not assumed beforehand in the correction procedure. The best fit scaling factor for the theoretical curve after correcting the experimental data corresponds to a $B(E2; 0_1^+ \rightarrow 2_1^+)$ strength of 326 e^2fm^4.

The ^{42}S data were taken in two separate sets of beam time, one in the middle of the experiment and one at the end of the experiment. The data from the first set and the second set show the same correlation between $B(E2; 0_1^+ \rightarrow 2_2^+)$ strength and laboratory scattering angle shown in Figure 4.15. For example, the cross sections found for the 40 mrad laboratory-frame scattering angle cut from the first and second data sets are 48.4 mb and 48.2 mb, respectively. The experimental data for each of the neutron-rich sulfur isotopes was taken in the following order: ^{38}S, ^{40}S, ^{42}S (first half), ^{43}S, ^{44}S, and ^{42}S (second half). As seen in Section 4.3 and the following subsection, the ^{43}S and ^{44}S data do not clearly show the same correlation between choice of scattering angle cut and $B(E2; 0_1^+ \rightarrow 2_2^+)$ strength observed for ^{42}S. Therefore, the issue did not appear at a certain time and persist for the remainder of the experiment. Based on this, it is hypothesized that the problem is with the scattering-angle reconstruction on an incoming beam basis rather than a scattering-angle-dependent loss in γ-ray detection efficiency.

The $B(E2; 0_1^+ \rightarrow 2_1^+)$ in ^{42}S measured in intermediate-energy Coulomb excitation by

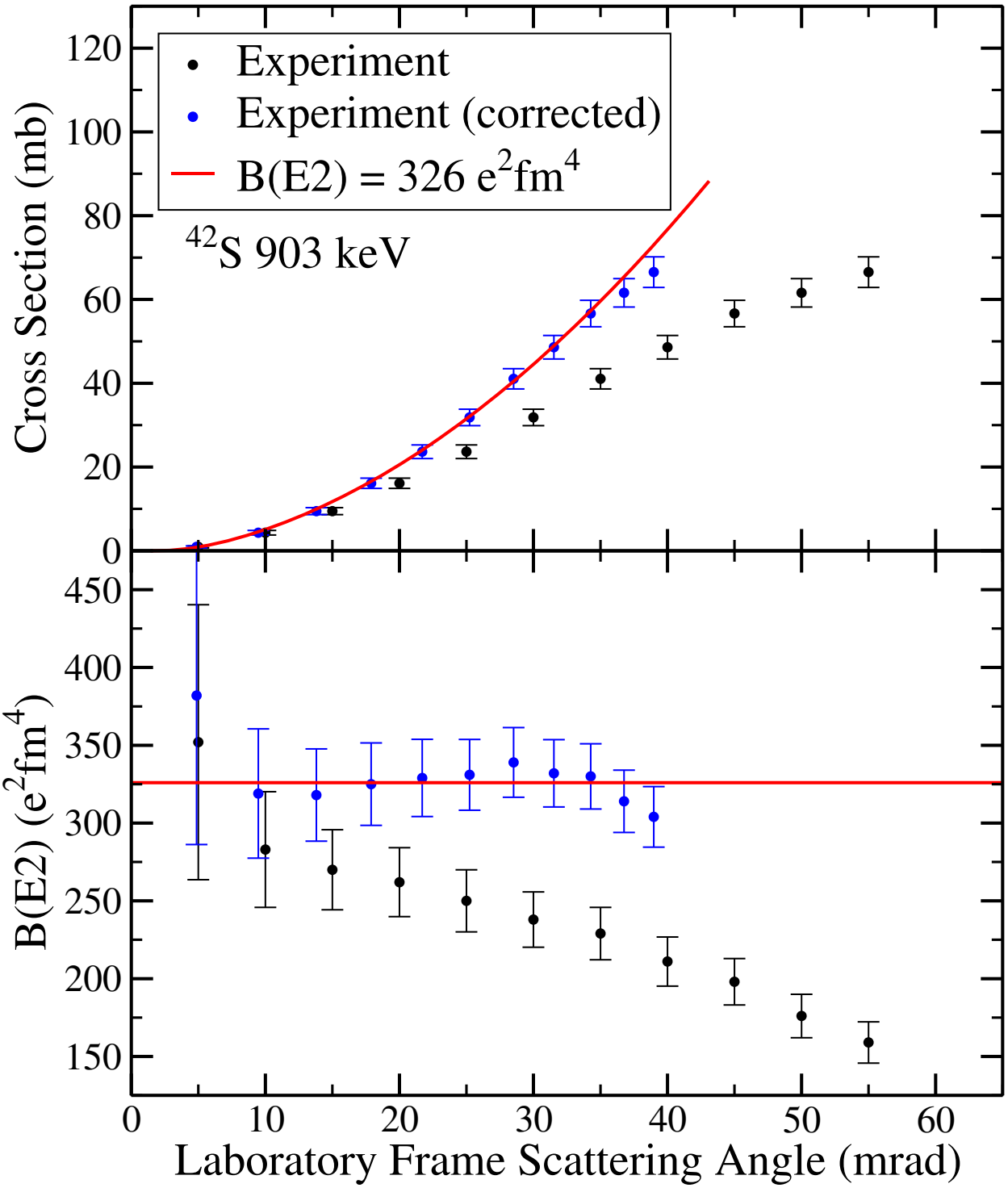

Figure 4.15: Top: feeding-subtracted angle-integrated cross section as a function of choice of scattering angle cut derived from the experimental data for the 2_1^+ state in ^{42}S (black). The red curve is the expected cross section assuming a $B(E2; 0_1^+ \rightarrow 2_1^+)$ strength of 326 e^{2}fm^4. The blue data points are the experimental data with the correction for scattering angle explained in the text. Bottom: $B(E2; 0_1^+ \rightarrow 2_1^+)$ strength calculated using Alder-Winther theory for different choices of maximum scattering angle.

Scheit *et al.* was 397(63) e^2fm^4 [28]. The lifetime of the 2_1^+ state in ^{42}S has also been measured using the recoil-distance method to be 20.6(15) ps [45] and $21.5^{+1.1}_{-0.9}$ ps [53]. Using Equation 2.34, Equation 1.18, and an excitation energy of 903(5) keV, the corresponding $B(E2; 0_1^+ \rightarrow 2_1^+)$ strengths are 329(26) e^2fm^4 from [45] and 315^{+18}_{-16} e^2fm^4 from [53]. The value of 326 e^2fm^4 found after applying the correction to the scattering angle is in good agreement with these previous measurements. The uncertainty in the extracted $B(E2; 0_1^+ \rightarrow 2_1^+)$ strength was estimated by varying the number of experimental data points included in the fit and using both linear and quadratic correction factors. Including an additional 10% systematic uncertainty, the adopted value is 326(48) e^2fm^4.

The Coulomb excitation cross section to the 3002-keV state was found using the 35 mrad laboratory-frame scattering angle cut from the yields of the detected 2100-keV and 3002-keV de-excitation γ rays. The $B(E2; 0_1^+ \rightarrow 2_2^+)$ strength was calculated using the same corrected scattering angle used to extract the adopted result for the $B(E2; 0_1^+ \rightarrow 2_1^+)$ strength to be 27(14) e^2fm^4. SDPF-MU shell-model calculations predict a $B(E2; 0_1^+ \rightarrow 2_5^+)$ strength of 16 e^2fm^4 for the level at 5003 keV. The predicted reduced transition strengths to the 2_3^+ and 2_4^+ states are less than 0.001 e^2fm^4 and about 4 e^2fm^4, respectively. The 2_4^+ level at 4924 keV decays with a relative branching ratios of 100% to the ground state and 54% branching ratio to the 2_1^+ state (with smaller branching ratios to other states) while the 2_5^+ level decays with relative branching ratios of 100% to the 2_1^+ state and 11% to the ground state in the calculation. Employing the same method used for the 3002-keV level, the reduced transition strength to the level at 5053(110) keV that decays via a 4150(110)-keV γ ray to the 903-keV 2_1^+ state was calculated to be 11(9) e^2fm^4 assuming an $E2$ excitation from the data using the 35 mrad scattering angle cut. Lunderberg *et al.* report γ-ray transitions at 4102(8) keV and 4266(7) keV that were not placed in the level scheme [10]. Due to its large energy

uncertainty, the 4150(110)-keV feature may correspond to one or a combination of these transitions.

4.2.4 Intermediate-Energy Coulomb Excitation of ^{44}S

The Doppler-corrected γ-ray spectrum for ^{44}S measured with CAESAR using a laboratory-frame scattering angle cut of 40 mrad is shown in Figure 4.16. The previously-observed 1329.0(5)-keV γ ray corresponds to the $2_1^+ \rightarrow 0_1^+$ transition [49]. Other works report the energy of this transition as 1297(18) keV [29], 1350(10) keV [91], 1319(7) keV [44], 1321(10) keV [94], and 1320(8) keV [95]. The energy of the transition measured in this work is 1324(6) keV. The 949(5)-keV $2_3^+ \rightarrow 2_1^+$ transition reported in the literature [7] is more clearly observed in the two-dimensional γ-γ coincidence matrix for events with exactly two detected γ rays shown in Figure 4.17. The background-subtracted projection of this matrix gated on the 1329-keV peak is shown in Figure 4.18. The energy for the $2_3^+ \rightarrow 2_1^+$ transition measured in this work is 941(19) keV. This transition has also been reported recently at an energy of 954(4) keV [96]. SDPF-MU predicts that the 2_3^+ state decays with relative branching ratios of 100% to the 2_1^+ level and 14% to the ground state. Due to low statistics, the possible ground state branch was not observed in this experiment or in previous works. The 2150(11)-keV transition reported in the literature is tentatively assigned as the γ decay of the 2_2^+ state to the ground state [44, 45]. Due to the Doppler-corrected 1460-keV laboratory-frame background, the possible presence of this transition in this work is not well constrained.

The angle-integrated cross section for the 1329-keV transition, corrected for feeding by the 949-keV transition, is shown in the top panel Figure 4.19 as a function of the choice of maximum scattering angle. As seen in the bottom panel of Figure 4.19, the correspond-

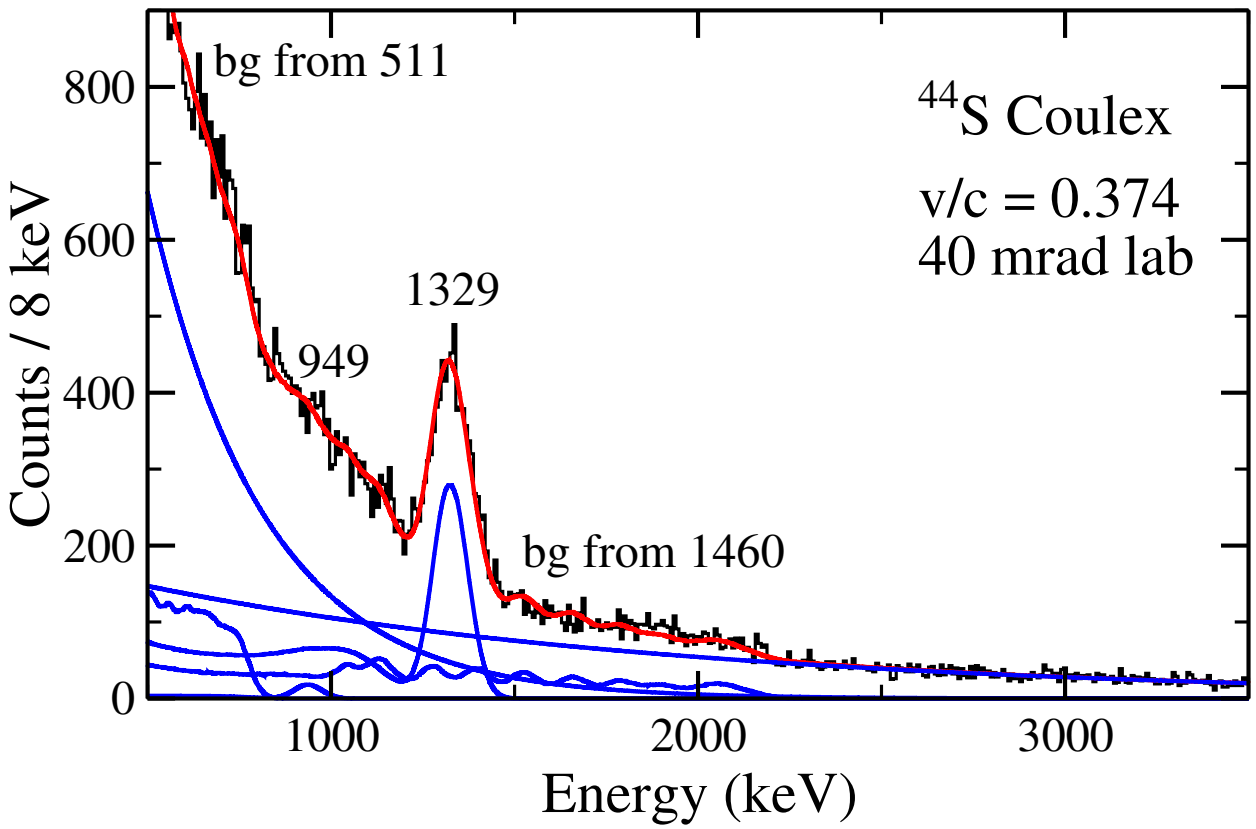

Figure 4.16: Doppler-corrected energy spectrum for ^{44}S gated on scattering angles smaller than 40 mrad in the laboratory frame. The blue curves are the individual components of the fit function derived from GEANT4 simulations along with a double exponential background. The red curve is the total fit function.

ing $B(E2; 0_1^+ \rightarrow 2_1^+)$ strength does not decrease with scattering angle cut with the same large slope observed for ^{42}S. The $B(E2; 0_1^+ \rightarrow 2_1^+)$ strength extracted using the 35 mrad laboratory-frame scattering angle cut is 221(28) e^{2}fm^4. The nominal maximum scattering angle in the laboratory frame from the touching spheres plus 2 fm approximation is 48 mrad. Using the same angle cut and the yield of the 949-keV $2_3^+ \rightarrow 2_1^+$ transition, the $B(E2; 0_1^+ \rightarrow 2_3^+)$ strength was determined to be 10(6) e^{2}fm^4.

The $B(E2; 0_1^+ \rightarrow 2_1^+)$ strength reported from intermediate-energy Coulomb excitation by Glasmacher *et al.* is 314(88) e^{2}fm^4 [29] which overlaps with the value in this work of 221(28) e^{2}fm^4 within mutual uncertainties. No feeding transitions were observed in the

work of Glasmacher *et al.* [29]. If feeding is neglected in this work, the $B(E2; 0_1^+ \rightarrow 2_1^+)$ value increases to 231 e^2fm^4, slightly improving the agreement.

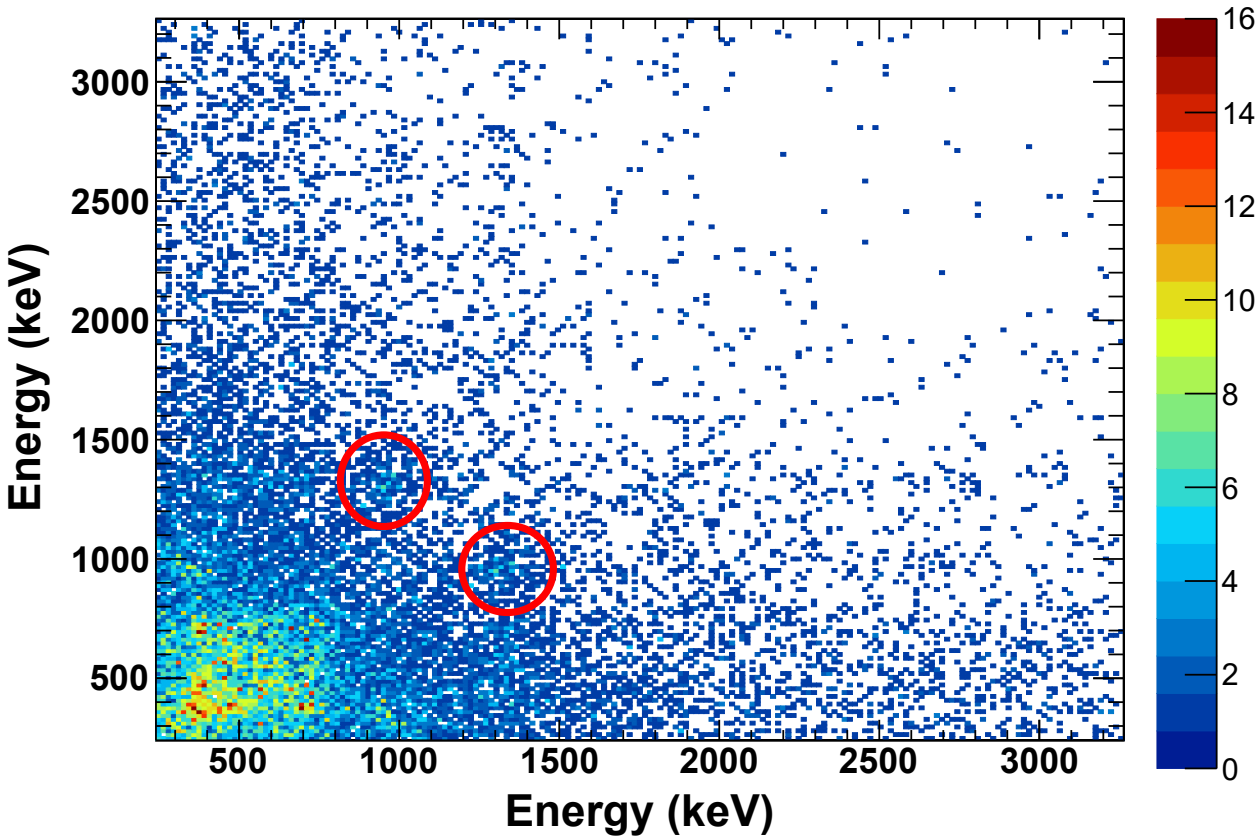

Figure 4.17: Doppler-corrected coincidence matrix for ^{44}S events with exactly two γ rays detected in CAESAR. Both the x and y axes have 16-keV wide bins. The matrix is filled symmetrically. The 1329-keV transition is in coincidence with the 949-keV transition.

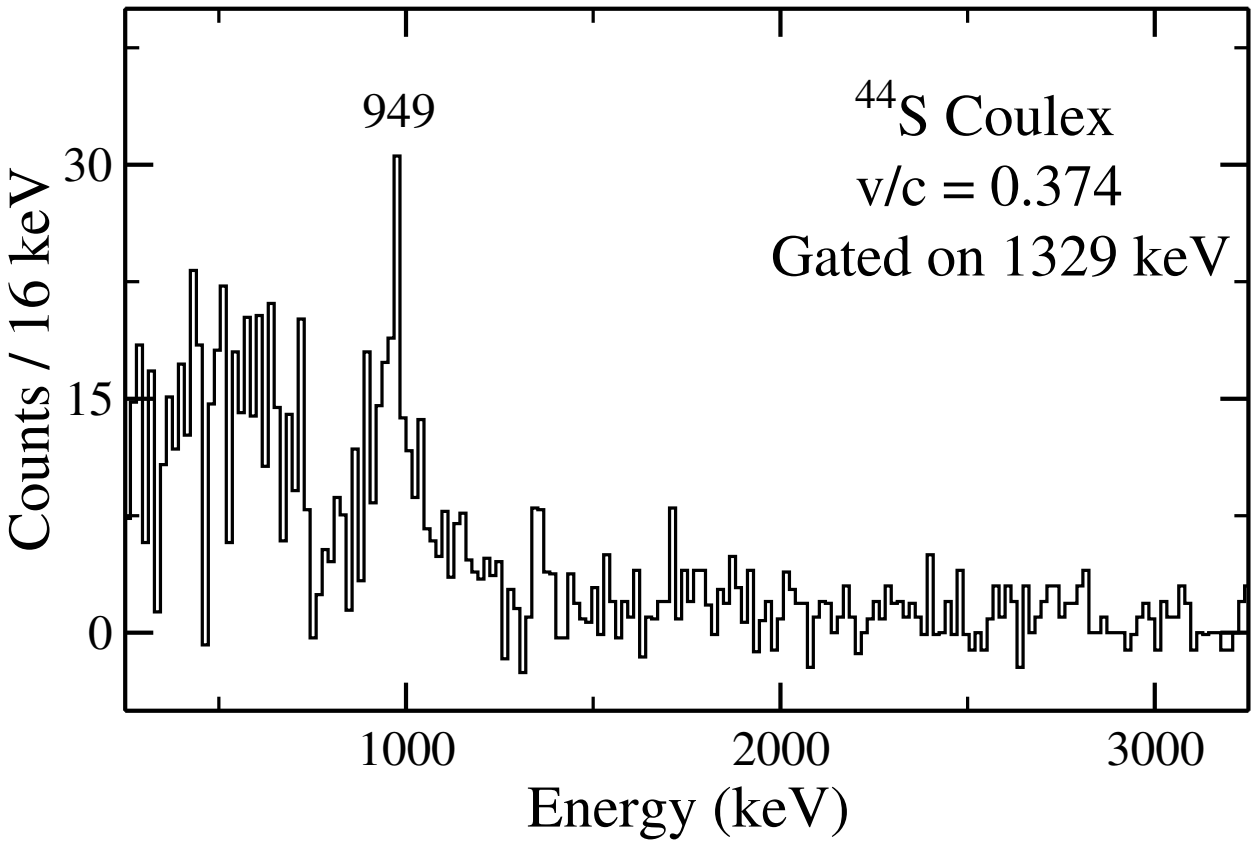

Figure 4.18: Background-subtracted, Doppler-corrected γ-ray spectrum for ^{44}S counts in coincidence with the 1329-keV transition.

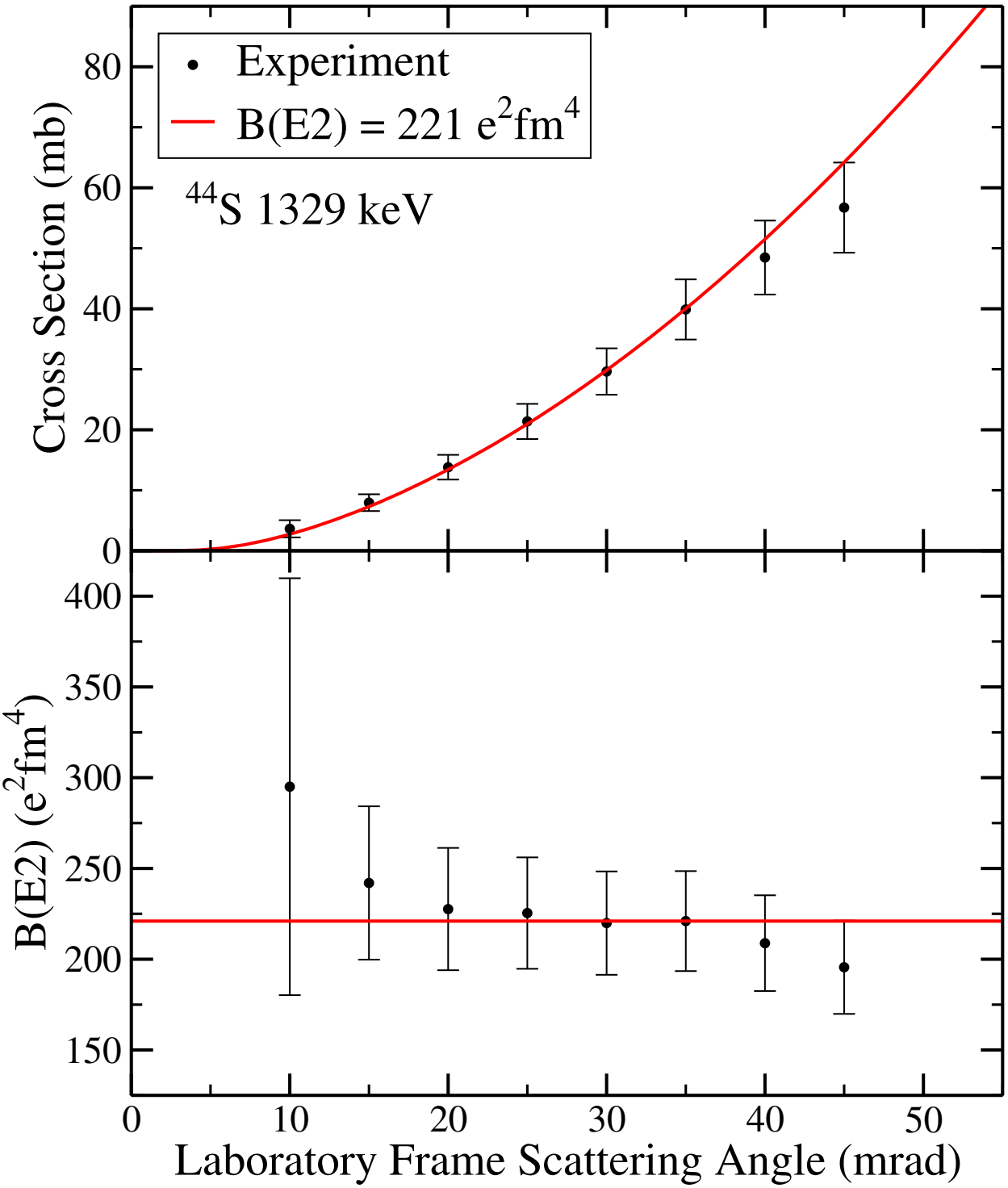

Figure 4.19: Top: feeding-subtracted angle-integrated cross section as a function of choice of scattering angle cut derived from the experimental data for the 2_1^+ state in ^{44}S (black). The red curve is the expected cross section assuming a $B(E2; 0_1^+ \rightarrow 2_1^+)$ strength of 221 e^{2}fm^4. Bottom: $B(E2; 0_1^+ \rightarrow 2_1^+)$ strength calculated using Alder-Winther theory for different choices of maximum scattering angle.

4.3 Results for ^{43}S

4.3.1 ^{43}S Incoming Beam Isomeric Content

The production of the ^{43}S secondary beam at the NSCL is known to leave a fraction of ^{43}S nuclei in the isomeric $7/2^-$ state at 320 keV. Since this level has a half-life of 415 ns [50, 51], some ^{43}S nuclei will still be in this excited when they reach the ^{209}Bi reaction target at the center of CAESAR. Two methods were used to determine the isomeric content of the incoming ^{43}S secondary beam. In the first method, the ^{43}S beam was stopped at the center of CAESAR with a 5.1-mm thick Al stopper. For this measurement, the trigger for the data acquisition system was switched from the E1 scintillator in the S800 focal plane to the object scintillator in the beamline, which counts the number of incoming beam particles. The proportion of ^{43}S projectiles in the cocktail incoming beam was determined from the particle identification plots in subsequent runs taken under the typical experimental settings. The efficiency of CAESAR for detecting 320-keV γ rays from the decay of the isomeric state in ^{43}S was interpolated using the 303-keV and 356-keV lines from a ^{133}Ba source. In addition, GEANT4 simulations were performed to estimate the reduction in efficiency due to absorption in the 5.1-mm Al stopper. A reduction factor of 0.82 was calculated using the ratio of the CAESAR GEANT4 efficiency at 320 keV assuming the γ decay occurs in the center of the Al stopper to the CAESAR GEANT4 efficiency at 320 keV without a stopper. From the efficiency-corrected number of 320-keV γ rays from the decay of the isomer in ^{43}S divided by the number of incoming ^{43}S projectiles, the proportion of ^{43}S nuclei in the isomeric state at the center of CAESAR was found to be 14(3)%.

In the second method, the CsI(Na) hodoscope at the back of the S800 focal plane was utilized to determine the isomeric content of the incoming ^{43}S beam. In this setup, no reaction

target or stopper was installed at the center of CAESAR. Since no reactions occur without the target, the composition of the incoming beam was determined using particle identification from the energy loss in the S800 ionization chamber and the time-of-flight from the object scintillator to the E1 scintillator. The efficiency of the hodoscope was estimated using a GEANT4 simulation of the IsoTagger configuration which includes the Al stopping plate before the CsI(Na) detectors and the surrounding stainless steel vacuum chamber [77]. The extracted efficiency at 320 keV of 19(3)% is similar to the value measured by Momiyama *et al.* from ^{43}S produced from one-neutron knockout [15]. Dividing the efficiency-corrected number of 320-keV γ rays measured in the hodoscope by the number of incoming ^{43}S projectiles gives the isomeric content at the Al stopper of IsoTagger. In order to determine the isomeric content at the reaction target, the half-life of the isomeric state must be considered. For the no reaction target setting, the average velocity of the ^{43}S nuclei is 0.396c. Therefore, using a half-life of 415 ns and a distance of 15 m between the reaction target and the Al stopper of IsoTagger, 81% of the ^{43}S nuclei survive the flight from the reaction target to the Al stopper in the S800 focal plane. Taking this into account gives an isomeric content of 18(4)% for ^{43}S at the reaction target.

The average of the isomeric content measurements is 16(5)% where the difference in the results using the two different methods has been adopted as the systematic uncertainty. The distance from the ^{9}Be production target to the A1900 focal plane is about 35.5 m [97] and the distance from the A1900 focal plane to the S800 focal plane is about 58 m [98]. Using approximately 15 m for the distance between the reaction target and the S800 focal plane, the distance from the production target to the reaction target is about 78.5 m. Assuming a half-life of 415 ns, a velocity of 0.396c, and 16% of ^{43}S in the isomeric state at the reaction target, the initial isomeric ratio at the production target is about 0.5. Therfore,

the fragmentation of the ^{48}Ca primary beam leaves ^{43}S in the isomeric state or states that feed the isomeric state about half of the time. For comparison, the fraction of the cross sections from one-neutron knockout to the isomeric $7/2^-$ state in ^{43}S and to the state at 1852 keV that γ decays to the isomer to the inclusive cross section is also about 0.5 [15].

4.3.2 Intermediate-Energy Coulomb Excitation of ^{43}S

The γ-ray spectrum from CAESAR for ^{43}S after Doppler reconstruction is shown in Figure 4.20 using a laboratory-frame scattering angle cut of 40 mrad. The higher-energy region of the spectrum is shown in the top panel of Figure 4.20 while the lower-energy region is provided in the bottom panel. The highest-statistics peak observed in this work is at 979(6) keV. In previous experiments, this transition has been reported at 971(6) keV [52], 977(9) keV [53], and 977(3) keV [15]. In [53], this transition was inferred to feed a level at 184(2) keV from lifetime measurements. However, it was noted that the observed intensities of the 184-keV and 977-keV γ rays were equal within uncertainties [53], as was the case in [52]. In the recent one-neutron knockout work, the efficiency-corrected intensity of the 977-keV transition was found to be larger than the intensity of the 185(1)-keV peak, establishing the 977-keV γ decay as a ground state transition and the 185-keV γ decay as originating from a state at 1162 keV [15]. As seen in the bottom panel of Figure 4.20, the 185-keV transition is not observed in this work, providing clear evidence for the level scheme proposed in [15]. For comparison, the Doppler-corrected γ-ray spectrum for ^{43}S produced from one-neutron removal measured in this experiment during the ^{44}S setting is shown in Figure 4.21. In this plot, the 185-keV transition, which is of similar efficiency-corrected intensity as the 977-keV transition, is clearly visible. This figure shows events where either one or two γ rays were detected in CAESAR after nearest-neighbor addback. The bottom panel of Figure 4.20 also

shows a wide feature resulting from the in-flight decay of the 320-keV isomer. Since the γ decay of the isomer can occur at any point along the beam line, Doppler reconstruction assuming the decay occurs at the middle of the reaction target does not result in a peak at 320 keV.

The top panel of Figure 4.20 also shows weaker peaks at 1168(27) keV, 1219(22) keV, and 1525(10) keV. The energies of these transitions were measured at 1154(7) keV, 1203(7) keV, and 1529(9) keV in [52], at 1159(9) keV, 1213(10) keV, and 1543(13) keV in [53], and at 1155(3) keV, 1209(3) keV, and 1532(4) keV in [15]. The 1155-keV γ ray has been placed in the level scheme for ^{43}S as a transition to the ground state [15, 52, 53], as has the 1209-keV transition [15]. In this work, no γ-γ coincidence relationships were observed in the data collected with CAESAR, in agreement with the previous placements of transitions. The prompt 1532-keV transition has been measured in coincidence with the isomeric 320-keV decay in the hodoscope [15]. In this work, additional evidence consistent with the 1532-keV transition feeding the 320-keV isomer is seen in Figure 4.22, which shows the CAESAR spectrum for multiplicity one events after nearest-neighbor addback in coincidence with the 320-keV peak measured in the hodoscope with background subtraction applied.

The angle-integrated cross section for the 977-keV transition is shown in the top panel Figure 4.23 as a function of maximum scattering angle. As for ^{38,40,44}S, the extracted $B(E2)$ strength does not decrease with scattering angle cut in the same manner observed for ^{42}S. The nominal safe scattering angle in the laboratory frame from the touching spheres plus 2 fm approximation is about 47 mrad. Using the more restrictive choice of 40 mrad, the $B(E2)$ strength from the $3/2^-$ ^{43}S ground state to the level at 977 keV is 91(18) e^{2}fm^4. With the same choice for the maximum scattering angle, the $B(E2)$ strengths to the 1155-keV and 1209-keV states are 9(7) e^{2}fm^4 and 23(11) e^{2}fm^4, respectively. Similarly, the $B(E2)$ strength

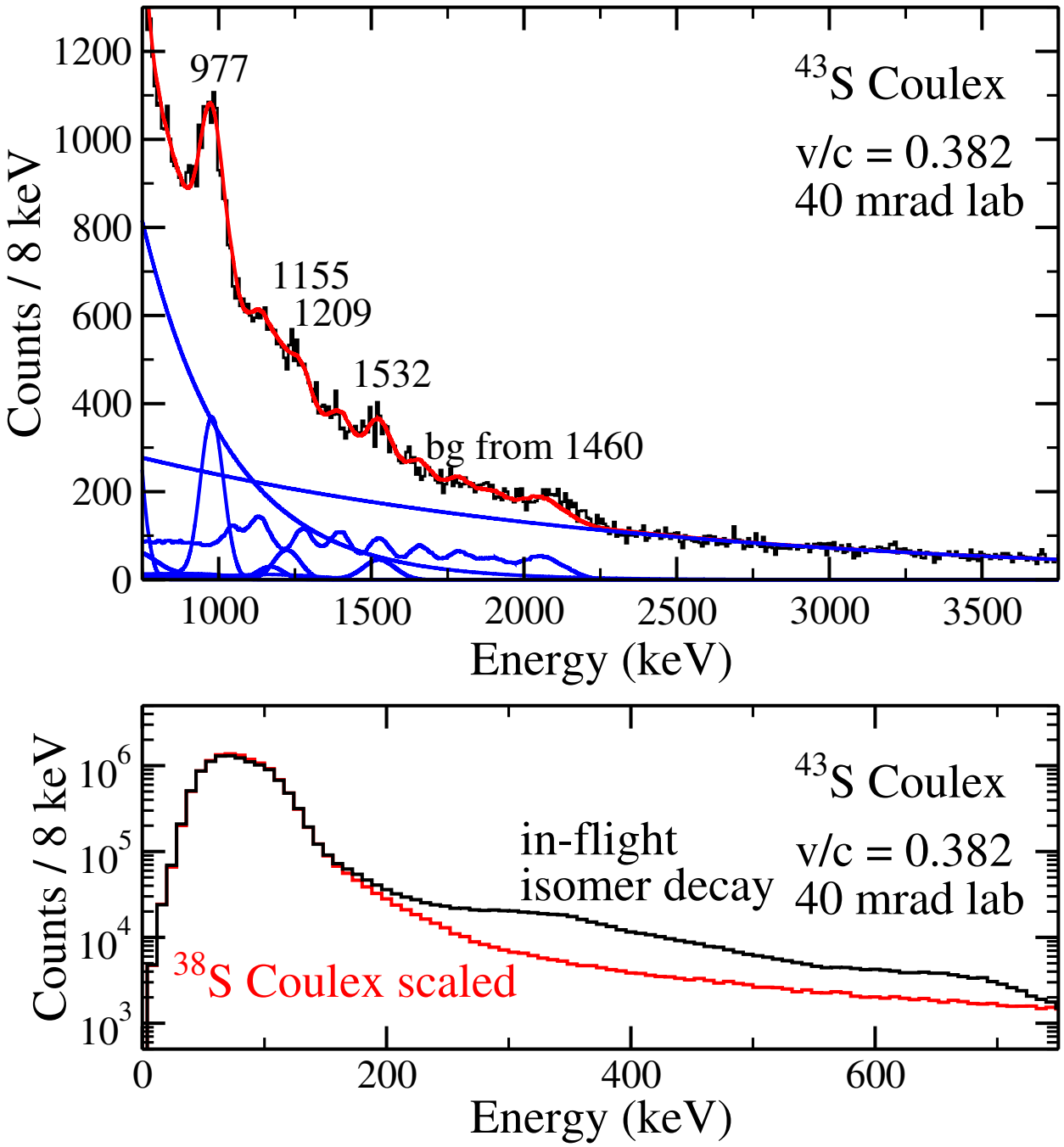

Figure 4.20: Top: Doppler-corrected energy spectrum for ^{43}S gated on scattering angles smaller than 40 mrad in the laboratory frame. The blue curves are the individual components of the fit function derived from GEANT4 simulations along with a double exponential background. The red curve is the total fit function. Bottom: Low-energy portion of the Doppler-corrected energy spectrum for ^{43}S. The wide feature present in the ^{43}S data that is not present for ^{38}S is due to the continuous decay of the 320-keV isomer at different points along the beam line. The large background at low energies is due to bremsstrahlung and other beam-correlated background.

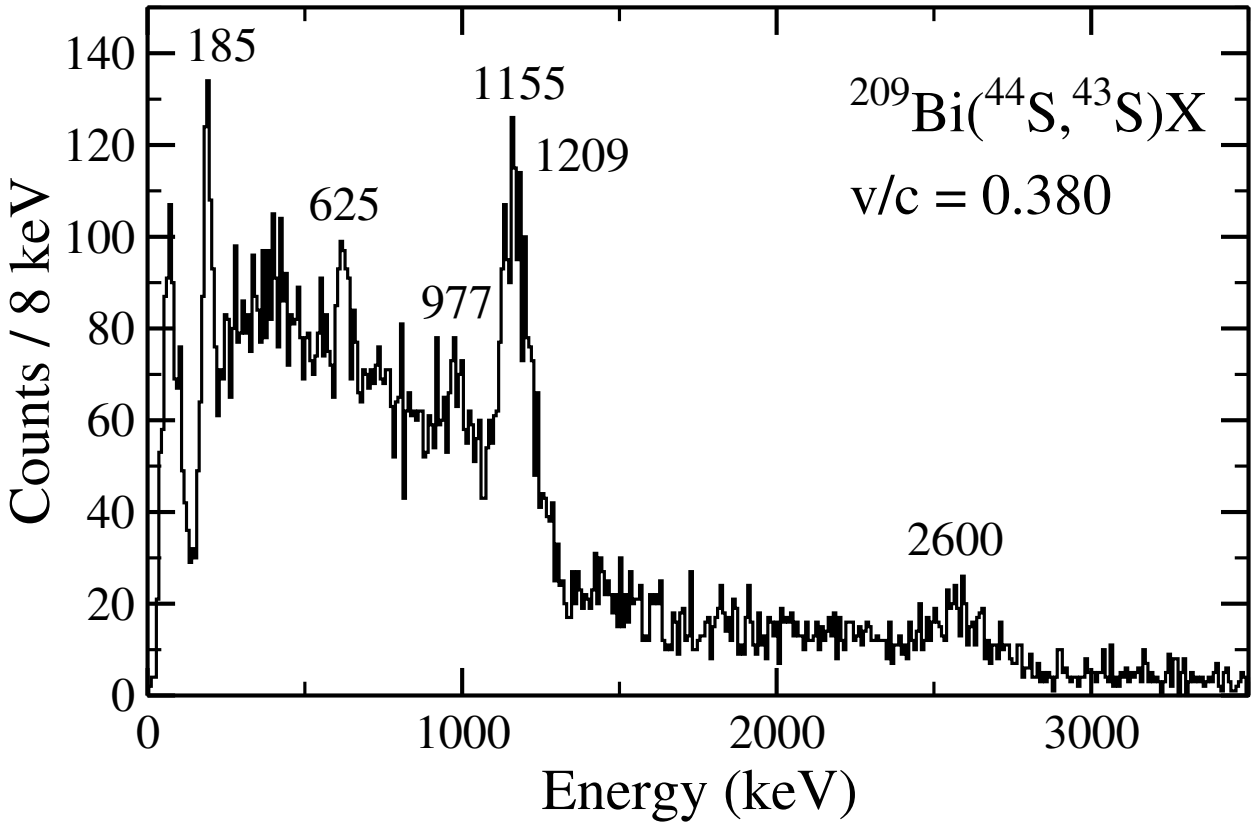

Figure 4.21: Doppler-corrected energy spectrum for ^{43}S produced from one-neutron removal for addback events with exactly one or two detected γ rays. The labeled peaks were also observed in the high-resolution ^{9}Be(^{44}S,^{43}S)X data presented in [15].

from the $7/2^-$ isomeric state at 320 keV to the level at 1852 keV that decays via a 1532-keV γ-ray transition was found to be 101(42) e^2fm^4. When calculating these electric quadrupole transition strengths, the numbers of incoming ^{43}S nuclei in the ground and isomeric states were utilized based on the proportion calculated in the previous subsection.

$B(E2)$ strengths for low-lying states in ^{43}S predicted using the SDPF-MU interaction are shown in Figure 4.24 in comparison with the results found in this work. Based on the intensity of the 977-keV transition observed experimentally, the 977-keV level is assigned as the $7/2^-_2$ state, establishing it as a member of the rotational band built on top of the $3/2^-$ ground state. Furthermore, the 1155-keV and 1209-keV states are most similar to the

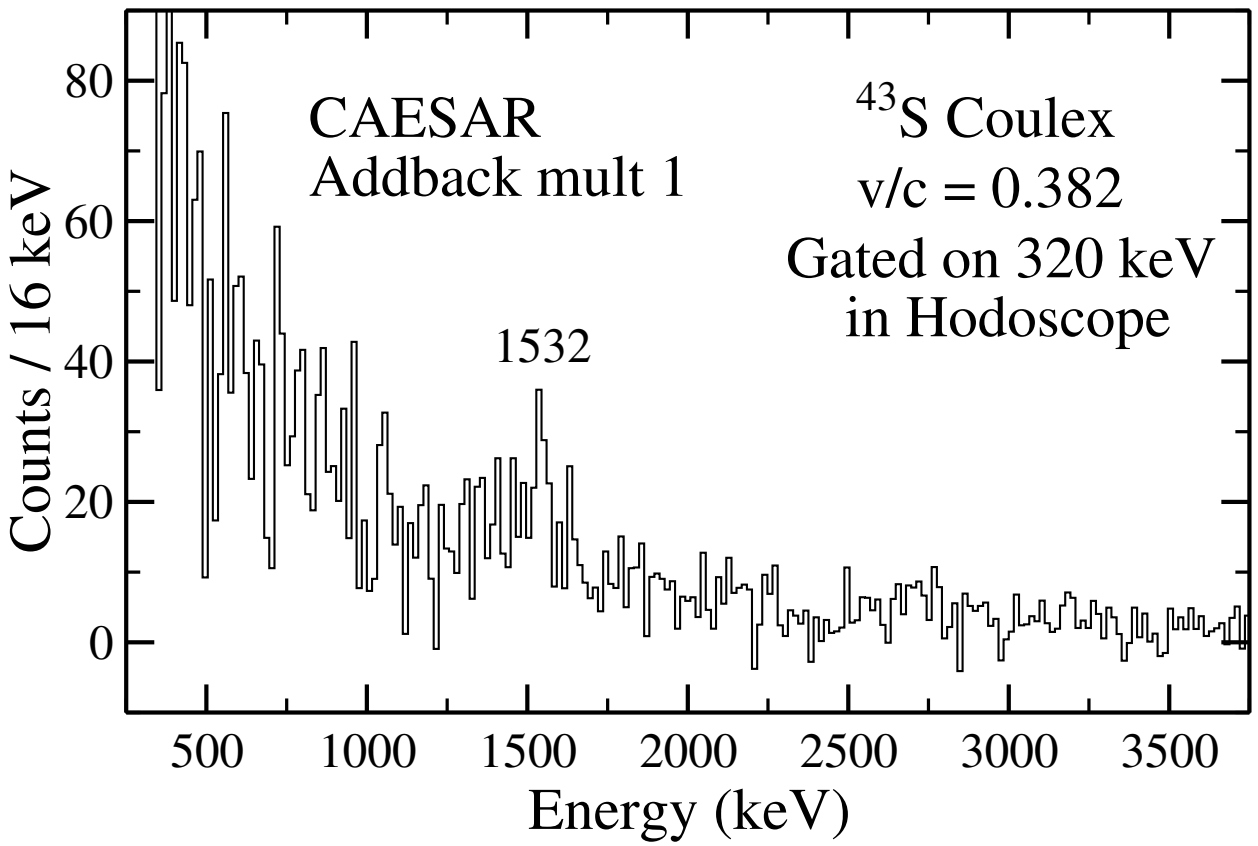

Figure 4.22: Background-subtracted, Doppler-corrected energy spectrum for ^{43}S measured with CAESAR in coincidence with 320-keV γ rays detected on the hodoscope at the S800 focal plane from the decay of the isomer. The CAESAR spectrum is for addback multiplicity one.

shell-model $3/2^-_2$ and $5/2^-_1$ levels. Note that SDPF-MU predicts that the $3/2^-_2$ and $5/2^-_1$ states decay predominantly to the ground state (100%) with only 20% and 22% relative branching ratios to all other states, respectively. The second largest brancing ratios are to the low-lying $1/2^-$ state. Experimentally, this state is tentatively reported at 228 keV [15]. Since these other decay branches would result in γ rays at 927 keV and 981 keV, a portion of the $B(E2)$ strength to the 1155-keV and 1209-keV states may be misattributed to the 977-keV state. The 228-keV transition was not observed in this experiment. Finally, the 1852-keV state is assigned as the $9/2^-_1$ level built on top of the isomeric $7/2^-_1$ state. In the shell-model calculations, the $B(E2)$ strength is 137 e^2fm^4, in good agreement with the

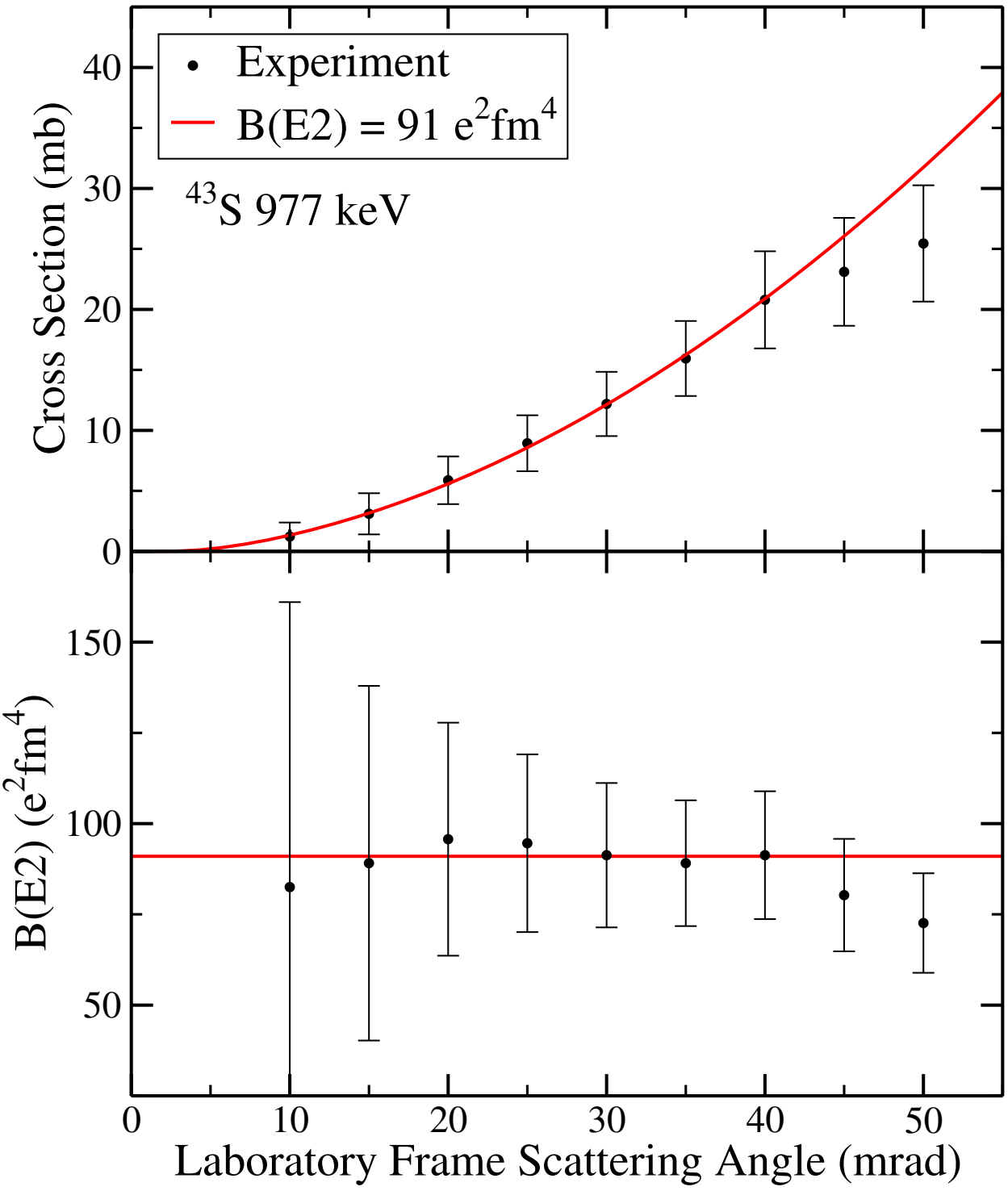

Figure 4.23: Top: feeding-subtracted angle-integrated cross section as a function of choice of scattering angle cut derived from the experimental data for the 977-keV state in ^{43}S (black). The red curve is the expected cross section assuming a $B(E2)$ strength of 91 e^{2}fm^4 from the ground state to the 977-keV level. Bottom: $B(E2)$ strength calculated using Alder-Winther theory for different choices of maximum scattering angle.

measured value of 101(42) e^2fm^4. In [15], a peak at 1865(6) keV was observed with 17% intensity relative to the 1532-keV transition and it was suggested that this γ ray could be a transition from the 1852-keV state to the ground state based solely on its energy. Due to the large spin difference between the $3/2^-$ ground state and the $9/2^-$ level at 1852 keV established in the present work, this 1865-keV transition is strongly suggested to originate from a different level.

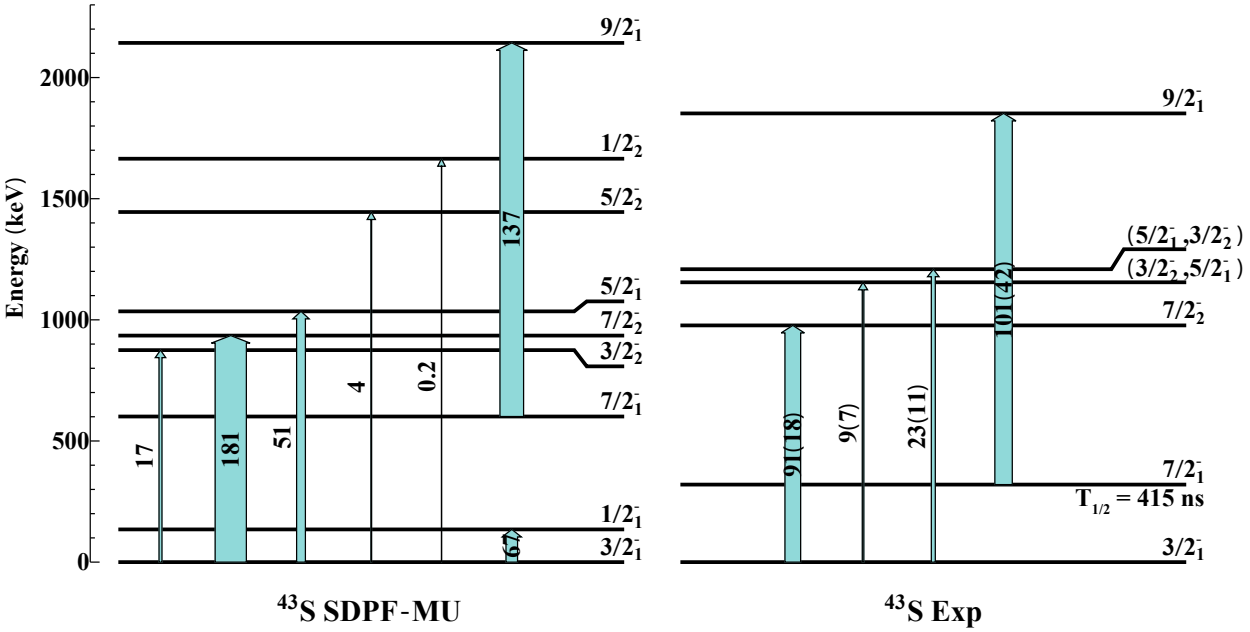

Figure 4.24: SDPF-MU predictions for $B(E2)$ strengths in e^2fm^4 for low-lying levels in ^{43}S compared with experimental results. Arrow widths are proportional to transition strength.

In a previous intermediate-energy Coulomb excitation experiment, the $B(E2)$ strength to a level around 940 keV in ^{43}S was measured to be 175(69) e^2fm^4 [99] which is almost a factor of two larger than the value of 91(18) e^2fm^4 reported to the later-observed level at 977(3) keV [15], measured in this work at 979(6) keV. It was noted by Ibbotson *et al.* that the reported 940-keV peak may consist of multiple γ ray transitions within the 8% energy resolution of the detector array utilized [99]. In this work and in the other in-beam γ-ray spectroscopy experiments [15, 52, 53], no multiplets in this energy range were observed. The

reported energy for the observed transition in ^{45}Cl was 929(17) keV in [99] which is in very good agreement with the literature value of 928(6) keV [7]. Suppose the ^{43}S peak reported at 940 keV in [99] has two components, the 977-keV transition reported in this work and in the other in-beam γ-ray spectroscopy experiments [15, 52, 53] and a 903-keV transition from the decay of the 2_1^+ state in ^{42}S. The number of incoming ^{42}S particles was reported to be nearly a factor of 7 larger than the number of incoming ^{43}S particles in [99]. In addition, this contaminant transition may be present due to one-neutron removal from ^{43}S. The energy of the 940-keV peak could then be explained as the centroid of the 977-keV and 903-keV transitions with each transition contributing about half of the counts. Since the $B(E2)$ strength to the 903-keV state in ^{42}S is larger than the $B(E2)$ strength to the 977-keV state in ^{43}S, the average number of 903-keV γ rays per incoming particle is higher. Consequently, the $B(E2)$ strength to the 977-keV level would be overestimated. For a simple estimate of the scale of this effect, suppose the experimental details for ^{42}S and ^{43}S are identical and neglect any contribution from one-neutron removal so that the following relation holds:

$$N_{903} \propto B(E2)_{903} \times N_{^{42}\mathrm{S}} = B(E2)_{977} \times N_{^{43}\mathrm{S}} \propto N_{977}. \tag{4.10}$$

Here, $N_{^{42}\mathrm{S}}$ is the number of incoming ^{42}S projectiles and $N_{^{43}\mathrm{S}}$ is the number of incoming ^{43}S projectiles. From above, the number of 903 keV and 977 keV γ rays, N_{903} and N_{977}, are approximately equal. Using a $B(E2)$ strength to the 903-keV transition of 326 e^{2}fm^4, the measured value for the combined $B(E2)$ strength of 175 e^{2}fm^4 [99] is then the weighted average:

$$175 = \frac{326 \times N_{^{42}\mathrm{S}} + B(E2)_{977} \times N_{^{43}\mathrm{S}}}{N_{^{42}\mathrm{S}} + N_{^{43}\mathrm{S}}}. \tag{4.11}$$

Solving these relations simultaneously gives a purity of $N_{^{43}\mathrm{S}} = 2.73 N_{^{42}\mathrm{S}}$ and a $B(E2)_{977}$

strength of 120 e^2fm^4, which is much closer to the value extracted in this experiment than 175 e^2fm^4.

For ^{45}Cl, Ibbotson *et al.* report the $B(E2)$ strength to the 929(17)-keV state as 87(24) e^2fm^4 [99]. In this work, incoming ^{45}Cl nuclei were present in the ^{44}S setting. The Doppler-corrected γ-ray energy spectrum for ^{45}Cl projectiles identified from time-of-flight and energy loss is shown in Figure 4.25. Here, the energy of the peak was measured as 928(9) keV. The resulting $B(E2)$ strength using a 40 mrad labortory-frame scattering angle cut is 82(29) e^2fm^4 which is in good agreement with the previous intermediate-energy Coulomb excitation measurement. The touching spheres plus 2 fm approximation gives a nominal laboratory-frame safe scattering angle cut of about 47 mrad.

The lifetimes of the 977-keV and 184-keV transitions were measured by Mijatovic *et al.* using the recoil-distance method with a plunger device [53]. The best-fit results were obtained assuming the 977-keV transition feeds the 184-keV transition which is shown in this work and the work of Momiyama *et al.* to be incorrect [15]. Under the assumption that the 184-keV transition feeds the 977-keV transition, a lower-quality fit was obtained and the lifetime of the 1161-keV state was found to be 15(2) ps while the lifetime of the 977-keV state was inferred to be very short [53]. Assuming the 977-keV state is the $7/2^-_2$ level, the decay to the $3/2^-$ ground state will be predominantly $E2$ and the limit of zero lifetime corresponds to a $B(E2)$ value approaching infinity. Interestingly, if the lifetime of the 977-keV level is 15 ps instead of the 1161-keV level, the corresponding $B(E2)$ strength from the $3/2^-$ ground state to the $7/2^-$ 977-keV state would be 122 e^2fm^4. The lifetime for the $7/2^- \rightarrow 3/2^-$ γ decay calculated from the $B(E2; 3/2^- \rightarrow 7/2^-)$ value of 91 e^2fm^4 measured in this work is 20 ps.

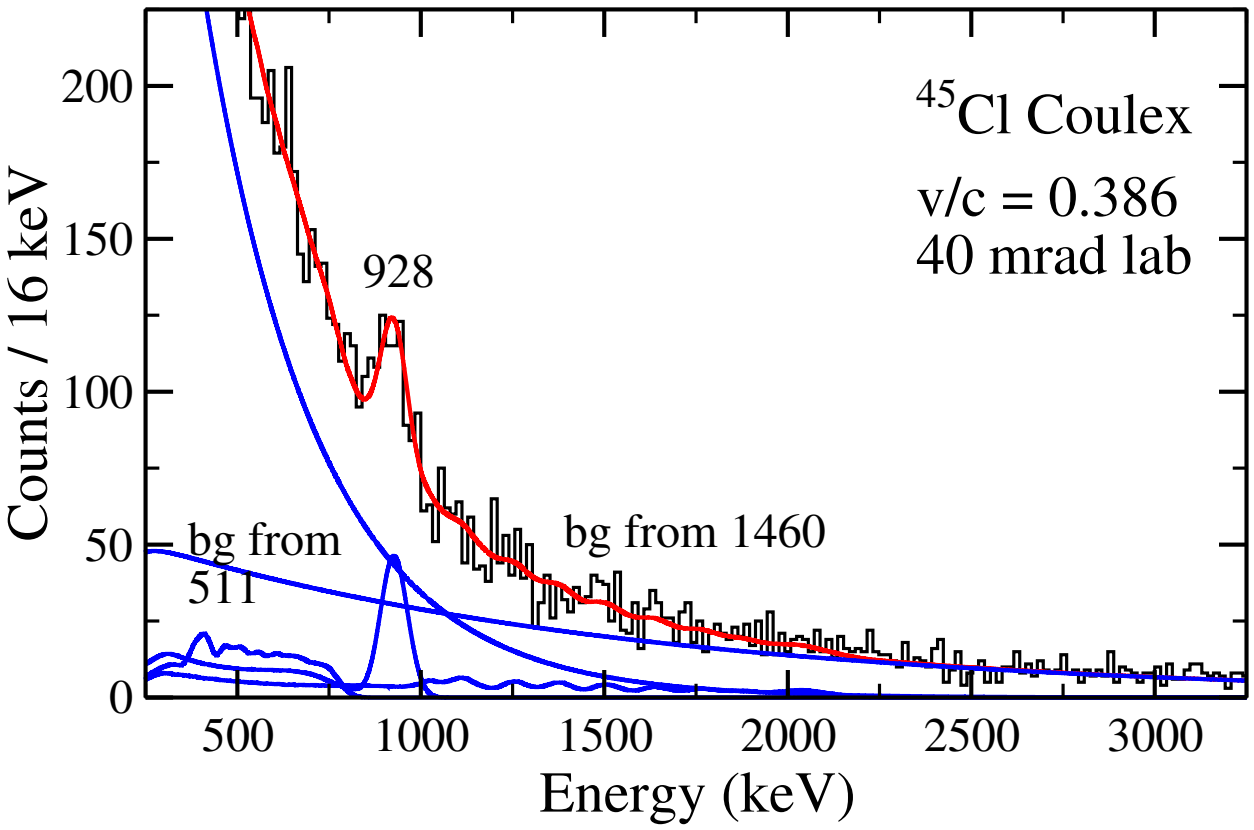

Figure 4.25: Doppler-corrected energy spectrum for ^{45}Cl gated on scattering angles smaller than 40 mrad in the laboratory frame. The blue curves are the individual components of the fit function derived from GEANT4 simulations along with a double exponential background. The red curve is the total fit function.

Chapter 5

Discussion

The $B(E2)$ strengths determined for the even-even sulfur isotopes in this work using intermediate-energy Coulomb excitaion are provided in Table 5.1 along with the values from the previous intermediate-energy Coulomb excitation experiments [28, 29] and the strengths predicted by the SDPF-MU interaction. In general, the $B(E2; 0_1^+ \rightarrow 2_1^+)$ strengths extracted in this work are slightly lower than those published by Scheit *et al.* [28] and Glasmacher *et al.* [29]. The effects of transitions feeding the 2_1^+ states on the reduced transition strengths were taken into account in this experiment while feeding transitions were not observed in the previous works due to limited statistics and thus could not be subtracted. Furthermore, the $B(E2; 0_1^+ \rightarrow 2_1^+)$ strengths in ^{42}S calculated from recent lifetime measurements of 329(26) e^2fm^4 [45] and 315^{+18}_{-16} e^2fm^4[53] are slightly below the value of 397(63) e^2fm^4 from Scheit *et al.* and in good agreement with the value of 326(48) e^2fm^4 found in the present work. Figure 5.1 shows a visual comparison of the measured $B(E2)$ strengths and the $B(E2)$ strengths predicted using the SDPF-MU interaction. Overall, there is very good agreement between experiment and theory up to and including $N = 26$.

In ^{38}S, shell-model calculations using the SDPF-MU interaction yield a $B(E2; 0_1^+ \rightarrow 2_1^+)$ strength of 160 e^2fm^4, which is slightly lower than the experimental value of 229(19) e^2fm^4. In addition, SDPF-MU predicts a $B(E2; 0_1^+ \rightarrow 2_2^+)$ strength of 25 e^2fm^4 and a $B(E2; 0_1^+ \rightarrow 2_3^+)$ strength of 26 e^2fm^4. In this work, the $B(E2; 0_1^+ \rightarrow 2_2^+)$ strength was measured as

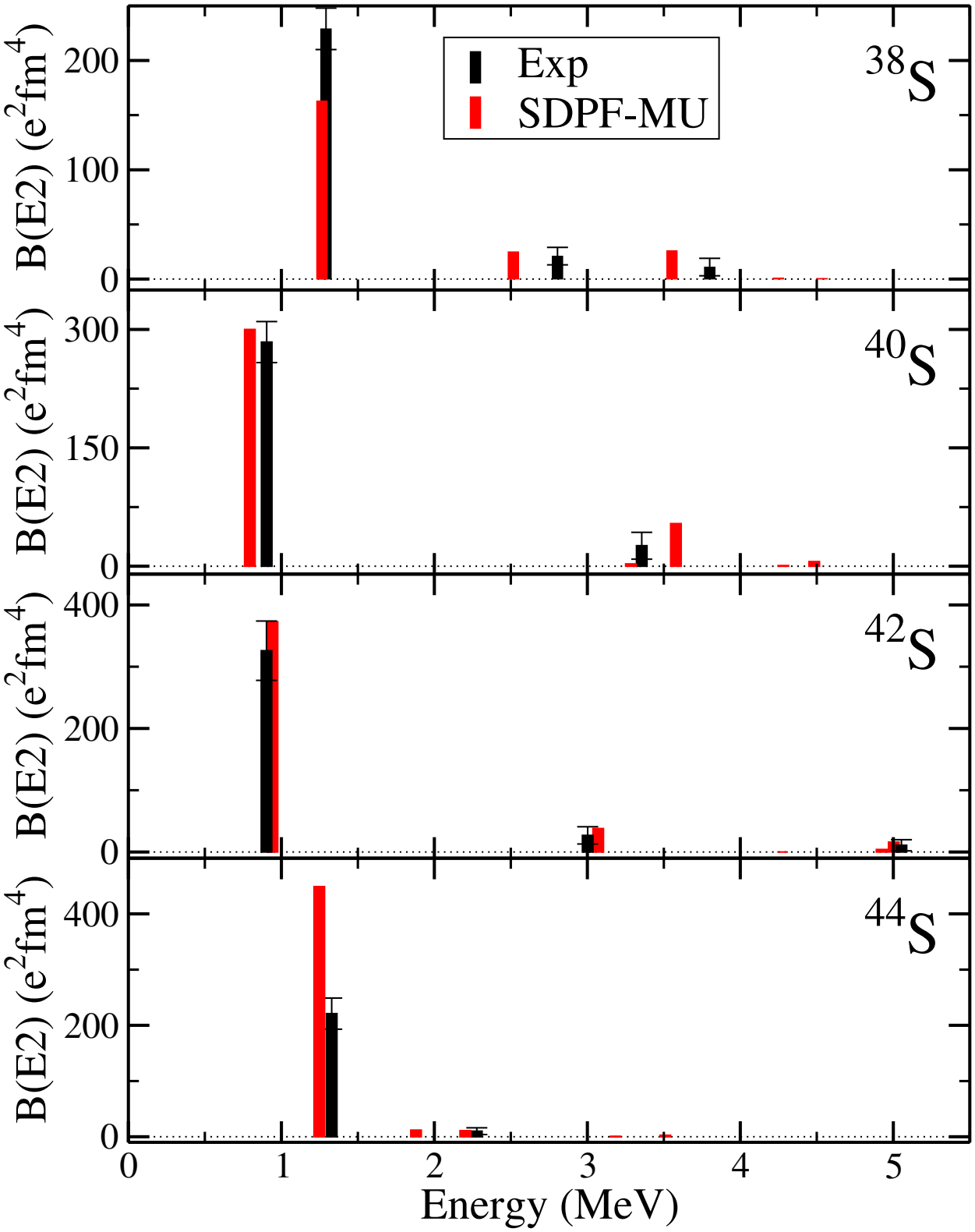

Figure 5.1: $B(E2; 0_1^+ \rightarrow 2^+)$ strengths in the even-even sulfur isotopes for the 2^+ states measured in this work compared to predictions from the SDPF-MU Hamiltonian for the first five 2^+ states.

Table 5.1: $B(E2)$ strengths for the neutron-rich sulfur isotopes studied in this work compared to the results of previous intermediate-energy Coulomb excitation experiments and theoretical calculations using the SDPF-MU Hamiltonian with effective proton and neutron charges of 1.35 and 0.35, respectively.

Nucleus	Excitation	This Work e^2fm^4	Previous Works e^2fm^4	Theory (SDPF-MU) e^2fm^4
^{38}S	$0_1^+ \rightarrow 2_1^+$	229(19)	235(30) [28]	160
	$0_1^+ \rightarrow 2_2^+$	21(8)		25
	$0_1^+ \rightarrow 2_3^+$	11(8)		26
^{40}S	$0_1^+ \rightarrow 2_1^+$	284(26)	334(36) [28]	300
	$0_1^+ \rightarrow 2_2^+$			3
	$0_1^+ \rightarrow 2_3^+$	26(17)		54
^{42}S	$0_1^+ \rightarrow 2_1^+$	326(48)	397(63) [28]	370
	$0_1^+ \rightarrow 2_2^+$	27(14)		38
	$0_1^+ \rightarrow 2_5^+$	11(9)		16
^{44}S	$0_1^+ \rightarrow 2_1^+$	221(28)	314(88) [29]	450
	$0_1^+ \rightarrow 2_2^+$			12
	$0_1^+ \rightarrow 2_3^+$	10(6)		11

21(8) e^2fm^4 from the 1513-keV $2_2^+ \rightarrow 2_1^+$ transition while the reduced transition strength from the ground state to the newly-observed level at 3800(25) keV was found to be 11(8) e^2fm^4 from the 2508-keV transition to the 2_1^+ state. Based on the theoretical calculations, the 3800-keV level is inferred to have structure most similar to the shell-model 2_3^+ state. The 2_2^+ state at 2805 keV was observed to γ decay to the 2_1^+ level but not to the ground state, consistent with the previous measurements [10, 48] and with the dominance of the $2_2^+ \rightarrow 2_1^+$ branch predicted by SDPF-MU.

For ^{40}S, the SDPF-MU Hamiltonian predicts a $B(E2; 0_1^+ \rightarrow 2_1^+)$ strength of 300 e^2fm^4 compared to the measured value of 284(26) e^2fm^4. Moreover, the shell-model calculations predict a 54 e^2fm^4 $B(E2; 0_1^+ \rightarrow 2_3^+)$ strength while the $B(E2; 0_1^+ \rightarrow 2_2^+)$ strength is only

2.9 e^2fm^4. In this work, the reduced transition probability from the ground state to the presumed 2^+ level at 3356(23) keV was found to be 26(17) e^2fm^4. Based on its observation in this work, the 3356(23)-keV level corresponds more closely to the collective shell-model 2_3^+ state. The predicted relative branching ratios for the 2_3^+ state are 100% to the 2_1^+ level and 8% to the ground state. In this experiment, only the $2_3^+ \rightarrow 2_1^+$ branch of the newly-reported 3356(23)-keV state was observed, consistent with the theoretical predictions given the level of statistics. In the single-particle picture discussed in [10] and reproduced in Figure 1.8, the neutron $1p_{3/2}$ occupancy for the ground state is very similar to the neutron $1p_{3/2}$ occupancies for the 2_1^+ and 2_3^+ states, both of which states were observed in the present work. The SDPF-MU neutron $1p_{3/2}$ occupancy of the unobserved 2_2^+ level is only slightly higher but is nearly identical to the neutron $1p_{3/2}$ occupancy of the 0_2^+ state, which is predicted to be at nearly the same excitation energy.

Shell-model calculations for ^{42}S give a $B(E2; 0_1^+ \rightarrow 2_1^+)$ strength of 370 e^2fm^4 which is slightly above the experimental result from this work of 326(48) e^2fm^4. In addition, SDPF-MU predicts a $B(E2; 0_1^+ \rightarrow 2_2^+)$ strength of 38 e^2fm^4 compared to the measured value of 27(14) e^2fm^4. The shell-model calculations also predict a $B(E2; 0_1^+ \rightarrow 2_5^+)$ strength of 16 e^2fm^4. Assuming an $E2$ excitation, the reduced transition strength to the level at 5053(110) keV is 11(9) e^2fm^4. However, the 4150(110)-keV transition from the 5053(110)-keV state observed in this work may correspond to multiple unresolved transitions, such as the 4102-keV and 4266-keV transitions reported in [10]. In addition, the branching ratios of the tentatively assigned 2_2^+ level at 3002-keV to the 2_1^+ state and the ground state measured by Lunderberg *et al.* were in remarkable agreement with the predictions from SDPF-MU [10]. In this work, the 3002-keV state was confirmed as the 2_2^+ level. Overall, the SDPF-MU Hamiltonian predictions for the energies of 2^+ states and $E2$ strengths in ^{42}S are in

very good agreement with the experimental results, as seen in Figure 5.1, supporting the single-particle evolution sketched with the neutron $1p_{3/2}$ occupancy in Figure 1.8.

The SDPF-MU interaction predicts a $B(E2; 0_1^+ \rightarrow 2_1^+)$ strength of 450 e^2fm^4 for $N = 28$ ^{44}S. In this work, the measured $B(E2; 0_1^+ \rightarrow 2_1^+)$ strength is roughly half of this value at 221(28) e^2fm^4. The $B(E2; 0_1^+ \rightarrow 2_2^+)$ and $B(E2; 0_1^+ \rightarrow 2_3^+)$ strengths from the shell-model calculation are 12 e^2fm^4 and 11 e^2fm^4, respectively. The experimental value for the $B(E2; 0_1^+ \rightarrow 2_3^+)$ strength from the 949-keV transition of the 2278-keV state in this work is 10(6) e^2fm^4. The yield of possible 2150-keV transitions from the decay of the 2_2^+ level to the ground state was not well constrained due to Doppler-corrected 1460-keV laboratory-frame background. A similar overprediction of the $B(E2; 0_1^+ \rightarrow 2_1^+)$ strength by shell-model calculations has been reported for $N = 28$ ^{46}Ar, just two protons above ^{44}S. While a lifetime measurement obtained a value of 570^{+335}_{-160} e^2fm^4 [100], intermediate-energy Coulomb excitation experiments have resulted in consistent strengths of 196(39) e^2fm^4 [28], 218(31) e^2fm^4 [62], and 225(29) e^2fm^4 (absoulte) and 234(19) e^2fm^4 (relative to ^{44}Ca) [101]. Shell-model interactions including SDPF-MU predict a $B(E2; 0_1^+ \rightarrow 2_1^+)$ strength roughly a factor of two larger at around 500 e^2fm^4 [101].

From the experimental results in the present work, the $B(E2; 0_1^+ \rightarrow 2_1^+)$ strength peaks at $N = 26$ for the sulfur isotopes between $N = 22$ and $N = 28$. SDPF-MU predictions, however, put the maximum collectivity at $N = 28$ rather than $N = 26$ over this range of neutron numbers. For comparison, the SDPF-MU $B(E2; 0_1^+ \rightarrow 2_1^+)$ strengths for ^{44}S and ^{46}S are nearly the same at about 450 e^2fm^4 while the SDPF-MU $B(E2; 0_1^+ \rightarrow 2_1^+)$ strength for ^{48}S is lower at around 330 e^2fm^4. For the argon isotopic chain, there is a similar relationship between the experimental results and shell-model calculations. The $B(E2; 0_1^+ \rightarrow 2_1^+)$ strength in $N = 28$ ^{46}Ar [101] as discussed above and the $B(E2)$ strength from the $3/2^-$

ground state to low-lying states for $N = 29$ ^{47}Ar [102] are significantly overpredicted by shell-model calculations by roughly a factor of two. At $N = 30$, the reported $B(E2; 0_1^+ \rightarrow 2_1^+)$ strength of 346(55) e^{2}fm^4 is in better agreement with theoretical calculations but is still about 1.5 to 2 standard deviations lower than predicted [102]. Consequently, reproducing the observed $B(E2)$ strengths near $N = 28$ for argon and sulfur may serve as important benchmarks for future shell-model interactions.

In ^{43}S, collective structures built on top of the intruder $3/2^-$ ground state and the normal-order $7/2^-$ isomeric state were characterized. The $B(E2)$ strength to the 977-keV state was measured to be 91(18) e^{2}fm^4 while the largest $B(E2)$ strength predicted by the SDPF-MU Hamiltonian from the ground state is 181 e^{2}fm^4 to the $7/2_2^-$ level. The overprediction by a factor of two is similar for the $B(E2; 0_1^+ \rightarrow 2_1^+)$ strengths in ^{44}S and ^{46}Ar discussed above. A previous intermediate-energy Coulomb excitation experiment measured a $B(E2)$ strength of 175(69) e^{2}fm^4 using a peak at appropriately 940 keV [99] which may include some contamination from the 903-keV level in ^{42}S. It would be interesting to revisit the lifetime measurements performed for states in ^{43}S [53]. In [53], the 184-keV transition was assumed to be fed by the 977-keV transition and tentatively assigned as originating from the low-lying $1/2^-$ state. In both this work and [15], the 977-keV transition was found to be to the ground state. Furthermore, the newly-observed 228-keV level is tentatively assigned as the $1/2^-$ state in [15]. Levels at 1155 keV and 1209 keV were also Coulomb excited from the ground state of ^{43}S with $B(E2)$ values of 9(7) e^{2}fm^4 and 23(11) e^{2}fm^4, respectively. The SDPF-MU $B(E2)$ strengths from the ground state to the $3/2_2^-$ and $5/2_1^-$ states are 17 e^{2}fm^4 and 51 e^{2}fm^4, respectively. The 1532-keV transition was found to be in coincidence with the 320-keV isomer in agreement with results from one-neutron knockout [15]. The $B(E2)$ strength from the 320-keV isomer present in the incoming beam to the 1852-keV level was

found to be 101(42) e^2fm^4. The SDPF-MU Hamiltonian predicts a $B(E2)$ strength from the $7/2^-$ isomer to the $9/2^-$ state of 137 e^2fm^4. As discussed in [51], the normal-order configuration provides the largest contribution to the wavefunction of the $7/2^-$ isomer but intruder configurations also play a role. For example, the measured spectroscopic quadrupole moment of 23(3) efm^2 is larger than expected for a single-hole state and well-reproduced by shell-model calculations [51]. Here, the measured $B(E2; 7/2^-_1 \rightarrow 9/2^-_1)$ strength is also in agreement with the shell-model prediction, supporting the picture of shape coexistence painted by the SDPF-MU interaction.

Chapter 6

Summary and Outlook

Reduced electromagnetic transition strengths in the neutron-rich sulfur isotopes ^{38,40,42,43,44}S were measured using the technique of intermediate-energy Coulomb excitation with the CsI(Na) scintillator array CAESAR and the S800 magnetic spectrograph at the National Superconducting Cyclotron Laboratory. For the even-even neutron-rich sulfur isotopes the $B(E2)$ strengths from the ground states to multiple low-lying 2^+ states were investigated. For ^{43}S, the isomeric content of the incoming beam was exploited in order to measure quadrupole collectivity from both the ground state and the isomeric state at 320 keV.

Looking forward, the Facility for Rare Isotope Beams (FRIB) is scheduled to begin operations in 2022. With the new linear accelerator replacing the coupled cyclotrons, FRIB will provide rare isotope beams at intensities roughly three orders of magnitude greater than the NSCL [67]. With the increased beam intensities available, it may be possible to perform low-energy Coulomb excitation of the neutron-rich sulfur isotopes studied in this work. For beam energies below the Coulomb barrier, multi-step excitations can occur, allowing population of excited states that are high in energy. With semi-classical coupled-channels Coulomb excitation codes such as GOSIA [103], the yields of the de-excitation γ rays detected experimentally as a function of the scattering angle of the radioactive nucleus can be used to determine electromagnetic transition matrix elements in a model-independent

fashion. The diagonal matrix elements are related to the static electromagnetic moments and characterize the shape and degree of deformation of the nucleus. Furthermore, with the increased beam intensities, it should be possible to perform intermediate-energy Coulomb excitation of sulfur ($Z = 16$) isotopes beyond $N = 28$ toward the limit of nuclear existence. It would also be interesting to probe the $E2$ strength distributions in the neutron-rich silicon ($Z = 14$) and magnesium ($Z = 12$) isotopes near $N = 28$ through intermediate-energy Coulomb excitation in order to benchmark the performance of state-of-the-art shell-model interactions throughout this island of inversion.

BIBLIOGRAPHY

BIBLIOGRAPHY

[1] S. McDaniel, Ph.D. thesis, Michigan State University (2011).

[2] *Isotope Science Facility at Michigan State University: Upgrade of the NSCL Rare Isotope Research Capabilities* (Michigan State University, 2006).

[3] S. R. Stroberg, Ph.D. thesis, Michigan State University (2014).

[4] M. Wang, G. Audi, A. Wapstra, F. Kondev, M. MacCormick, X. Xu, and B. Pfeiffer, Chin. Phys. C **36**, 1603 (2012).

[5] B. A. Brown, *Lecture Notes in Nuclear Structure Physics*.

[6] R. F. Casten, Front. Phys. **13(6)**, 132104 (2018).

[7] Evaluated nuclear structure data file (ensdf), https://www.nndc.bnl.gov/ensdf/ .

[8] B. Pritychenko, M. Birch, B. Singh, and M. Horoi, At. Data Nucl. Data Tables **107**, 1 (2016).

[9] T. Otsuka, T. Suzuki, R. Fujimoto, H. Grawe, and Y. Akaishi, Phys. Rev. Lett. **95**, 232502 (2005).

[10] E. Lunderberg, A. Gade, V. Bader, T. Baugher, D. Bazin, J. S. Berryman, B. A. Brown, D. J. Hartley, F. Recchia, S. R. Stroberg, D. Weisshaar, and K. Wimmer, Phys. Rev. C **94**, 064327 (2016).

[11] T. Baugher, Ph.D. thesis, Michigan State University (2013).

[12] D. Morrissey, B. Sherrill, M. Steiner, A. Stolz, and I. Wiedenhoever, Nucl. Instrum. Methods Phys. Res. B **204**, 90 (2003).

[13] A. Ratkiewicz, Ph.D. thesis, Michigan State University (2011).

[14] D. Weisshaar, A. Gade, T. Glasmacher, G. F. Grinyer, D. Bazin, P. Adrich, T. Baugher, J. M. Cook, C. A. Diget, S. McDaniel, A. Ratkiewicz, K. P. Siwek, and K. A. Walsh, Nucl. Instrum. Methods Phys. Res. A **624**, 615 (2010).

[15] S. Momiyama, Ph.D. thesis, University of Tokyo (2019).

[16] D. J. Griffiths, *Introduction to Elementary Particles* (Wiley, 2008).

[17] H. Yukawa, Proc. Phys.-Math. Soc. Jpn. **17**, 48 (1935).

[18] R. Machleidt and H. Müther, Phys. Rev. C **63**, 034005 (2001).

[19] J. Erler, N. Birge, M. Kortelainen, W. Nazarewicz, E. Olsen, A. M. Perhac, and M. Stoitsov, Nature **486**, 509 (2012).

[20] C. F. von Weizsäcker, Zeitschrift für Physik **96**, 431 (1935).

[21] M. G. Mayer, Phys. Rev. **75**, 1969 (1949).

[22] O. Haxel, J. H. D. Jensen, and H. E. Suess, Phys. Rev. **75**, 1766 (1949).

[23] R. F. Casten, *Nuclear Structure from a Simple Perspective* (Oxford University Press, 1990).

[24] D. L. Hill and J. A. Wheeler, Phys. Rev. **89**, 1102 (1953).

[25] Y. Utsuno, T. Otsuka, B. A. Brown, M. Honma, T. Mizusaki, and N. Shimizu, Phys. Rev. C **86**, 051301 (2012).

[26] F. Nowacki and A. Poves, Phys. Rev. C **79**, 014310 (2009).

[27] O. Sorlin and M.-G. Porquet, Prog. Part. Nucl. Phys. **61**, 602 (2008).

[28] H. Scheit, T. Glasmacher, B. A. Brown, J. A. Brown, P. D. Cottle, P. G. Hansen, R. Harkewicz, M. Hellström, R. W. Ibbotson, J. K. Jewell, K. W. Kemper, D. J. Morrissey, M. Steiner, P. Thirolf, and M. Thoennessen, Phys. Rev. Lett. **77**, 3967 (1996).

[29] T. Glasmacher, B. A. Brown, M. J. Chromik, P. D. Cottle, M. Fauerbach, R. W. Ibbotson, K. W. Kemper, D. J. Morrissey, H. Scheit, D. W. Sklenicka, and M. Steiner, Phys. Lett. B **395**, 163 (1997).

[30] T. Otsuka, Phys. Scr. **T152**, 014007 (2013).

[31] B. Bastin, S. Grévy, D. Sohler, O. Sorlin, Z. Dombrádi, N. L. Achouri, J. C. Angélique, F. Azaiez, D. Baiborodin, R. Borcea, C. Bourgeois, A. Buta, A. Bürger, R. Chapman, J. C. Dalouzy, Z. Dlouhy, A. Drouard, Z. Elekes, S. Franchoo, S. Iacob, B. Laurent, M. Lazar, X. Liang, E. Liénard, J. Mrazek, L. Nalpas, F. Negoita, N. A. Orr, Y. Penionzhkevich, Z. Podolyák, F. Pougheon, P. Roussel-Chomaz, M. G. Saint-Laurent, M. Stanoiu, I. Stefan, F. Nowacki, and A. Poves, Phys. Rev. Lett. **99**, 022503 (2007).

[32] E. Caurier, F. Nowacki, and A. Poves, Phys. Rev. C **90**, 014302 (2014).

[33] B. H. Wildenthal, Prog. Part. Nucl. Phys. **11**, 5 (1984).

[34] B. A. Brown and B. H. Wildenthal, Annu. Rev. Nucl. Part. Sci. **38**, 29 (1988).

[35] Y. Utsuno, T. Otsuka, T. Mizusaki, and M. Honma, Phys. Rev. C **60**, 054315 (1999).

[36] M. Honma, T. Otsuka, and T. Mizusaki, RIKEN Accelerator Progress Report **41**, 32 (2008).

[37] A. Poves and A. Zuker, Phys. Rep. **70**, 235 (1981).

[38] T. Otsuka, T. Suzuki, M. Honma, Y. Utsuno, N. Tsunoda, K. Tsukiyama, and M. Hjorth-Jensen, Phys. Rev. Lett. **104**, 012501 (2010).

[39] G. Bertsch, J. Borysowicz, H. McManus, and W. G. Love, Nucl. Phys. A **284**, 399 (1977).

[40] S. Kahana, H. C. Lee, and C. K. Scott, Phys. Rev. **180**, 956 (1969).

[41] F. Sarazin, H. Savajols, W. Mittig, F. Nowacki, N. A. Orr, Z. Ren, P. Roussel-Chomaz, G. Auger, D. Baiborodin, A. V. Belozyorov, C. Borcea, E. Caurier, Z. Dlouhý, A. Gillibert, A. S. Lalleman, M. Lewitowicz, S. M. Lukyanov, F. de Oliveira, Y. E. Penionzhkevich, D. Ridikas, H. Sakuraï, O. Tarasov, and A. de Vismes, Phys. Rev. Lett. **84**, 5062 (2000).

[42] S. Grévy, F. Negoita, I. Stefan, N. L. Achouri, J. C. Angélique, B. Bastin, R. Borcea, A. Buta, J. M. Daugas, F. De Oliveira, O. Giarmana, C. Jollet, B. Laurent, M. Lazar, E. Liénard, F. Maréchal, J. Mrázek, D. Pantelica, Y. Penionzhkevich, S. Piétri, O. Sorlin, M. Stanoiu, C. Stodel, and M. G. St-Laurent, Eur. Phys. J. A **25**, 111 (2005).

[43] B. A. Brown, Physics **3**, 104 (2010).

[44] D. Santiago-Gonzalez, I. Wiedenhöver, V. Abramkina, M. L. Avila, T. Baugher, D. Bazin, B. A. Brown, P. D. Cottle, A. Gade, T. Glasmacher, K. W. Kemper, S. McDaniel, A. Rojas, A. Ratkiewicz, R. Meharchand, E. C. Simpson, J. A. Tostevin, A. Volya, and D. Weisshaar, Phys. Rev. C **83**, 061305 (2011).

[45] J. J. Parker, I. Wiedenhöver, P. D. Cottle, J. Baker, D. McPherson, M. A. Riley, D. Santiago-Gonzalez, A. Volya, V. M. Bader, T. Baugher, D. Bazin, A. Gade, T. Ginter, H. Iwasaki, C. Loelius, C. Morse, F. Recchia, D. Smalley, S. R. Stroberg, K. Whitmore, D. Weisshaar, A. Lemasson, H. L. Crawford, A. O. Macchiavelli, and K. Wimmer, Phys. Rev. Lett. **118**, 052501 (2017).

[46] Y. Utsuno, N. Shimizu, T. Otsuka, T. Yoshida, and Y. Tsunoda, Phys. Rev. Lett. **114**, 032501 (2015).

[47] J. L. Egido, M. Borrajo, and T. R. Rodríguez, Phys. Rev. Lett. **116**, 052502 (2016).

[48] B. Fornal, R. H. Mayer, I. G. Bearden, P. Benet, R. Broda, P. J. Daly, Z. W. Grabowski, I. Ahmad, M. P. Carpenter, P. B. Fernandez, R. V. F. Janssens, T. L. Khoo, T. Lauritsen, E. F. Moore, and M. Drigert, Phys. Rev. C **49**, 2413 (1994).

[49] C. Force, S. Grévy, L. Gaudefroy, O. Sorlin, L. Cáceres, F. Rotaru, J. Mrazek, N. L. Achouri, J. C. Angélique, F. Azaiez, B. Bastin, R. Borcea, A. Buta, J. M. Daugas, Z. Dlouhy, Z. Dombrádi, F. De Oliveira, F. Negoita, Y. Penionzhkevich, M. G. Saint-Laurent, D. Sohler, M. Stanoiu, I. Stefan, C. Stodel, and F. Nowacki, Phys. Rev. Lett. **105**, 102501 (2010).

[50] L. Gaudefroy, J. M. Daugas, M. Hass, S. Grévy, C. Stodel, J. C. Thomas, L. Perrot, M. Girod, B. Rossé, J. C. Angélique, D. L. Balabanski, E. Fiori, C. Force, G. Georgiev, D. Kameda, V. Kumar, R. L. Lozeva, I. Matea, V. Méot, P. Morel, B. S. N. Singh, F. Nowacki, and G. Simpson, Phys. Rev. Lett. **102**, 092501 (2009).

[51] R. Chevrier, J. M. Daugas, L. Gaudefroy, Y. Ichikawa, H. Ueno, M. Hass, H. Haas, S. Cottenier, N. Aoi, K. Asahi, D. L. Balabanski, N. Fukuda, T. Furukawa, G. Georgiev, H. Hayashi, H. Iijima, N. Inabe, T. Inoue, M. Ishihara, Y. Ishii, D. Kameda, T. Kubo, T. Nanao, G. Neyens, T. Ohnishi, M. M. Rajabali, K. Suzuki, H. Takeda, M. Tsuchiya, N. Vermeulen, H. Watanabe, and A. Yoshimi, Phys. Rev. Lett. **108**, 162501 (2012).

[52] L. A. Riley, P. Adrich, T. R. Baugher, D. Bazin, B. A. Brown, J. M. Cook, P. D. Cottle, C. A. Diget, A. Gade, D. A. Garland, T. Glasmacher, K. E. Hosier, K. W. Kemper, A. Ratkiewicz, K. P. Siwek, J. A. Tostevin, and D. Weisshaar, Phys. Rev. C **80**, 037305 (2009).

[53] T. Mijatović, N. Kobayashi, H. Iwasaki, D. Bazin, J. Belarge, P. C. Bender, B. A. Brown, A. Dewald, R. Elder, B. Elman, A. Gade, M. Grinder, T. Haylett, S. Heil, C. Loelius, B. Longfellow, E. Lunderberg, M. Mathy, K. Whitmore, and D. Weisshaar, Phys. Rev. Lett. **121**, 012501 (2018).

[54] K. Alder, A. Bohr, T. Huus, B. Mottelson, and A. Winther, Rev. Mod. Phys. **28**, 432 (1956).

[55] D. Cline, Ann. Rev. Nucl. Part. Sci. **36**, 683 (1986).

[56] T. Glasmacher, Ann. Rev. Nucl. Part. Sci. **48**, 1 (1998).

[57] A. Gade and T. Glasmacher, Prog. Part. Nucl. Phys. **60**, 161 (2008).

[58] A. Görgen, J. Phys. G: Nucl. Part. Phys. **37**, 103101 (2010).

[59] A. Görgen and W. Korten, J. Phys. G: Nucl. Part. Phys. **43**, 024002 (2016).

[60] T. Motobayashi, Y. Ikeda, K. Ieki, M. Inoue, N. Iwasa, T. Kikuchi, M. Kurokawa, S. Moriya, S. Ogawa, H. Murakami, S. Shimoura, Y. Yanagisawa, T. Nakamura, Y. Watanabe, M. Ishihara, T. Teranishi, H. Okuno, and R. Casten, Phys. Lett. B **346**, 9 (1995).

[61] A. Winther and K. Alder, Nucl. Phys. A **319**, 518 (1979).

[62] A. Gade, D. Bazin, C. M. Campbell, J. A. Church, D. C. Dinca, J. Enders, T. Glasmacher, Z. Hu, K. W. Kemper, W. F. Mueller, H. Olliver, B. C. Perry, L. A. Riley, B. T. Roeder, B. M. Sherrill, and J. R. Terry, Phys. Rev. C **68**, 014302 (2003).

[63] H. Scheit, Ph.D. thesis, Michigan State University (1998).

[64] H. Olliver, T. Glasmacher, and A. E. Stuchbery, Phys. Rev. C **68**, 044312 (2003).

[65] F. Delaunay and F. M. Nunes, J. Phys. G: Nucl. Part. Phys. **34**, 2207 (2007).

[66] J. M. Cook, T. Glasmacher, and A. Gade, Phys. Rev. C **73**, 024315 (2006).

[67] A. Gade and B. M. Sherrill, Phys. Scr. **91**, 053003 (2016).

[68] D. J. Morrissey and B. M. Sherrill, Phil. Trans. R. Soc. Lond. **A356**, 1985 (1998).

[69] D. Bazin, J. Caggiano, B. Sherrill, J. Yurkon, and A. Zeller, Nucl. Instrum. Methods Phys. Res. B **204**, 629 (2003).

[70] G. Machicoane, D. Cole, J. Ottarson, J. Stetson, and P. Zavodszky, Review of Scientific Instruments **77**, 03A322 (2006).

[71] G. F. Knoll, *Radiation Detection and Measurement* (Wiley, 2000).

[72] O. B. Tarasov and D. Bazin, Nucl. Instrum. Methods Phys. Res. B **376**, 185 (2016).

[73] J. A. Caggiano, Ph.D. thesis, Michigan State University (1999).

[74] J. Yurkon, D. Bazin, W. Benenson, D. Morrissey, B. Sherrill, D. Swan, and R. Swanson, Nucl. Instrum. Methods Phys. Res. A **422**, 291 (1999).

[75] M. Berz, K. Joh, J. A. Nolen, B. M. Sherrill, and A. F. Zeller, Phys. Rev. C **47**, 537 (1993).

[76] K. Meierbachtol, D. Bazin, and D. J. Morrissey, Nucl. Instrum. Methods Phys. Res. A **652**, 668 (2011).

[77] K. Wimmer, D. Barofsky, D. Bazin, L. M. Fraile, J. Lloyd, J. R. Tompkins, and S. J. Williams, Nucl. Instrum. Methods Phys. Res. A **769**, 65 (2015).

[78] D. Weisshaar, D. Bazin, P. Bender, C. Campbell, F. Recchia, V. Bader, T. Baugher, J. Belarge, M. Carpenter, H. Crawford, M. Cromaz, B. Elman, P. Fallon, A. Forney, A. Gade, J. Harker, N. Kobayashi, C. Langer, T. Lauritsen, I. Lee, A. Lemasson, B. Longfellow, E. Lunderberg, A. Macchiavelli, K. Miki, S. Momiyama, S. Noji, D. Radford, M. Scott, J. Sethi, S. Stroberg, C. Sullivan, R. Titus, A. Wiens, S. Williams, K. Wimmer, and S. Zhu, Nucl. Instrum. Methods Phys. Res. A **847**, 187 (2017).

[79] S. Agostinelli, J. Allison, K. Amako, J. Apostolakis, H. Araujo, P. Arce, M. Asai, D. Axen, S. Banerjee, G. Barrand, F. Behner, L. Bellagamba, J. Boudreau, L. Broglia, A. Brunengo, H. Burkhardt, S. Chauvie, J. Chuma, R. Chytracek, G. Cooperman, G. Cosmo, P. Degtyarenko, A. Dell'Acqua, G. Depaola, D. Dietrich, R. Enami, A. Feliciello, C. Ferguson, H. Fesefeldt, G. Folger, F. Foppiano, A. Forti, S. Garelli, S. Giani, R. Giannitrapani, D. Gibin, J. G. Cadenas, I. González, G. G. Abril, G. Greeniaus, W. Greiner, V. Grichine, A. Grossheim, S. Guatelli, P. Gumplinger, R. Hamatsu, K. Hashimoto, H. Hasui, A. Heikkinen, A. Howard, V. Ivanchenko, A. Johnson, F. Jones, J. Kallenbach, N. Kanaya, M. Kawabata, Y. Kawabata, M. Kawaguti, S. Kelner, P. Kent, A. Kimura, T. Kodama, R. Kokoulin, M. Kossov, H. Kurashige, E. Lamanna, T. Lampén, V. Lara, V. Lefebure, F. Lei, M. Liendl, W. Lockman, F. Longo, S. Magni, M. Maire, E. Medernach, K. Minamimoto, P. M. de Freitas, Y. Morita, K. Murakami, M. Nagamatu, R. Nartallo, P. Nieminen, T. Nishimura, K. Ohtsubo, M. Okamura, S. O'Neale, Y. Oohata, K. Paech, J. Perl, A. Pfeiffer, M. Pia, F. Ranjard, A. Rybin, S. Sadilov, E. D. Salvo, G. Santin, T. Sasaki, N. Savvas, Y. Sawada, S. Scherer, S. Sei, V. Sirotenko, D. Smith, N. Starkov, H. Stoecker,

J. Sulkimo, M. Takahata, S. Tanaka, E. Tcherniaev, E. S. Tehrani, M. Tropeano, P. Truscott, H. Uno, L. Urban, P. Urban, M. Verderi, A. Walkden, W. Wander, H. Weber, J. Wellisch, T. Wenaus, D. Williams, D. Wright, T. Yamada, H. Yoshida, and D. Zschiesche, Nucl. Instrum. Methods Phys. Res. A **506**, 250 (2003).

[80] V. Bader, Ph.D. thesis, Michigan State University (2014).

[81] B. Elman, A. Gade, D. Weisshaar, D. Barofsky, D. Bazin, P. C. Bender, M. Bowry, M. Hjorth-Jensen, K. W. Kemper, S. Lipschutz, E. Lunderberg, N. Sachmpazidi, N. Terpstra, W. B. Walters, A. Westerberg, S. J. Williams, and K. Wimmer, Phys. Rev. C **96**, 044332 (2017).

[82] R. Brun and F. Rademakers, Nucl. Instrum. Methods Phys. Res. A **389**, 81 (1997).

[83] F. James and M. Roos, Computer Physics Communications **10**, 343 (1975).

[84] P. C. Bender, https://github.com/pcbend/grutinizer/.

[85] E. Lunderberg, Ph.D. thesis, Michigan State University (2014).

[86] J. W. Olness, E. K. Warburton, J. A. Becker, D. J. Decman, E. A. Henry, L. G. Mann, and L. Ussery, Phys. Rev. C **34**, 2049 (1986).

[87] E. K. Warburton, D. E. Alburger, and G. Wang, Phys. Rev. C **36**, 429 (1987).

[88] Z. M. Wang, R. Chapman, X. Liang, F. Haas, F. Azaiez, B. R. Behera, M. Burns, E. Caurier, L. Corradi, D. Curien, A. N. Deacon, Z. Dombrádi, E. Farnea, E. Fioretto, A. Gadea, A. Hodsdon, F. Ibrahim, A. Jungclaus, K. Keyes, V. Kumar, A. Latina, S. Lunardi, N. Mărginean, G. Montagnoli, D. R. Napoli, F. Nowacki, J. Ollier, D. O'Donnell, A. Papenberg, G. Pollarolo, M.-D. Salsac, F. Scarlassara, J. F. Smith, K. M. Spohr, M. Stanoiu, A. M. Stefanini, S. Szilner, M. Trotta, and D. Verney, Phys. Rev. C **81**, 054305 (2010).

[89] B. Longfellow, A. Gade, B. A. Brown, W. A. Richter, D. Bazin, P. C. Bender, M. Bowry, B. Elman, E. Lunderberg, D. Weisshaar, and S. J. Williams, Phys. Rev. C **97**, 054307 (2018).

[90] V. M. Bader, A. Gade, D. Weisshaar, B. A. Brown, T. Baugher, D. Bazin, J. S. Berryman, A. Ekström, M. Hjorth-Jensen, S. R. Stroberg, W. B. Walters, K. Wimmer, and R. Winkler, Phys. Rev. C **88**, 051301 (2013).

[91] D. Sohler, Z. Dombrádi, J. Timár, O. Sorlin, F. Azaiez, F. Amorini, M. Belleguic, C. Bourgeois, C. Donzaud, J. Duprat, D. Guillemaud-Mueller, F. Ibrahim, J. A. Scarpaci, M. Stanoiu, M. J. Lopez, M. G. Saint-Laurent, F. Becker, F. Sarazin, C. Stodel, G. Voltolini, S. M. Lukyanov, V. Maslov, Y.-E. Penionzhkevich, M. Girod, S. Péru, F. Nowacki, G. Sletten, R. Lucas, C. Theisen, D. Baiborodin, Z. Dlouhy, J. Mrazek, C. Borcea, A. Bauchet, C. J. Moore, and M. J. Taylor, Phys. Rev. C **66**, 054302 (2002).

[92] K. L. Miller, Ph.D. thesis, Michigan State University (2003).

[93] K. L. Yurkewicz, D. Bazin, B. A. Brown, C. M. Campbell, J. A. Church, D. C. Dinca, A. Gade, T. Glasmacher, M. Honma, T. Mizusaki, W. F. Mueller, H. Olliver, T. Otsuka, L. A. Riley, and J. R. Terry, Phys. Rev. C **70**, 054319 (2004).

[94] L. Cáceres, D. Sohler, S. Grévy, O. Sorlin, Z. Dombrádi, B. Bastin, N. L. Achouri, J. C. Angélique, F. Azaiez, D. Baiborodin, R. Borcea, C. Bourgeois, A. Buta, A. Bürger, R. Chapman, J. C. Dalouzy, Z. Dlouhy, A. Drouard, Z. Elekes, S. Franchoo, L. Gaudefroy, S. Iacob, B. Laurent, M. Lazar, X. Liang, E. Liénard, J. Mrazek, L. Nalpas, F. Negoita, F. Nowacki, N. A. Orr, Y. Penionzhkevich, Z. Podolyák, F. Pougheon, A. Poves, P. Roussel-Chomaz, M. G. Saint-Laurent, M. Stanoiu, and I. Stefan, Phys. Rev. C **85**, 024311 (2012).

[95] L. A. Riley, P. Adrich, N. Ahsan, T. R. Baugher, D. Bazin, B. A. Brown, J. M. Cook, P. D. Cottle, C. A. Diget, A. Gade, T. Glasmacher, K. E. Hosier, K. W. Kemper, A. Ratkiewicz, K. P. Siwek, J. A. Tostevin, A. Volya, and D. Weisshaar, Phys. Rev. C **86**, 047301 (2012).

[96] L. A. Riley, D. Bazin, J. Belarge, P. C. Bender, B. A. Brown, P. D. Cottle, B. Elman, A. Gade, S. D. Gregory, E. B. Haldeman, K. W. Kemper, B. R. Klybor, M. A. Liggett, S. Lipschutz, B. Longfellow, E. Lunderberg, T. Mijatovic, J. Pereira, L. M. Skiles, R. Titus, A. Volya, D. Weisshaar, J. C. Zamora, and R. G. T. Zegers, Phys. Rev. C **100**, 044312 (2019).

[97] N. Frank, T. Baumann, D. Bazin, R. R. C. Clement, M. W. Cooper, P. Heckman, W. A. Peters, A. Stolz, M. Thoennessen, and M. S. Wallace, Phys. Rev. C **68**, 054309 (2003).

[98] M. Matoš, A. Estrade, M. Amthor, A. Aprahamian, D. Bazin, A. Becerril, T. Elliot, D. Galaviz, A. Gade, S. Gupta, G. Lorusso, F. Montes, J. Pereira, M. Portillo, A. M. Rogers, H. Schatz, D. Shapira, E. Smith, A. Stolz, and M. Wallace, J. Phys. G **35**, 014045 (2007).

[99] R. W. Ibbotson, T. Glasmacher, P. F. Mantica, and H. Scheit, Phys. Rev. C **59**, 642 (1999).

[100] D. Mengoni, J. J. Valiente-Dobón, A. Gadea, S. Lunardi, S. M. Lenzi, R. Broda, A. Dewald, T. Pissulla, L. J. Angus, S. Aydin, D. Bazzacco, G. Benzoni, P. G. Bizzeti, A. M. Bizzeti-Sona, P. Boutachkov, L. Corradi, F. Crespi, G. de Angelis, E. Farnea, E. Fioretto, A. Goergen, M. Gorska, A. Gottardo, E. Grodner, A. M. Howard, W. Królas, S. Leoni, P. Mason, D. Montanari, G. Montagnoli, D. R. Napoli, A. Obertelli, R. Orlandi, T. Pawłat, G. Pollarolo, F. Recchia, A. Algora, B. Rubio, E. Sahin, F. Scarlassara, R. Silvestri, J. F. Smith, A. M. Stefanini, D. Steppenbeck, S. Szilner, C. A. Ur, P. T. Wady, and J. Wrzesiński, Phys. Rev. C **82**, 024308 (2010).

[101] S. Calinescu, L. Cáceres, S. Grévy, O. Sorlin, Z. Dombrádi, M. Stanoiu, R. Astabatyan, C. Borcea, R. Borcea, M. Bowry, W. Catford, E. Clément, S. Franchoo, R. Garcia,

R. Gillibert, I. H. Guerin, I. Kuti, S. Lukyanov, A. Lepailleur, V. Maslov, P. Morfouace, J. Mrazek, F. Negoita, M. Niikura, L. Perrot, Z. Podolyák, C. Petrone, Y. Penionzhkevich, T. Roger, F. Rotaru, D. Sohler, I. Stefan, J. C. Thomas, Z. Vajta, and E. Wilson, Phys. Rev. C **93**, 044333 (2016).

[102] R. Winkler, A. Gade, T. Baugher, D. Bazin, B. A. Brown, T. Glasmacher, G. F. Grinyer, R. Meharchand, S. McDaniel, A. Ratkiewicz, and D. Weisshaar, Phys. Rev. Lett. **108**, 182501 (2012).

[103] T. Czosnyka, D. Cline, and C. Y. Wu, Bull. Am. Phys. Soc. **28**, 745 (1983).